University of Warsaw
Faculty of Physics

Arumona Edward Arumona
Student no. 441784

Strongly coupled light in optical nanostructures based on excitonic materials

Doctoral's thesis
in PHYSICS

Supervisor:
dr hab. Tomasz Antosiewicz, prof. ucz.
Faculty of Physics

Warsaw, September 2025

Abstract

Strong light-matter coupling offers the possibility of altering material properties at the fundamental level. In recent years, the strong coupling phenomena have gained wide attention across many fields. Traditionally, strong coupling has been achieved using external optical cavities, which offer flexibility in selecting interacting components. However, this approach has limitations, such as requiring sophisticated fabrication techniques and complex experimental setups, which restrict scalability and practical applications. A compelling approach is self-hybridization, which allows optical modes and excitonic transitions to exist together in the same material, thereby avoiding the need for external cavity structures. Self-hybridization simplifies fabrication while maintaining the advantages of strong coupling, leading to efficient and compact device architectures.

This dissertation examines strong coupling between optical modes and excitons in self-hybridized uniaxial hyperbolic multilayer nanospheroids, systematically analyzing the effects of geometry and shape on these coupling phenomena. The nanospheroids have a wide range of aspect ratios that include prolate, sphere, and oblate geometries. Numerical and computational methods used for this study include the T-matrix and finite difference time domain (FDTD) techniques.

The first part of the research is the study of the optical modes of uniaxial hyperbolic nanospheriods that are composed of silver/silica multilayers. Their optical response and mode coupling characteristics are investigated in relation to their shape as the aspect ratio is varied from 1/3 (prolate) to 1 (sphere) to 3 (oblate). The optical responses are dependent on the material anisotropy, shape, and type of illumination. The results show that two dominant modes are present in the system: an electric dipole mode (ED) coupled to a magnetic quadrupole (MQ) and a magnetic dipole mode (MD) coupled to an electric quadrupole (EQ). The oblate shape exhibits less favorable optical mode characteristics compared to the prolate and spherical shapes.

Building upon these results, the second part of the research encompasses self-hybridized strong coupling of the optical modes to excitons in prolate and spherical geometries. Here, excitons are embedded within the material matrix as a function of their optical properties. The prolate and spherical nanoparticles exhibit large Rabi splitting as the oscillator strength is varied from 0 to 1 enabling strong coupling of the optical modes (ED and MD) to the excitons. The results show under which conditions the MD or ED modes offer greater coupling to excitonic or molecular transitions in the prolate and spherical geometries.

Building upon the MD dominance, the third part of the research focuses on evaluating practical realization of self-hybridized strong coupling of MD modes to excitons in the prolate and spherical geometries using TMDC (transition metal dichalcogenide) materials like MoS_2 (molybdenum disulfide), $MoSe_2$ (molybdenum diselenide), WS_2 (tungsten disulfide), and WSe_2 (tungsten diselenide). First, general considerations of coupling TMDCs to modes of hyperbolic nanoparticles are evaluated for simple two-component structures, which, however, yield an absence of strong coupling due to spectral detuning of the modes. To solve this limitation, a dielectric spacer is introduced to make the system a three-layered nanospheroid (silver/silica/TMDCs). The results show that the strong coupling in the MD regime is achieved in the three-layered prolate geometry composed of silver/silica/WS_2 and silver/silica/MoS_2.

In summary, this dissertation provides insight into how geometry and shape influence or suppress strong coupling in uniaxial hyperbolic multilayer nanospheroids. These can enhance the design of the next generation of opto-electronics devices.

Streszczenie

Silne sprzężenie światło-materia, które w ostatnich latach cieszy się szerokim zainteresowaniem badaczy na całym świecie, pozwala na modyfikację właściwości materiałów na poziomie fundamentalnym. Tradycyjnie silne sprzężenie uzyskuje się za pomocą zewnętrznych wnęk optycznych, które zapewniają elastyczność w doborze oddziałujących komponentów. Jednak to podejście ma ograniczenia, takie jak konieczność stosowania zaawansowanych technik wytwarzania i złożonych układów eksperymentalnych, co ogranicza skalowalność i praktyczne zastosowania. Alternatywnym podejściem jest auto-hybrydyzacja, która pozwala na współistnienie modów optycznych i przejść ekscytonowych w tym samym materiale, eliminując w ten sposób potrzebę stosowania zewnętrznych wnęk. Auto-hybrydyzacja upraszcza wytwarzanie, zachowując jednocześnie zalety silnego sprzężenia, co prowadzi do wydajnych i kompaktowych rowiązań.

Niniejsza rozprawa doktorska bada silne sprzężenie między modami optycznymi a ekscytonami w auto-hybrydyzowanych, jednoosiowych hiperbolicznych nanosferoidach zbudowanych z materiałów wielowarstwowych. W pracy tej zawarto systematyczną analizę wpływu geometrii, rozmiaru i składu materiałowego na zjawiska sprzężenia. Nanosferoidy charakteryzują się szerokim zakresem doboru kształtu od wydłużonych nanocząstek poprzez sferyczne do spłaszczonych. Metody numeryczne i obliczeniowe wykorzystane w tym badaniu obejmują techniki macierzy T i skończonej dziedziny czasu.

Pierwszą częścią oryginalnych badań jest analiza modów optycznych jednoosiowych hiperbolicznych nanosferiod zbudowanych z wielowarstw srebra i krzemionki. Ich odpowiedź optyczna i sprzężenie modów są badane w odniesieniu do ich kształtu i wewnętrznej struktury, przy czym współczynnik kształtu zmienia się od 1/3 (wydłużony) przez 1 (sferyczny) do 3 (spłaszczony). Odpowiedź optyczna zależy od anizotropii materiału, kształtu i rodzaju oświetlenia. Wyniki pokazują, że w układzie występują dwa dominujące mody: dipol elektryczny (ED) sprzężony z kwadrupolem magnetycznym (MQ) oraz dipol magnetyczny (MD) sprzężony z kwadrupolem elektrycznym (EQ). Nanocząstki o spłaszczonym kształcie wykazują mniej korzystne własności modów optycznych w porównaniu z tym o wydłużonych i sferycznych geometriach.

Bazując na powyższych wynikach, druga część badań obejmuje auto-hybrydyzujące silne sprzężenie modów optycznych z ekscytonami w nanocząstkach o wydłużonych i sferycznych geometriach. Zakłada się, że ekscytony są umieszczone w matrycy dielektrycznej, która wchodzi w skład warstwowego materiału hiperbolicznego. Nanocząstki wydłużone i sferyczne wykazują duże rozszczepienie Rabiego, umożliwiając silne sprzężenie modów optycznych (ED i MD) z ekscytonami. Wyniki pokazują, w jakich warunkach mody MD lub ED oferują silniejsze sprzężenie z przejściami ekscytonowymi lub molekularnymi w badanych nanocząstkach.

Bazując na wydajnym dipolu magnetycznym, trzecia część badań koncentruje się na ocenie praktycznej realizacji auto-hybrydyzacji w reżimie silnego sprzężenia modów MD z ekscytonami. W tej części badań wykorzystuje się dichalkogenki metali przejściowych jako składnik materiału hiperbolicznego: MoS_2 (disiarczek molibdenu), $MoSe_2$ (diselenek molibdenu), WS_2 (disiarczek wolframu) i WSe_2 (diselenek wolframu). Najpierw dokonano oceny ogólnych własności ekscytonów dichalkogenków metali przejściowych z modami nanocząstek hiperbolicznych dla prostych materiałów dwuskładnikowych (srebro plus dichalkogenek), które jednak charakteryzują się brakiem silnego sprzężenia z powodu rozstrojenia widmowego modów z ekscytonami. Aby rozwiązać to ograniczenie, wprowadzono dodatkową dielektryczną warstwę tworząc trójwarstwowy materiał hiperboliczny (srebro/krzemionka/dichalkogenek). Wyniki pokazują,

że w nanocząstkach zbudowanych z takich materiałów silne sprzężenie z ekscytonami może być osiągnięte zarówno dla modu dipola magnetycznego jak i elektrycznego, co pokazano na przykładzie nanocząstki zbudowanej ze srebra/krzemionki/WS_2 i srebra/krzemionki/MoS_2.

Podsumowując, niniejsza rozprawa przedstawia wgląd w to, jak geometria, rozmiar i struktura wewnętrzna wpływają lub tłumią silne sprzężenie w jednoosiowych hiperbolicznych wielowarstwowych nanosferoidach. Mogą one usprawnić projektowanie urządzeń optoelektronicznych nowej generacji.

Acknowledgements

I am very thankful to my supervisor, Dr. hab. Tomasz Antosiewicz, for the opportunity to conduct this research and for all the support I received when I came to Poland from Vietnam. I also thank him for his valuable suggestions that made this research possible and for his patience when I struggled to understand the research. I would also like to thank Dr. Krzysztof M. Czajkowski for teaching me how to use the SMUTHI package which implements the T-matrix method and his support during my first year of study. I thank my mother and brothers for their support and prayers, and I especially thank God for making all things possible.

Funding

The Dissertation topic is supported by the National Science Center, Poland via the project **Nanophotonic hybrid materials based on strong coupling of light to excitons** awarded to Dr. hab. Tomasz Antosiewicz, (grant number 2019/34/E/ST3/00359).

Contents

Chapter 1

Introduction to Strongly Coupled Light in Optical Nanostructures

1.1. Light-Matter Interaction

When light interacts with molecules or quantum emitters, it can be absorbed, scattered, reflected, or re-emitted as new light, transforming the light's energy in the process. These interactions enable us to explore, improve, or utilize the materials' properties [1]. The behavior of light-matter interactions is governed not merely by the fundamental properties of quantum emitters, but equally by the photonic environment around them, which modifies the local density of states in the optical field that the emitter experiences [2, 3]. Two distinct coupling regimes can be identified: weak and strong coupling. When it is weak coupling, energy exchange occurs more slowly than the rate at which the system loses energy to its surroundings. Under these conditions, the natural emission rate of quantum emitters is modified by the photonic structure around them (Figure 1.1(a) and (b)) [4]. By carefully designing the photonic environment, radiation can be either enhanced or suppressed depending on how the cavity interacts with the emitter at its characteristic frequency. This enhancement effect was first identified by Purcell [2, 5], who demonstrated that when an optical cavity resonates at the same frequency as a quantum emitter, it creates favorable conditions that accelerate the emitter's radiative decay.

In contrast, strong coupling emerges when energy exchange between the interacting elements happens much faster than energy loss from the system. This leads to the formation of two new hybrid states that exhibit coherent, reversible energy oscillations between light and matter components (Figure 1.1 (c) and (d)) [4]. These hybrid modes display unique characteristics, combining properties of both light (such as easy transport but low nonlinearity) and matter (high nonlinearity but limited transport). The energy separation between these hybrid states is known as vacuum Rabi splitting.

Strongly coupled optical cavity modes and electronic transitions have demonstrated effectiveness in tailoring and controlling various material properties. These modifications encompass areas such as electronic transport properties [6], polariton condensation [7], and chemical reactivity [8, 9]. Conventional strong coupling methods rely on external optical cavities that are physically separated from the material transitions. While this configuration provides flexibility in choosing which components interact, it comes with significant drawbacks, including the need for advanced fabrication tools and demanding experimental conditions that limit both scalability and real-world applications.

An alternative approach known as self-hybridization has emerged as a compelling solu-

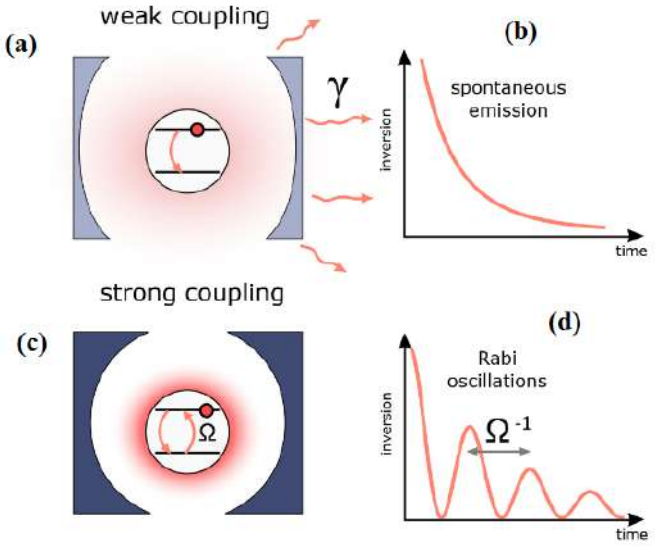

Figure 1.1: Comparison of weak and strong coupling regimes between quantum emitters and optical cavities: (a) Illustration of a dielectric optical cavity interacting with a quantum emitter in the weak coupling regime, where energy dissipates to the surrounding environment before completing the oscillation cycle between the two modes; (b) Quantum emitter population dynamics during spontaneous emission; (c) Schematic of an optical cavity interacting with a quantum emitter in the strong coupling regime, where electromagnetic oscillations between the quantum emitter and cavity take place prior to energy loss; (d) Quantum emitter population dynamics exhibiting Rabi oscillations (Figure adapted from [4]).

tion to these challenges. In self-hybridization, both optical modes and excitonic transitions exist within the same material system, removing the requirement for separate external cavities [10]. This configuration integrates material transitions and light confinement within a single platform, generating hybrid states with properties that differ markedly from their individual, non-interacting components. Self-hybridization streamlines the fabrication process while preserving the benefits of strong coupling, enabling the development of more efficient and compact device designs. This process relies on the material's inherent characteristics, including how it confines optical modes, its resonance behavior, and its geometric structure. Various materials have successfully exhibited self-hybridized polaritonic states, such as transition metal dichalcogenide (TMDC) multilayers [11], perovskite-based photonic crystals [12], organic-inorganic lead-halide perovskite cavities [13], layered perovskite structures [14], tungsten disulphide flakes [15], 2D halide perovskites [16], 2D Ruddlesden-Popper Perovskites [17], tungsten disulphide nanodisks [18], bulk TMDC nanoresonators [19], perovskite metasurfaces [20], or tungsten disulphide metasurfaces [21]. Building upon these advances in self-hybridization, new opportunities arise for exploring novel nanostructures that can further enhance and control light-matter interactions.

1.2. Research Motivation

This dissertation advances the field further by exploring self-hybridized strong coupling in a new type of nanostructure. This structure uniquely combines the properties of hyperbolic metamaterials with precise geometric control. The proposed novel nanostructure for this

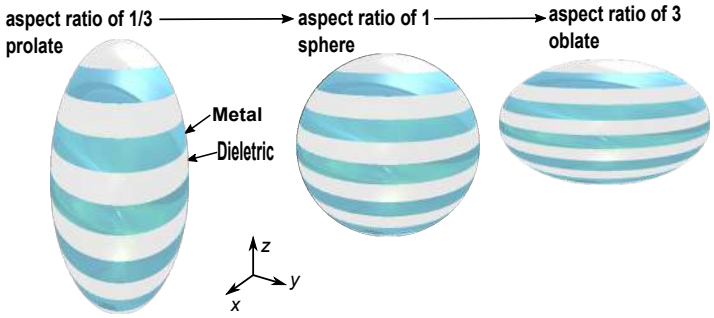

Figure 1.2: Multilayer nanospheroid structures with varying aspect ratios (prolate, sphere, oblate)

work are uniaxial hyperbolic multilayer nanospheroids. This nanostructure takes the form of a spheroid with aspect ratios that include prolate, spherical, and oblate shapes, as shown in Figure 1.2. It is composed of alternating metal and dielectric layers, with the capability to incorporate excitonic materials, especially within the latter material.

These nanospheroids simultaneously support optical modes, such as electric dipole (ED) and magnetic dipole (MD) resonances, and excitons within the same nanostructure. The advantage of this nanostructure over others, such as purely plasmonic or dielectric ones, is that it combines the benefits of a metallic optical response, which is dominated by strong electric dipole resonance [22], and of a dielectric optical response, which has a strong magnetic dipole resonance [23], all determined fundamentally by the material platform. Furthermore, these optical resonances are tunable and can be tailored across different spatial directions. This dissertation examines strong coupling between optical modes and excitons in self-hybridized uniaxial hyperbolic multilayer nanospheroids, systematically analyzing the effects of geometry and shape on these coupling phenomena.

1.3. Dissertation Outline

The dissertation is structured as follows: **CHAPTER 1** to **CHAPTER 3** form the literature review, discussing the phenomenon of strong coupling and relevant fundamental concepts of this dissertation.

CHAPTER 4 provides a description of the methodologies used in this research. Numerical studies are conducted using classical electrodynamics methods and coupled harmonic oscillator models to analyze shape-dependent effects on self-hybridized strong coupling.

CHAPTER 5 focuses on the study of optical modes in uniaxial hyperbolic multilayer nanospheroids. This chapter examines the optical response of these nanospheroids in the presence of an electromagnetic field, serving as a foundation for subsequent analyses.

CHAPTER 6 investigates self-hybridized strong coupling between optical modes and excitons in uniaxial hyperbolic multilayer nanospheroids. Leveraging the optical mode analysis from Chapter 5, this chapter examines how optical modes interact with excitonic transitions within these nanostructures. **CHAPTER 7** builds on these findings by focusing specifically on self-hybridized strong coupling phenomena in three-layered uniaxial hyperbolic nanospheroids. While Chapters 5 and 6 focused on nanospheroids made of two-material multilayers (silver-silica), this chapter investigates nanospheroids incorporating three materials: silver, silica, and TMDCs. The TMDCs considered include WS_2, WSe_2, MoS_2, and $MoSe_2$.

CHAPTER 8 concludes the dissertation by summarizing the key findings and offering perspectives on potential future research directions.

1.4. List of Scientific Papers

Published Paper (Part of the Dissertation):

1. Arumona, A. E., Czajkowski, K. M., Antosiewicz, T. J. (2023). Material- and shape-dependent optical modes of hyperbolic spheroidal nanoresonators. *Optics Express 31*(14), 23459. https://doi.org/10.1364/oe.494389

2. Arumona, A. E., Antosiewicz, T. J. (2025). Self-hybridized strong coupling of optical modes to excitons in hyperbolic nanoresonators. *Optics Express 33*(16), 34537. https://doi.org/10.1364/OE.569875

3. Arumona, A. E., Antosiewicz, T. J. (2025). Self-Hybridized Strong Coupling of MD Mode to Exciton in Uniaxial Hyperbolic Multilayer Nanospheroids. *In manuscript.*

Other Published Paper (Not Part of the Dissertation):

4. Arumona, A. E., Johnson, A. (2024). Prediction of optical properties of uniaxial hyperbolic nanospheres via artificial neural networks. *Physica Scripta, 99*(11). https://doi.org/10.1088/1402-4896/ad7fa2

Chapter 2

Fundamentals

Having established the context and motivation for investigating strongly coupled light in optical nanostructures in Chapter 1, it is essential to recall the fundamental physical principles that govern these interactions. Chapter 2 provides the theoretical foundation necessary to analyse and design the hyperbolic nanospheroids that form the core of this dissertation.

2.1. Classical Electrodynamics

The behavior of electromagnetic fields within classical physics is governed by Maxwell's fundamental equations, which form the cornerstone of electromagnetic theory and provide the foundation for understanding light-matter interactions in nanophotonic systems. These equations relate the electric and magnetic fields to their sources and describe how they propagate through space and matter.

In their most general form, Maxwell's equations are [24]:

$$\nabla \cdot \vec{D} = \rho, \tag{2.1}$$

$$\nabla \cdot \vec{B} = 0, \tag{2.2}$$

$$\nabla \times \vec{E} = -\frac{\partial \vec{B}}{\partial t}, \tag{2.3}$$

$$\nabla \times \vec{H} = \frac{\partial \vec{D}}{\partial t} + \vec{j}, \tag{2.4}$$

where $\vec{E}$ is the electric field vector, $\vec{H}$ is the magnetic field, $\vec{D}$ is the electric displacement field, $\vec{B}$ is the magnetic induction, ρ is the charge density, and $\vec{j}$ is the current density. These fields are related to the material properties through constitutive relations that describe how matter responds to electromagnetic excitation.

In macroscopic electromagnetic theory, the response of materials to electromagnetic fields is characterized through the polarization vector $\vec{P}$, magnetization $\vec{M}$, and conductivity κ. The constitutive relations connect the fundamental fields to the material-dependent displacement and magnetic fields:

$$\vec{D}(\vec{r}, t) = \varepsilon_0 \vec{E}(\vec{r}, t) + \vec{P}(\vec{r}, t), \tag{2.5}$$

$$\vec{H}(\vec{r}, t) = \mu_0^{-1} \vec{B}(\vec{r}, t) - \vec{M}(\vec{r}, t), \tag{2.6}$$

where ε_0 and μ_0 are the vacuum permittivity and permeability, respectively. The current

density includes contributions from both conduction and material polarization:

$$\vec{j} = \vec{j}_c + \vec{j}_s + \frac{\partial \vec{P}}{\partial t} + \nabla \times \vec{M}, \tag{2.7}$$

where $\vec{j}_c = \kappa(\vec{r}, t)\vec{E}(\vec{r}, t)$ is the conduction current and $\vec{j}_s$ represents external source currents.

For linear, isotropic materials, the polarization and magnetization respond linearly to the applied fields:

$$\vec{P} = \varepsilon_0 \chi_e \vec{E}, \tag{2.8}$$

$$\vec{M} = \chi_m \vec{H}, \tag{2.9}$$

where χ_e and χ_m are the electric and magnetic susceptibilities. This leads to the familiar material parameters:

$$\varepsilon = \varepsilon_0(1 + \chi_e), \qquad \mu = \mu_0(1 + \chi_m), \tag{2.10}$$

which define the permittivity and permeability of the medium.

For time-harmonic fields oscillating at angular frequency $\omega = 2\pi\nu$, we can express the fields with temporal dependence $\vec{E}(\vec{r}, t) = \mathrm{Re}(\vec{E}(\vec{r})e^{-i\omega t})$. This frequency domain representation simplifies the analysis of electromagnetic phenomena and is particularly useful for studying resonant systems. Maxwell's equations in the frequency domain become:

$$\nabla \times \vec{E} = i\omega \vec{B}, \tag{2.11}$$

$$\nabla \cdot \vec{D} = \rho, \tag{2.12}$$

$$\nabla \times \vec{H} = -i\omega \vec{D} + \vec{j}, \tag{2.13}$$

$$\nabla \cdot \vec{B} = 0. \tag{2.14}$$

The frequency domain formulation is essential for analyzing the optical properties of materials and the resonant behavior of nanostructures.

To understand how electromagnetic fields propagate through materials, we derive the wave equations from Maxwell's equations. In a source-free, homogeneous, linear, isotropic medium, Maxwell's curl equations reduce to:

$$\nabla \times \vec{E} = -\mu \frac{\partial \vec{H}}{\partial t}, \tag{2.15}$$

$$\nabla \times \vec{H} = \varepsilon \frac{\partial \vec{E}}{\partial t}. \tag{2.16}$$

Taking the curl of the first equation and substituting the second gives:

$$\nabla \times (\nabla \times \vec{E}) = -\mu\varepsilon \frac{\partial^2 \vec{E}}{\partial t^2}. \tag{2.17}$$

Using the vector identity $\nabla \times (\nabla \times \vec{E}) = \nabla(\nabla \cdot \vec{E}) - \nabla^2 \vec{E}$ and noting that $\nabla \cdot \vec{E} = 0$ in a source-free medium, we obtain the wave equation for the electric field:

$$\nabla^2 \vec{E} - \mu\varepsilon \frac{\partial^2 \vec{E}}{\partial t^2} = 0. \tag{2.18}$$

Similarly, the magnetic field satisfies:

$$\nabla^2 \vec{H} - \mu\varepsilon \frac{\partial^2 \vec{H}}{\partial t^2} = 0. \tag{2.19}$$

The fundamental solutions to these wave equations are plane waves, which form the basis for understanding electromagnetic propagation. The general plane wave solution can be written as:

$$\vec{E} = \vec{E}_0 \cdot f(\omega t - \vec{k} \cdot \vec{r}) \tag{2.20}$$

where $\vec{E}_0$ denotes a constant amplitude vector perpendicular to the wave vector $\vec{k}$, while $f(x)$ represents an arbitrary waveform function. This expression describes electromagnetic radiation with polarization perpendicular to its propagation direction, as specified by $\vec{k}$. The field maintains constant amplitude across planes normal to $\vec{k}$, with its profile along the propagation axis determined by the function $f(x)$.

Substituting this general solution into the wave equation yields the fundamental dispersion relation for plane waves in a homogeneous medium:

$$k^2 = k_x^2 + k_y^2 + k_z^2 = \omega^2 \mu \varepsilon. \tag{2.21}$$

The wave number and frequency are related through the dispersion relation:

$$k = \frac{\omega}{v} = \frac{2\pi}{\lambda}, \quad \text{where} \quad \lambda = \frac{v}{\nu}, \quad v = \frac{c}{n}, \quad n = \sqrt{\varepsilon_r \mu_r}, \tag{2.22}$$

with $\varepsilon_r = \varepsilon/\varepsilon_0$ and $\mu_r = \mu/\mu_0$ being the relative permittivity and permeability. The phase velocity, which describes the propagation speed of constant phase surfaces, is given by:

$$v_p = \frac{\omega}{k} = \frac{c}{n}, \tag{2.23}$$

where n is the refractive index and c represents the speed of light in vacuum.

At interfaces between different materials, the electromagnetic fields must satisfy specific boundary conditions that ensure continuity of the tangential electric field and normal magnetic field components. These boundary conditions are essential for understanding reflection, transmission, and field confinement at material interfaces in nanostructures. At the interface between media i and j, with $\vec{n}$ as the unit normal vector, the conditions are:

$$\vec{n} \times (\vec{E}_j - \vec{E}_i) = 0, \tag{2.24}$$

$$\vec{n} \times (\vec{H}_j - \vec{H}_i) = \vec{j}_{\text{surf}}, \tag{2.25}$$

$$\vec{n} \cdot (\vec{D}_j - \vec{D}_i) = \sigma, \tag{2.26}$$

$$\vec{n} \cdot (\vec{B}_j - \vec{B}_i) = 0, \tag{2.27}$$

where $\vec{j}_{\text{surf}}$ is the surface current density and σ is the surface charge density. These boundary conditions are fundamental to understanding the behavior of electromagnetic fields in layered structures and at the interfaces of nanoparticles, which are central to the operation of hyperbolic nanospheroids.

2.2. Plane Waves at Multilayer Interfaces

The analysis of plane wave propagation through multilayer structures extends the fundamental Fresnel equations [25] to complex dielectric systems with multiple interfaces and arbitrary layer thicknesses. This formalism provides the theoretical foundation for analyzing optical behavior in layered structures where each interface contributes to the overall reflection and transmission characteristics.

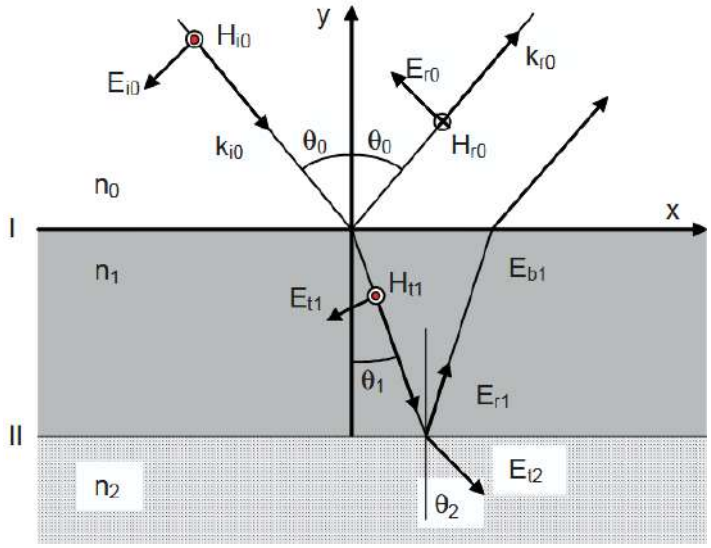

Figure 2.1: Schematic of the incident, reflected, transmitted, and back-reflected components of a Transversal-Electric field (TE) plane wave incident on a dielectric film (Figure adapted from [25]).

For a multilayer system, we consider the boundary conditions at each interface between adjacent media. Figure 2.1 illustrates the wave components in a multilayer dielectric structure, showing the incident wave E_{i0} with wave vector k_{i0}, reflected wave E_{r0} with wave vector k_{r0}, forward transmitted wave E_{t1} with wave vector k_{t1}, and backward reflected wave E_{b1} with wave vector k_{b1} at the interfaces. The angles θ_0, θ_1, and θ_2 represent the propagation angles in media with refractive indices n_0, n_1, and n_2 respectively. The magnetic field components H_{i0}, H_{r0}, H_{t1}, and H_{b1} correspond to their respective electric field components.

Tangential electric and magnetic field components must remain continuous at interface I between media 0 and 1. At interface I, these conditions are expressed as:

$$E_I = E_{i0}\cos\theta_0 + E_{r0}\cos\theta_0 = E_{t1}\cos\theta_1 + E_{b1}\cos\theta_1, \tag{2.28}$$

$$H_I = H_{i0} - H_{r0} = H_{t1} - H_{b1}, \tag{2.29}$$

where E_{i0} and E_{r0} are the incident and reflected field amplitudes in medium 0, while E_{t1} and E_{b1} are the forward and backward propagating field amplitudes in medium 1. The negative sign in the magnetic field boundary condition accounts for the phase reversal of the reflected wave traveling away from the interface.

For non-magnetic materials, the relationship between magnetic and electric fields is given by $\vec{H} = \sqrt{\varepsilon_0/\mu_0} \cdot n \cdot (\vec{k}/|\vec{k}|) \times \vec{E}$, which allows us to express the magnetic field boundary conditions in terms of the electric field amplitudes. An important consideration in multilayer analysis is the phase shift accumulated by a beam crossing a dielectric film of thickness d at angle θ. This phase shift is given by:

$$\phi = k_0 nd\cos\theta = \frac{2\pi}{\lambda_0} nd\cos\theta. \tag{2.30}$$

This expression accounts for the actual optical path and lateral shift of the beam, which is counterintuitive compared to the simple geometric path length but crucial for accurate multilayer calculations.

The mathematical treatment of multilayer systems employs the transfer matrix method, which relates the electromagnetic fields on opposite sides of each layer through matrix multiplication. For a single layer with thickness d_1 and refractive index n_1, the transfer matrix M_1 connects the fields at the input and output interfaces:

$$\begin{bmatrix} E_I \\ H_I \end{bmatrix} = M_1 \begin{bmatrix} E_{II} \\ H_{II} \end{bmatrix}. \tag{2.31}$$

The transfer matrix for a single layer is expressed as:

$$M_1 = \begin{bmatrix} \cos(k_0 n_1 d_1 \cos\theta_1) & j\sin(k_0 n_1 d_1 \cos\theta_1)/\Gamma_1 \\ j\Gamma_1 \sin(k_0 n_1 d_1 \cos\theta_1) & \cos(k_0 n_1 d_1 \cos\theta_1) \end{bmatrix}, \tag{2.32}$$

where the parameter Γ_1 depends on the polarization state of the incident wave. For TM (p-polarized) waves, $\Gamma_{1,\mathrm{TM}} = \sqrt{\varepsilon_0/\mu_0} n_1 \cos\theta_1$, while for TE (s-polarized) waves, $\Gamma_{1,\mathrm{TE}} = \sqrt{\varepsilon_0/\mu_0} n_1/\cos\theta_1$. The difference in these expressions reflects the distinct boundary conditions for electric and magnetic field components parallel to the interface for different polarizations.

For a complete multilayer stack consisting of p layers, the total transfer matrix is obtained by multiplying the individual layer matrices in sequence. The fields at the front surface of the stack are related to the fields at the bottom of the final layer through:

$$\begin{bmatrix} E_I \\ H_I \end{bmatrix} = M_1 M_2 M_3 \cdots M_p \begin{bmatrix} E_{p+1} \\ H_{p+1} \end{bmatrix} = M \begin{bmatrix} E_{p+1} \\ H_{p+1} \end{bmatrix}, \tag{2.33}$$

where the total transfer matrix

$$M = \begin{bmatrix} m_{11} & m_{12} \\ m_{21} & m_{22} \end{bmatrix}, \tag{2.34}$$

encodes the cumulative optical properties of the entire multilayer system.

Using the boundary conditions at the first and last interfaces of the multilayer stack, we can derive expressions for the reflection and transmission coefficients. For TM polarization, these coefficients are:

$$r_{\mathrm{TM}} = \frac{E_{r0}}{E_{i0}} = \frac{\Gamma_{0,\mathrm{TM}} m_{11} + \Gamma_{0,\mathrm{TM}}\Gamma_{p+1,\mathrm{TM}} m_{12} - m_{21} - \Gamma_{p+1,\mathrm{TM}} m_{22}}{\Gamma_{0,\mathrm{TM}} m_{11} + \Gamma_{0,\mathrm{TM}}\Gamma_{p+1,\mathrm{TM}} m_{12} + m_{21} + \Gamma_{p+1,\mathrm{TM}} m_{22}}, \tag{2.35}$$

$$t_{\mathrm{TM}} = \frac{E_{tp}}{E_{i0}} = \frac{2\Gamma_{0,\mathrm{TM}}}{\Gamma_{0,\mathrm{TM}} m_{11} + \Gamma_{0,\mathrm{TM}}\Gamma_{p+1,\mathrm{TM}} m_{12} + m_{21} + \Gamma_{p+1,\mathrm{TM}} m_{22}}. \tag{2.36}$$

Similar expressions apply for TE polarization, where the reflection and transmission coefficients are given by:

$$r_{\mathrm{TE}} = \frac{E_{r0}}{E_{i0}} = \frac{\Gamma_{0,\mathrm{TE}} m_{11} + \Gamma_{0,\mathrm{TE}}\Gamma_{p+1,\mathrm{TE}} m_{12} - m_{21} - \Gamma_{p+1,\mathrm{TE}} m_{22}}{\Gamma_{0,\mathrm{TE}} m_{11} + \Gamma_{0,\mathrm{TE}}\Gamma_{p+1,\mathrm{TE}} m_{12} + m_{21} + \Gamma_{p+1,\mathrm{TE}} m_{22}}, \tag{2.37}$$

$$t_{\mathrm{TE}} = \frac{E_{tp}}{E_{i0}} = \frac{2\Gamma_{0,\mathrm{TE}}}{\Gamma_{0,\mathrm{TE}} m_{11} + \Gamma_{0,\mathrm{TE}}\Gamma_{p+1,\mathrm{TE}} m_{12} + m_{21} + \Gamma_{p+1,\mathrm{TE}} m_{22}}. \tag{2.38}$$

These formulas provide a systematic approach to calculating reflection and transmission through any layered optical structure with parallel interfaces for both polarization states, making them invaluable for the design and analysis of complex optical systems.

The matrix formulation scales efficiently with the number of layers and maintains numerical stability for most practical applications. However, care must be taken with sign conventions and phase relationships to ensure physical consistency of the results. The method is particularly powerful because it can handle both real and complex dielectric constants, enabling analysis of lossy materials and metal-dielectric structures where absorption and complex optical properties play important roles.

2.3. Lorentz-Drude Permittivity Model

The Lorentz-Drude permittivity model describes the optical properties of materials by combining the contributions of dielectrics (bound electrons) and metals (free electrons). In dielectric materials, the optical response is dominated by the displacement of bound electrons under an applied electric field, while in metals, the conduction electrons exhibit a free-electron behavior due to the absence of a restoring force from atomic cores [26, 27].

For an electron in an oscillating electric field $\mathbf{E} = \mathbf{E}_0 e^{-i\omega t}$, the equation of motion is:

$$m\frac{d^2x}{dt^2} + m\gamma\frac{dx}{dt} + m\omega_0^2 x = -eE_0 e^{-i\omega t}, \tag{2.39}$$

where m is the effective mass of the electron, γ is the damping coefficient representing energy loss, ω_0 is the natural frequency of oscillation, and $-e$ is the electron charge.

Assuming a solution of the form $x = x_0 e^{-i\omega t}$, we substitute into the equation of motion:

$$-m\omega^2 x_0 - im\gamma\omega x_0 + m\omega_0^2 x_0 = -eE_0 \tag{2.40}$$

to solve for x_0:

$$x_0 = \frac{eE_0}{m(\omega_0^2 - \omega^2 - i\gamma\omega)}. \tag{2.41}$$

Then, the polarization $\mathbf{P}$ is related to the dipole moment:

$$P = -Nex_0 = -\frac{Ne^2E_0}{m(\omega_0^2 - \omega^2 - i\gamma\omega)}, \tag{2.42}$$

where N is the number density of oscillators. The electric susceptibility χ is defined by $\mathbf{P} = \varepsilon_0\chi\mathbf{E}$, so:

$$\chi = -\frac{Ne^2}{\varepsilon_0 m(\omega_0^2 - \omega^2 - i\gamma\omega)}, \tag{2.43}$$

finally giving the dielectric function as $\varepsilon = \varepsilon_0(1 + \chi)$:

$$\varepsilon(\omega) = \varepsilon_0\left[1 - \frac{Ne^2}{\varepsilon_0 m(\omega_0^2 - \omega^2 - i\gamma\omega)}\right]. \tag{2.44}$$

One can introduce the plasma frequency as:

$$\omega_p^2 = \frac{Ne^2}{\varepsilon_0 m}, \tag{2.45}$$

allowing us to write:

$$\varepsilon(\omega) = \varepsilon_0\left[1 - \frac{\omega_p^2}{\omega_0^2 - \omega^2 - i\gamma\omega}\right]. \tag{2.46}$$

In real materials, there are additional contributions to the permittivity from core electrons and other sources. This is accounted for by a background permittivity ε_∞ ($\varepsilon_0 \to \varepsilon_\infty$):

$$\varepsilon(\omega) = \varepsilon_\infty\left[1 - \frac{\omega_p^2}{\omega_0^2 - \omega^2 - i\gamma\omega}\right]. \tag{2.47}$$

In the absence of a restoring force, such as for a material with free conduction electrons, we set $\omega_0 = 0$ and obtain the Drude model:

$$\varepsilon(\omega) = \varepsilon_\infty\left[1 - \frac{\omega_p^2}{\omega^2 + i\gamma\omega}\right]. \tag{2.48}$$

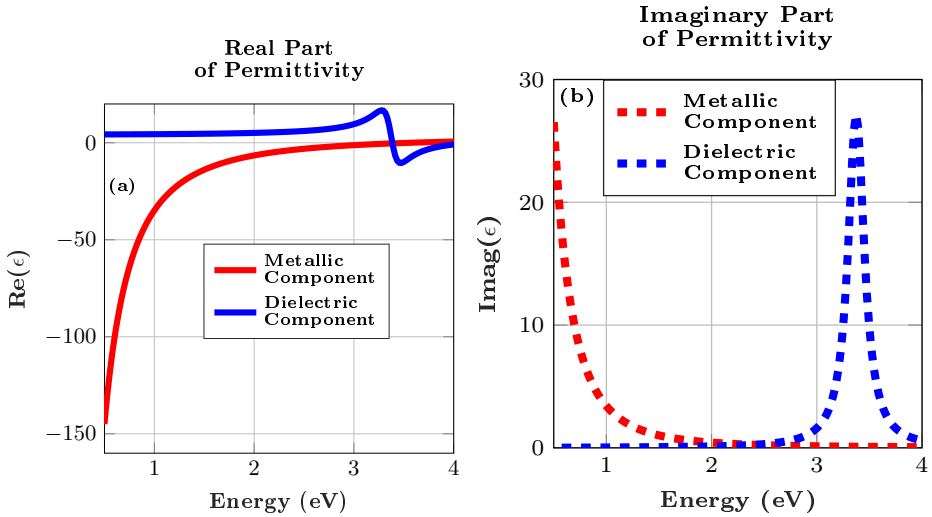

Figure 2.2: Energy-dependent permittivity of a metal-dielectric composite system described by the Lorentz-Drude model. (a) Real part of the permittivity showing the metallic component (red solid line) with characteristic negative values at low energies and the dielectric component (blue solid line) exhibiting positive values with resonant features. (b) Imaginary part of the permittivity displaying the metallic component (red dashed line) with high losses at low energies and the dielectric component (blue dashed line) with resonant absorption peaks. The complementary behavior of these components forms the basis for hyperbolic metamaterial properties.

In contrast, when $\omega_0 \neq 0$, we have bound electrons with a specific resonance frequency and the permittivity assumes the characteristic shape of a Lorentzian function.

To demonstrate the applicability of the Lorentz-Drude model to composite materials, we consider a metal-dielectric system that combines both free and bound electron responses. Figure 2.2 illustrates the energy-dependent permittivity of such a composite material, showing both the real part (panel a) and imaginary part (panel b) of the dielectric function. The metallic component (red curves) exhibits the characteristic negative real permittivity at low energies and significant losses, while the dielectric component (blue curves) shows resonant behavior with minimal losses. This complementary behavior forms the foundation for understanding the optical response of hyperbolic nanospheroids, where the combination of metallic and dielectric elements enables unique electromagnetic properties.

2.4. Introduction to Hyperbolic Metamaterials

Hyperbolic metamaterials (HMMs) are a class of materials that are typically artificially engineered or structured, however, examples of naturally occurring can be found.Their initial development began in the microwave frequency range and gradually it has evolved into the optical frequency range with them exhibiting hyperbolic behavior. The key feature of HMMs is their ability to support a high density of electromagnetic states across a broad bandwidth. This arises from their hyperbolic dispersion relation, a result of anisotropic permittivity with opposing signs. By providing an increased photonic density of states, HMMs enhance light-matter interactions, making them better than traditional optical devices for applications like single-molecule sensing, super-resolution imaging, and controlling quantum emitter dynamics.

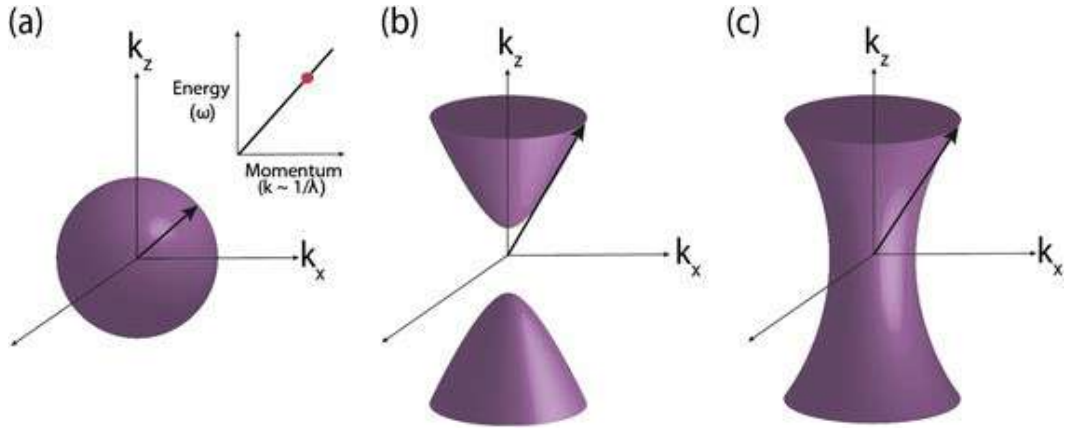

Figure 2.3: Isofrequency surfaces for different electromagnetic media. (a) A spherical isofrequency surface characteristic of an isotropic dielectric. The inset illustrates the energy-momentum dispersion relationship, where the red dot marks the operating frequency corresponding to the depicted isofrequency surface. (b) Type I HMM behavior (two-sheeted hyperboloid). (c) Type II HMM behavior (single-sheeted hyperboloid) (Figures (a-c) adapted from [28]).

HMMs get their name from the unique way waves travel through them. In a vacuum, waves spread equally in all directions, creating a spherical isofrequency contour (as shown in Figure 2.3(a)). However, in HMMs, the isofrequency surface forms an open hyperboloid shape as shown in Figure 2.3(b,c), depending on the signs of the diagonal elements of the permittivity tensor. This unusual behavior happens because these materials act like a metal along one axis while behaving like an insulator (dielectric) along another axis.

2.4.1. Hyperbolic Dispersion

For electromagnetic waves in uniaxial media, the dispersion relation can be derived from Maxwell's equations given in Section 2.1. The isofrequency contour (IFC), whose examples are plotted in Fig. 2.3, represents the relationship between the wavevector components k_x, k_y, and k_z at a fixed frequency ω. It describes all possible wavevector combinations that can propagate at that specific frequency, essentially mapping the allowed momentum states for electromagnetic waves in the material. The shape of the IFC determines fundamental wave propagation characteristics including the direction of energy flow, allowed propagation modes, and the density of optical states.

For electric uniaxial media with $\mu_{\parallel} = \mu_{\perp} = 1$, the wave equation leads to a dispersion relation that describes two distinct types of modes. The complete dispersion relation is given by [29]:

$$\left(k_x^2 + k_y^2 + k_z^2 - \varepsilon_{\parallel} k_0^2\right)\left(\frac{k_x^2 + k_y^2}{\varepsilon_{\perp}} + \frac{k_z^2}{\varepsilon_{\parallel}} - k_0^2\right) = 0, \tag{2.49}$$

where k_0 is the wave-vector in free space. The first bracketed term describes TE-polarized (transverse electric) waves with electric fields perpendicular to the optical axis in the xy plane. This TE mode corresponds to an ordinary wave with isofrequency contour taking the form of a sphere: $k_x^2 + k_y^2 + k_z^2 = \varepsilon_{\parallel} k_0^2$. The spherical IFC indicates that waves can propagate equally well in all directions, similar to isotropic materials.

The second term describes TM-polarized (transverse magnetic) waves with magnetic fields

in the xy plane. This TM mode corresponds to an extraordinary wave with isofrequency contour given by:

$$\frac{k_x^2 + k_y^2}{\varepsilon_\perp} + \frac{k_z^2}{\varepsilon_\parallel} = k_0^2. \tag{2.50}$$

When $\varepsilon_\parallel > 0$ and $\varepsilon_\perp < 0$, both TE and TM modes can coexist. In this case, the IFC of the TE mode takes the form of a sphere, while the IFC of the TM mode corresponds to a two-fold hyperboloid, creating what is called a dielectric-type or Type I HMM. The hyperbolic IFC is fundamentally different from the closed spherical or elliptical contours found in conventional materials because it forms an open surface that extends to infinity in k-space.

TM modes are fundamentally more important in hyperbolic metamaterials because they are the modes that exhibit hyperbolic dispersion when $\varepsilon_\parallel \varepsilon_\perp < 0$. The hyperbolic dispersion of TM modes enables the unique properties that make HMMs valuable for applications. The open hyperboloid isofrequency contour allows propagation of waves with arbitrarily large wave-vectors, which are normally evanescent in conventional materials. This leads to an enhanced optical density of states, enabling phenomena such as enhanced spontaneous emission, super-resolution imaging, and unusual refraction properties. In contrast, TE modes maintain elliptical dispersion characteristics with closed IFCs similar to ordinary materials, limiting their contribution to the novel properties of HMMs.

HMMs can be classified into two types based on their dielectric tensor components and the resulting IFC shapes. Type I HMMs, also called dielectric-type, have one negative component ($\varepsilon_\perp < 0$, $\varepsilon_\parallel > 0$) and feature a two-fold hyperboloid isofrequency surface as shown in Figure 2.3(b). Type II HMMs, also called metal-type, have the opposite sign configuration ($\varepsilon_\perp > 0$, $\varepsilon_\parallel < 0$) and exhibit a single-fold hyperboloid isofrequency surface as shown in Figure 2.3(c). Both types can sustain waves with infinitely large wavevectors within the effective medium approximation, whereas such waves would ordinarily be evanescent and decay exponentially in conventional materials.

The key characteristic that sets hyperbolic media apart is how they handle waves with large wavevectors. In conventional materials, high-magnitude wavevector components quickly fade away as evanescent waves because they fall outside the closed IFC. However, in hyperbolic media, the open isofrequency contours allow waves to theoretically propagate through the material regardless of their wavevector magnitude. This unique ability to support high-k propagating modes enables the conversion of evanescent waves into propagating waves, opening up possibilities for sub-diffraction applications and novel optical devices.

HMMs have found broad applications spanning negative refraction, sub-diffraction imaging, enhanced sensing, and engineering of spontaneous and thermal emissions [28, 30–38]. Their ability to manipulate the flow of electromagnetic energy at subwavelength scales has made them valuable for next-generation optical technologies including hyperlenses, high-sensitivity biosensors, and quantum optical devices.

2.4.2. Material Platforms for Hyperbolic Dispersion

To achieve hyperbolic dispersion, one needs material platforms that have the required anisotropic electromagnetic properties to enable unique light-matter interactions. Such material platforms are natural and artificially engineered materials as shown in Figure 2.4. Natural HMMs have hyperbolic dispersion due to their intrinsic properties. Such materials are graphite, magnesium diboride (MgB_2), magnesium difloride (MgF_2), hexagonal boron nitride (h-BN), and α-phase molybdenum trioxide (α-MoO_3). Graphite possesses HMM behavior in the ultraviolet (UV) and MgB_2 in the visible. h-BN has dual mode of operation, acting as a Type I hyperbolic material between 11.76 and 13.15 μm and Type II material between 6.17 and

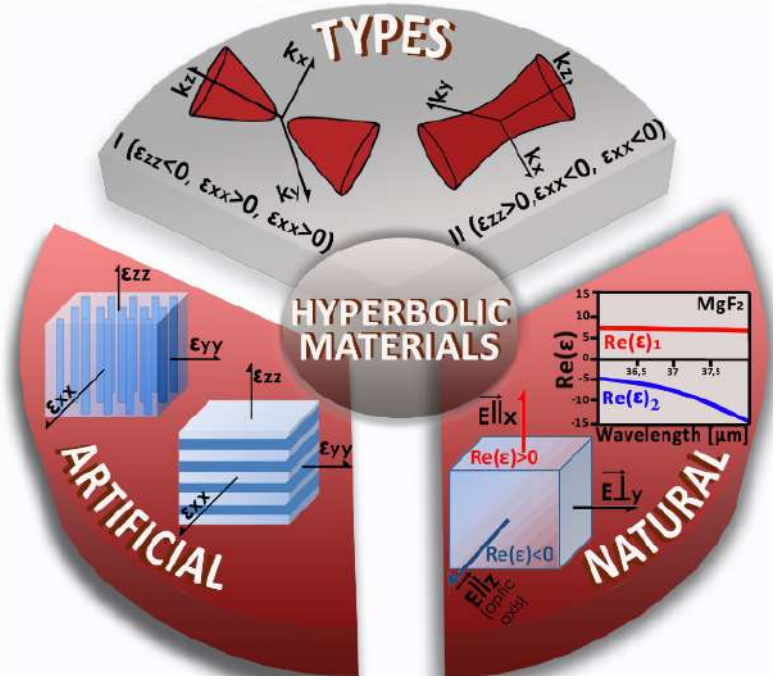

Figure 2.4: Overview of hyperbolic metamaterial types and material platforms, showing artificial multilayer structures, natural materials, and their characteristic dispersion properties (Figure adapted from [39]).

7.35 μm. α-MoO_3 supports hyperbolic dispersion in specific mid-infrared wavelengths. While these natural materials offer unique properties, their hyperbolic dispersion bandwidth is fixed, which limits their tunability and flexibility for broader applications [39, 40].

Artificial HMMs overcome the limitations of natural materials by allowing precise control over hyperbolic dispersion characteristics. Such materials include multilayer configurations with alternating metallic and dielectric layers having thicknesses significantly smaller than the operational wavelength, yielding a Type II HMM. Common metals used include gold, silver, and aluminum while common dielectrics used include silica, and titanium dioxide [41, 42]. Nanowire-based platforms are another approach to achieve hyperbolic dispersion with one permittivity tensor element being negative (Type I HMM). Such platforms include metallic nanowires, and transparent conductive oxides [43–46].

In summary, these artificial material platforms enable the development of HMMs with custom hyperbolic dispersion properties.

2.5. Hyperbolic Nanoresonators

In this dissertation, hyperbolic nanospheroids composed of both plasmonic and dielectric materials are employed in geometries with different aspect ratios, including spherical, prolate, and oblate configurations. These structures enable precise control over electromagnetic fields through their resonant properties while offering complementary advantages from both dielectric and metallic material platforms.

The development of hyperbolic nanoresonators requires understanding the unique properties that both plasmonic and dielectric components contribute to the composite system. Plasmonic elements provide high field enhancement and subwavelength light confinement ca-

pabilities, while dielectric components offer low-loss operation and magnetic response functionality. The combination of these contrasting material properties enables the realization of hyperbolic dispersion characteristics, as detailed in Section 2.4.1, which are fundamental to achieving the extraordinary electromagnetic behaviors of these hybrid nanoresonators.

Metal nanoparticles exhibit the capability to confine electromagnetic radiation and operate as open cavity systems, forming the plasmonic foundation of hyperbolic nanoresonators. These open resonators demonstrate quality factors ($Q \sim 10 - 100$), which quantify how long light can be stored in the cavity relative to the energy lost per oscillation cycle, that are considerably reduced compared to their dielectric counterparts ($Q \sim 10^6$) due to losses through both radiative and non-radiative pathways. Although metallic systems sacrifice temporal confinement (lower Q), they excel in spatial confinement, concentrating fields into subwavelength volumes that produce intense electromagnetic hotspots. This field enhancement compensates for the reduced quality factor by generating considerably amplified electromagnetic intensities [47].

The behavior of conduction electrons in metallic systems has been discussed in Section 2.3 through the Lorentz-Drude model (the Drude part). While this model accurately describes bulk metallic properties, the optical response transforms substantially when particle dimensions become subwavelength. In the quasi-static limit, where nanostructures are much smaller than the optical wavelength and external fields can be assumed as spatially uniform, the optical response of small metallic particles is determined by their polarizability -— a function of geometry, material properties, and environment. For simple cases, analytical expressions like the Clausius-Mossotti relation [48–50] provide insight into the underlying physics. This approach reveals that the optical characteristics are governed by particle morphology, metallic dielectric properties, and environmental dielectric conditions. However, as particle dimensions approach or exceed the optical wavelength, these quasi-static approximations become invalid, necessitating full electromagnetic solutions.

Plasmons [51, 52] are collective oscillations of free electrons in a metal. Although they are quantum mechanical entities, their interaction with light in nanostructures is often accurately modeled with classical physics. This model describes the electrons moving together against the fixed background of positive metal ions when excited by an external electric field. These collective excitations form the basis for the strong electromagnetic coupling required in hyperbolic nanoresonator systems.

Surface plasmon polaritons (SPPs) [51–53] are propagating excitations that manifest at metal-dielectric interfaces as shown in Figure 2.5, providing one mechanism for electromagnetic confinement in hyperbolic nanoresonators. When electromagnetic waves couple to charge density oscillations at the interface, they generate electric fields localized near the surface. These surface-confined modes possess wave vectors exceeding those of free-space photons, creating a momentum mismatch that prevents direct optical excitation of SPPs without additional coupling mechanisms such as prisms, gratings, or surface roughness. The strong electromagnetic coupling produces SPPs with the dispersion relation:

$$k_{SPP} = k_0 \sqrt{\frac{\varepsilon_{metal}\varepsilon_{dielectric}}{\varepsilon_{dielectric} + \varepsilon_{metal}}}, \tag{2.51}$$

where $k_0 = \frac{\omega}{c}$ is the free-space wave vector, ε_{metal} is the permittivity of the metal, and $\varepsilon_{dielectric}$ is the permittivity of dielectric.

Various ways enable SPP excitation despite this momentum gap. Optically thin metallic films allow excitation through high-index substrates, providing the additional momentum required for SPP launch at the metal-air interface. Surface roughness and defects can also

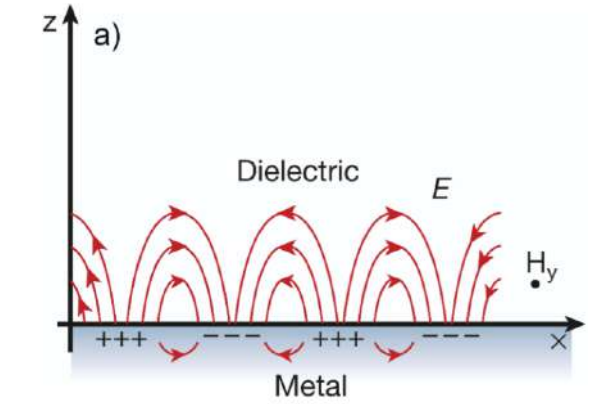

Figure 2.5: Surface plasmon polariton generation at the boundary between a dielectric and metallic material. Illustration of the electromagnetic field pattern within both the dielectric medium and the metal. (Figure adapted from [52]).

facilitate momentum transfer. Alternatively, periodic surface structures can supply the necessary momentum through diffraction. These coupling mechanisms become particularly relevant in the complex geometries of hyperbolic nanoresonators where multiple interfaces and surface features can facilitate SPP excitation.

Surface plasmon resonance (SPR) [51–53] is a label-free biosensing technique that detects analytes by measuring changes in the refractive index at a metal-dielectric interface. In a common configuration, a laser beam is reflected through a prism off a thin gold film, exciting surface plasmons. The extreme sensitivity of SPR allows it to detect sub-monolayer quantities and measure binding kinetics in real time. However, its sensing volume is not inherently localized, which often requires the use of a functionalized polymer layer to capture target molecules and generate a sufficient signal. While SPR demonstrates the sensitivity of plasmonic systems to environmental changes, its macroscopic nature hinders its use in nanoscale resonator designs.

Localized Surface Plasmon Resonance (LSPR) [51–53] represents a more directly relevant phenomenon for hyperbolic nanoresonator applications. LSPR occurs when electromagnetic radiation interacts with metal nanoparticles, specifically noble metals like gold and silver, causing collective coherent oscillations of the surface conduction electrons as shown in Figure 2.6. Unlike propagating SPPs, LSPR creates non-propagating surface plasmons confined to the nanoparticle surface. Resonance occurs when the frequency of incident electromagnetic radiation corresponds to the intrinsic oscillation frequency of the metallic surface electrons. This frequency resonance is susceptible to the shape, material composition, and size of the nanoparticle, as well as the dielectric constant of the surrounding medium. This tunability through geometric and material parameters makes LSPR particularly valuable for designing hyperbolic nanoresonators with specific optical responses.

The LSPR phenomenon manifests as sharp spectral absorption and scattering peaks in the visible to near-infrared range for noble metal nanoparticles. The displacement of the electron cloud relative to the positive ionic background generates intense localized electric fields at the nanoparticle surface. LSPR's highly localized sensing volume makes it extremely sensitive to changes in the local refractive index, forming the basis for LSPR-based sensing applications. The key advantages of LSPR over SPR include direct optical excitation without momentum matching requirements, highly localized sensing volumes that reduce bulk effects and eliminate the need for polymer matrices, simpler instrumentation with basic optical ex-

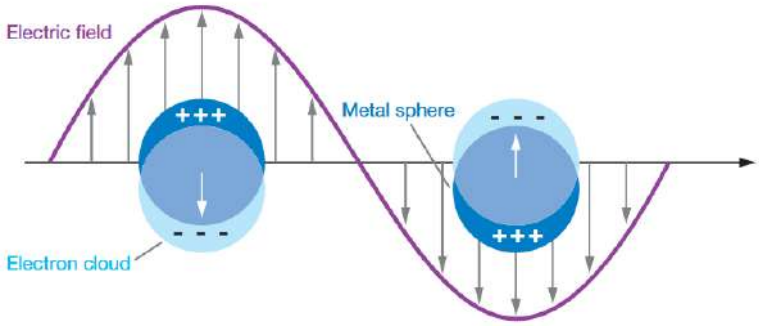

Figure 2.6: Depiction of an LSPR, where the electron cloud undergoes back-and-forth oscillations, causing the negatively charged electrons to shift relative to the positively charged ion lattice. (Figure adapted from [53]).

tinction measurements that are not temperature-sensitive, and the ability to tune resonance wavelengths through particle geometry.

Despite their high field enhancement capabilities, plasmonic components in hyperbolic nanoresonators face fundamental limitations that necessitate the integration of dielectric elements. The most significant constraint is material losses, which are noticeable even for noble metals in the visible range. Although these losses may be exploited for specific applications such as plasmonic heating or hot electron generation for catalysis, they are generally detrimental for resonator applications, causing Ohmic losses and reducing overall device efficiency. Another notable disadvantage is the lack of magnetic response for particles with simple geometries such as spheres or disks, limiting the ability to independently control magnetic field components. These limitations highlight the need for complementary dielectric components to achieve the full functionality required for hyperbolic nanoresonators.

High-index dielectric nanoparticles present a complementary solution to overcome the limitations of purely plasmonic systems in hyperbolic nanoresonators. Materials such as silicon, germanium, or gallium arsenide exhibit minimal absorption losses in the near-infrared range while maintaining high refractive indices [23, 54, 55]. The magnetic response of dielectric nanoparticles arises from displacement currents within the high-index material [23]. When electromagnetic radiation interacts with a dielectric nanoparticle, the oscillating electric field induces polarization currents that can circulate within the particle volume. For sufficiently high refractive indices, these displacement currents can generate both significant electric and magnetic dipole moments, effectively creating artificial magnetic resonances. This magnetic response, combined with the inherent electric response, allows dielectric nanoparticles to function as dual-resonant systems capable of independently controlling both electric and magnetic field components.

In summary, the combination of plasmonic and dielectric components in hyperbolic nanoresonator configurations leverages the advantages of both platforms while mitigating their individual limitations. The resulting hyperbolic dispersion enables unique electromagnetic properties not achievable with conventional materials, including hyperlensing, enhanced spontaneous emission, and directional light propagation. The nanospheroid geometry with tunable aspect ratios provides additional degrees of freedom for tailoring the optical response, allowing systematic exploration of the transition between spherical, prolate, and oblate configurations and their corresponding electromagnetic behaviors. These hyperbolic nanoresonators thus represent a new paradigm in nanophotonics, where the careful integration of contrasting material properties creates emergent functionalities that exceed the capabilities of either component

individually.

2.6. Introduction to Excitonic Materials

Excitonic materials are a class of materials that form bound electron-hole pairs referred to as excitons upon photon absorption. The excitons play an important role in their optical and electronic properties. These materials exhibit strong light-matter interactions and are particularly interesting for optoelectronic applications. Types of excitonic materials include zero-dimensional (0D) quantum dots, organic molecules, one-dimensional (1D) materials, layered materials, 2D materials, and three-dimensional (3D) materials as shown in Figure 2.7. Each of these materials has its advantages and challenges [56].

Excitons can be observed and studied under various temperature conditions, ranging from cryogenic temperatures [57, 58] (typically below 77 K) to room temperature [59, 60] (around 300 K). While cryogenic conditions often enhance excitonic effects by reducing thermal fluctuations and increasing exciton lifetimes, many excitonic materials exhibit robust excitonic behavior at room temperature, making them practical for real-world applications. For this dissertation, the focus is on room temperature excitonic phenomena and their applications in optoelectronic devices.

0D quantum dots [56] are semiconductors nanocrystals where electrons are confined in all three spatial dimensions. Example of such materials are II-IV compounds (cadmium sulfide (CdS)), and perovskite QDs. They exhibit high exciton binding energies and tunable bandgaps that can be adjusted by varying their sizes. Their high quantum yields and strong light absorption across a wide spectra range make them useful in applications like display technologies, and biomedical imaging. Their high exciton binding energies and strong oscillator strengths enable robust light-matter coupling even at room temperature, making them excellent candidates for strong coupling regimes in cavity systems. Their challenges include surface defects affecting quantum yield and complex synthesis control for size uniformity.

Organic molecules [56] including π-conjugated chains and J-aggregates exhibit Frenkel excitons with high binding energies and localized excitonic states. These materials are particularly suited for room-temperature excitonic devices due to their strong dipole moments and narrow absorption/emission linewidths. The high binding energies ensure that excitons remain stable at room temperature, preventing thermal dissociation that often occurs in inorganic semiconductors. The large transition dipole moments and high oscillator strengths in organic molecules facilitate strong light-matter coupling, enabling the formation of polaritons with large Rabi splitting in optical cavities. Their challenges include controlling molecular orientation, reducing non-radiative losses, and maintaining long-term stability under operational conditions.

Next, we move from 0D to 1D materials which exhibit confinement in two dimensions, with electrons free to move along one direction. Example of such materials include single-walled carbon nanotubes (SWCNTs), semiconductor nanowires, and polymer chains [56]. They exhibit unique anisotropic properties, high charge carrier mobilities, and large transition dipole moment. The large transition dipole moments and high density of states enhance the light-matter interaction strength, promoting strong coupling effects when integrated with optical cavities or plasmonic structures. Their challenges include bundle formation especially in carbon nanotubes, complex integration into devices, and surface defect sensitivity. Their applications include molecular-level imaging.

Layered materials [56] like III-VI semiconductors (gallium sulfide (GaS) and gallium selenide (GaSe)) exhibit large bandgaps and high excitonic binding energies. The III-VI semi-

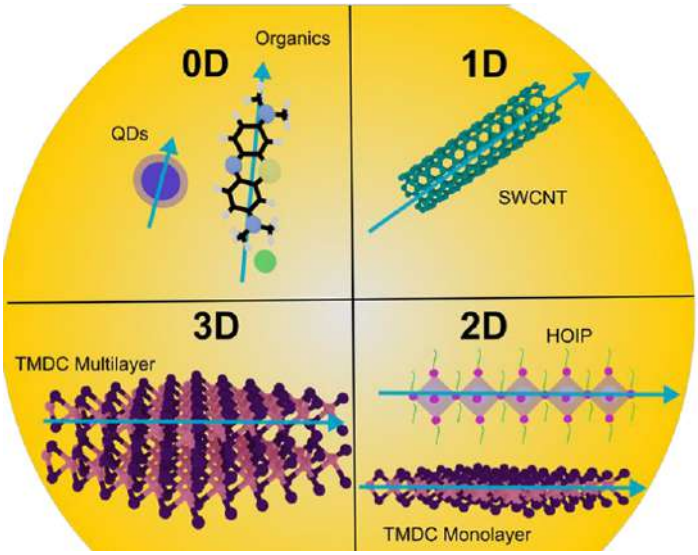

Figure 2.7: Dimensional classification of excitonic materials showing 0D quantum dots and organics, 1D carbon nanotubes, 2D TMDC monolayers and perovskites, and 3D TMDC multilayers [56].

conductors have unique structural properties where strong covalent bond exists within layers while weak van der Waals forces hold the layers together. Their advantages include layer dependent optical properties, high carrier mobility, and distinct in-plane and out-plane behaviors. The high excitonic binding energies and reduced dielectric screening in these layered structures enhance the coupling strength between excitons and photons, facilitating strong light-matter interactions for polariton formation. Their challenges include environmental stability, poor interface and contact issues in devices, and complex integration into devices.

Another type of layered material is black phosphorus [56] which is a 2D layered material. This material features a bandgap that can be adjusted from 0.3 eV in its bulk form to 1.5 eV when reduced to a monolayer. This tunability makes black phosphorus particularly interesting for optoelectronic applications spanning from the visible to infrared regions. The advantages of black phosphorus include enhanced exciton binding energies in few-layer forms, layer dependent optical properties, high carrier mobility, and distinct in-plane and out-plane behaviors. The enhanced exciton binding energies and anisotropic optical properties enable tunable strong coupling effects, allowing for wavelength-specific optimization of light-matter interactions. Their challenges include environmental stability.

2D materials like TMDCs [56] (MoS_2, $MoSe_2$, WS_2, and WSe_2) and HOIPs (Hybrid Organic-Inorganic Perovskites) are atomically thin materials where carriers are confined in one spatial direction (the out-of-plane direction), while they can move freely in the other two (the in-plane directions). These materials exhibit strong excitonic effects, a consequence of reduced dielectric screening and quantum confinement. Consequently, they possess large exciton binding energies ranging from 100 to 500 meV, which ensures remarkable stability even at room temperature. One of their strongest advantages is their tunable optoelectronic properties. The combination of high exciton binding energies, reduced dielectric screening, and large oscillator strengths makes 2D materials ideal for achieving strong coupling regimes with relatively low photon densities, enabling efficient polariton formation and propagation. Their challenges include substrate effect on properties, and sensitivity to environmental factors.

3D materials are bulk semiconductors [56] with excitonic effects, including traditional

semiconductors (e.g., Si, GaAs, InP) and bulk perovskites (e.g., $CsPbBr_3$, $CH_3NH_3PbI_3$). Their advantages include good stability, and high carrier mobility. While 3D materials typically exhibit weaker excitonic effects, bulk perovskites can still achieve strong coupling due to their large oscillator strengths and high exciton densities, particularly when incorporated into high-quality factor optical cavities. Their challenges include weaker excitonic effects at room temperature and less tunability compared to lower-dimensional materials.

2.6.1. Excitons in TMDCs

This section briefly examines the unique excitonic properties that make TMDCs particularly suitable for strong coupling applications. The bound electron-hole pairs binding energies in TMDCs are greater than those in bulk semiconductors. They support various excitonic states that have unique properties such as [56, 61]:

i. Bright excitons result from spin-allowed transitions and dominate the optical spectra of TMDCs. These excitons couple strongly with light and are responsible for the intense photoluminescence observed in monolayer TMDCs.

ii. Dark excitons are spin-forbidden transitions that cannot directly emit light due to spin and momentum mismatches. Although optically inactive under typical conditions, dark excitons can be activated using external stimuli such as magnetic fields or by coupling with plasmonic structures. Their long lifetimes and stability make them good candidates for quantum information storage.

iii. Trions, or charged excitons, form when an exciton interacts with an additional charge carrier (electron or hole). Trions exhibit distinct spectral signatures and are influenced by the carrier density in the material, which can be modulated through electrostatic gating.

iv. Biexcitons are two-bound excitons that exhibit nonlinear optical properties, such as enhanced two-photon absorption. These states have implications for high-efficiency light emission and lasing applications.

TMDCs have two inequivalent valleys (K and K') [61] in their Brillouin zone and enable valley excitons that have spin valley coupling. This is a fundamental property of TMDCs, such as MoS_2, $MoSe_2$, WS_2, and WSe_2. This property is unique to TMDCs and has significant implications for their optical and electronic properties. TMDCs also have prominent absorption peaks known as A and B excitons that correspond to the transitions at the K and K' valleys. These excitons exhibit high tunability and respond to various manipulation techniques, including electric and magnetic fields or mechanical strain.

To summarize, excitonic materials ranging from 0D to 3D materials support stable excitonic states and have the ability to achieve strong coupling phenomena when combined with other nanostructures like plasmonic and photonic nanostructures. While excitonic materials span various dimensions and compositions, TMDCs have a wide range of applications ranging from nonlinear optics to quantum information processing in the broader field of excitonic materials.

2.7. Integration of Excitons into Hyperbolic Nanoparticles

The integration of excitonic materials into photonic structures for strong light-matter coupling applications can be achieved through various approaches. These methods range from direct

incorporation of excitonic materials into device architectures to theoretical modeling using oscillator models that capture the essential physics of excitonic transitions. Understanding both approaches is crucial for designing and optimizing excitonic devices for strong coupling applications.

An important consideration in excitonic device design is that the specific physical origin of the excitonic transition becomes secondary to its optical response characteristics. If the excitonic effects in a material can be accurately described by a Lorentz oscillator model—capturing the resonance frequency, oscillator strength, and linewidth—-then the theoretical predictions and design principles remain valid regardless of whether the implementation uses actual excitonic materials or alternative systems that produce equivalent optical responses. This universality allows for flexible design approaches where the focus shifts from material constraints to optimizing the fundamental coupling parameters that govern strong light-matter interactions.

2.7.1. Material-Based Integration

Material-based integration involves the direct incorporation of excitonic materials into photonic structures such as optical cavities, metamaterials, and plasmonic systems.

For quantum dot integration [62], silicon nanocrystals are typically incorporated into silica or silicon nitride hosts by depositing alternating silicon-rich and stoichiometric dielectric layers with thicknesses of 2–7 nm, followed by high-temperature annealing to induce quantum dot formation. This technique provides precise control over the quantum dot density and size distribution, which is crucial for optimizing the coupling strength between the quantum dots and the optical modes.

For organic dyes or molecules [63], doping into silica matrices can be achieved using sol–gel techniques combined with dip-coating. In this process, silica sols are synthesized from tetraethyl orthosilicate (TEOS), ethanol, hydrochloric acid, water, and a surfactant (Triton X-100), with the organic dye introduced into the sol before gelation to ensure uniform distribution. Subsequent hydrolysis and condensation reactions at moderate temperatures (around 50 °C) form the silica network, while the coated substrates are withdrawn at controlled speeds to define the final film thickness. Annealing at a reduced temperature of 200 °C promotes condensation while preserving the dye, resulting in smooth, optically homogeneous silica films in which the dye molecules remain photoluminescent within the matrix.

Integration of 2D materials [64, 65] such as TMDCs can be achieved through mechanical transfer techniques, chemical vapor deposition (CVD), and molecular beam epitaxy (MBE). These methods allow atomically thin excitonic layers to be positioned at precise locations within photonic structures, enabling strong coupling with cavity modes or plasmonic resonances. The van der Waals bonding in these materials enables integration with diverse substrates without requiring lattice matching.

2.7.2. Lorentz-Oscillator Integration

The Lorentz oscillator model provides a theoretical framework for describing excitonic transitions and their integration into photonic structures. This framework shows that the physical origin of the excitonic response is secondary to its optical properties. Any system—whether based on actual excitons in quantum dots, organic molecules, 2D materials, or alternative physical mechanisms—that can be accurately described by the same Lorentz oscillator parameters will exhibit equivalent strong coupling behavior.

The excitonic contribution to the material permittivity is described by incorporating a Lorentz oscillator into the dielectric function [66, 67]:

$$\varepsilon_{ex}(\omega) = \frac{f\omega_{ex}^2}{\omega_{ex}^2 - \omega^2 - i\gamma_{ex}\omega}, \tag{2.52}$$

where ω is the angular frequency, f denotes here the oscillator strength, ω_{ex} is the exciton transition frequency, and γ_{ex} represents the exciton linewidth that accounts for dephasing and radiative damping. At resonance ($\omega = \omega_{ex}$), this expression simplifies to:

$$\varepsilon_{ex}(\omega_{ex}) = i\frac{f\omega_{ex}}{\gamma_{ex}}. \tag{2.53}$$

This simplified form clearly illustrates how the oscillator strength f directly determines both the real and imaginary parts of the permittivity at the resonance frequency, making it the key parameter for controlling the optical response regardless of the underlying physical mechanism.

The oscillator strength f is an important parameter that governs the coupling strength between excitons and photons. For integration into complex photonic structures, the excitonic contribution is added to the background permittivity of the host material:

$$\varepsilon_d \to \varepsilon_d + \varepsilon_{ex}(\omega). \tag{2.54}$$

This modification affects both the real and imaginary parts of the permittivity, influencing the dispersion and absorption characteristics of the composite material. The real part determines the phase velocity and refractive index, while the imaginary part governs absorption and radiative losses.

Moreover, multiple Lorentz oscillators can be used to model complex excitonic materials with multiple transition lines, such as TMDCs with A and B exciton transitions, or organic materials with vibronic progressions. This multi-oscillator approach provides a comprehensive description of the material response across broad spectral ranges, enabling accurate modeling of realistic device configurations.

Chapter 3

Strong Coupling of Light and Matter

Strong coupling between light and matter represents a regime where coherent energy exchange between the two domains dominates over dissipative processes, leading to the formation of hybrid light-matter states called polaritons. This chapter discusses the quantum mechanical framework for understanding strong coupling phenomena and examples of strong coupling in plasmonic nanostructures operating at room temperature.

3.1. Quantum Description of Strong Coupling

The fundamental quantum description of strong coupling is governed by the Jaynes-Cummings model [68], which models the interaction of a single two-level system with a single quantized cavity mode. In this framework, a quantum emitter is treated as a two-level system with a ground state $|g\rangle$ and excited state $|e\rangle$, separated by the transition energy $\hbar\omega_0$. The atomic Hamiltonian in the energy representation is expressed as:

$$\hat{H}_{\text{atom}} = E_g|g\rangle\langle g| + E_e|e\rangle\langle e|, \tag{3.1}$$

which can be rewritten by shifting the zero energy to $(E_g + E_e)/2$ as:

$$\hat{H}_{\text{atom}} = \frac{\hbar\omega_0}{2}\sigma_z, \tag{3.2}$$

where $\omega_0 = (E_e - E_g)/\hbar$ is the atomic transition frequency and:

$$\sigma_z = |e\rangle\langle e| - |g\rangle\langle g| \tag{3.3}$$

is the Pauli operator.

The quantization of the electromagnetic field is achieved by treating each independent radiation mode as a quantum harmonic oscillator. Each mode is uniquely identified by its wavevector $\mathbf{k}$ and polarization index α. In this quantum field description, the photon annihilation and creation operators $\hat{a}_k$ and $\hat{a}_k^\dagger$ satisfy the canonical commutation relation:

$$[\hat{a}_k, \hat{a}_k^\dagger] = 1. \tag{3.4}$$

The operators act on the number states $|n_k\rangle$ according to:

$$\hat{a}_k|n_k\rangle = \sqrt{n_k}|n_k - 1\rangle, \tag{3.5}$$

$$\hat{a}_k^\dagger|n_k\rangle = \sqrt{n_k + 1}|n_k + 1\rangle. \tag{3.6}$$

For a single cavity mode with frequency ω_c, the field Hamiltonian becomes:

$$\hat{H}_{\text{field}} = \sum_k \hbar\omega_k(\hat{a}_k^\dagger \hat{a}_k + 1/2) = \hbar\omega_c(\hat{a}^\dagger \hat{a} + 1/2). \tag{3.7}$$

The interaction between the atom and the electromagnetic field is mediated through the electric dipole coupling:

$$\hat{H}_{\text{int}} = -\hat{\mathbf{d}} \cdot \hat{\mathbf{E}}(\mathbf{r}), \tag{3.8}$$

where $\hat{\mathbf{d}}$ denotes the atomic dipole moment operator and $\hat{\mathbf{E}}(\mathbf{r})$ represents the electric field operator evaluated at the emitter's position. The dipole moment operator can be expressed in terms of the atomic raising and lowering operators as:

$$\hat{\mathbf{d}} = d_{10}(\hat{\sigma}_+ + \hat{\sigma}_-), \tag{3.9}$$

where

$$\hat{\sigma}_+ = |e\rangle\langle g|, \tag{3.10}$$

$$\hat{\sigma}_- = |g\rangle\langle e|, \tag{3.11}$$

are the atomic raising and lowering operators, and $d_{10} = \langle e|\hat{\mathbf{d}}|g\rangle$ is the transition dipole moment. The transition dipole moment quantifies the strength of the electric dipole coupling between the ground and excited states and determines the rate of spontaneous emission and absorption processes. For an electric dipole transition to be allowed, the transition dipole moment must be non-zero, which requires that the initial and final states have opposite parity. When the dipole coupling is combined with the quantized electromagnetic field, the interaction Hamiltonian becomes:

$$\hat{H}_{\text{int}} = \sum_k g_k\hbar(\hat{a}_k^\dagger + \hat{a}_k)(\hat{\sigma}_+ + \hat{\sigma}_-), \tag{3.12}$$

where g_k is the coupling strength parameter for mode k.

Under the rotating wave approximation, which neglects rapidly oscillating terms $\hat{a}_k\hat{\sigma}_+$ and $\hat{a}_k^\dagger\hat{\sigma}_-$ that oscillate at frequencies $\omega_k + \omega_0$, the interaction Hamiltonian simplifies to:

$$\hat{H}_{\text{int}} = \sum_k g_k\hbar(\hat{a}_k\hat{\sigma}_+ + \hat{a}_k^\dagger\hat{\sigma}_-). \tag{3.13}$$

The first term describes photon absorption creating an atomic excitation, while the second term describes photon emission destroying an atomic excitation. The transition matrix elements for these processes are:

$$\langle n_k - 1, 0|\hat{H}_{\text{int}}|n_k, 1\rangle = g_k\hbar\sqrt{n_k} \quad \text{(absorption)} \tag{3.14}$$

$$\langle n_k + 1, 1|\hat{H}_{\text{int}}|n_k, 0\rangle = g_k\hbar\sqrt{n_k + 1} \quad \text{(emission)} \tag{3.15}$$

where the joint states are denoted as $|n_k, i\rangle = |n_k\rangle \otimes |i\rangle$ with $i = 0, 1$ representing the atomic ground and excited states.

The complete Jaynes-Cummings Hamiltonian for a single mode is:

$$\hat{H}_{JC} = \frac{\hbar\omega_0}{2}\hat{\sigma}_z + \hbar\omega_c\hat{a}^\dagger\hat{a} + \hbar g(\hat{a}^\dagger\hat{\sigma}_- + \hat{a}\hat{\sigma}_+), \tag{3.16}$$

where g is the coupling strength parameter that characterizes the interaction strength in mode-exciton systems.

This Hamiltonian can be solved exactly in the single excitation subspace, which consists of the states $|e,0\rangle$ (atom excited, no photons) and $|g,1\rangle$ (atom in ground state, one photon). The Hamiltonian matrix in this subspace is:

$$\mathbf{H} = \begin{pmatrix} \hbar\omega_0 & \hbar g \\ \hbar g & \hbar\omega_c \end{pmatrix}. \tag{3.17}$$

Diagonalizing this matrix yields the eigenvalues:

$$E_\pm = \frac{\hbar(\omega_0 + \omega_c)}{2} \pm \frac{\hbar}{2}\sqrt{4g^2 + (\omega_0 - \omega_c)^2}, \tag{3.18}$$

which at zero detuning of the two resonant frequencies ($\omega_0 = \omega_c$) simplify to:

$$E_\pm = \hbar\omega_c \pm \hbar g. \tag{3.19}$$

The corresponding eigenstates are the dressed states or polaritons:

$$|P^\pm\rangle = \alpha|e,0\rangle \pm \beta|g,1\rangle, \tag{3.20}$$

where the Hopfield coefficients are given by:

$$|\alpha|^2 = \frac{1}{2}\left(1 + \frac{\Delta}{\sqrt{\Delta^2 + 4g^2}}\right), \tag{3.21}$$

$$|\beta|^2 = \frac{1}{2}\left(1 - \frac{\Delta}{\sqrt{\Delta^2 + 4g^2}}\right), \tag{3.22}$$

with $\Delta = \omega_0 - \omega_c$ being the detuning. The Hopfield coefficients quantify the relative weights of the atomic and photonic components in the polariton states. The energy difference between the upper and lower polariton branches defines the vacuum Rabi splitting energy:

$$\hbar\Omega_R = E_+ - E_- = 2\hbar g. \tag{3.23}$$

This splitting persists even in the absence of any photons initially in the cavity, demonstrating the fundamental role of vacuum field fluctuations in quantum electrodynamics. This anticrossing behavior and polariton formation is illustrated in Figure 3.1.

The extension to multiple identical emitters leads to the Tavis-Cummings model [70], where N emitters collectively interact with a single cavity mode. The collective spin operators are defined as:

$$\hat{S}^+ = \frac{1}{\sqrt{N}}\sum_{n=1}^{N}\hat{\sigma}_n^+, \tag{3.24}$$

$$\hat{S}^- = \frac{1}{\sqrt{N}}\sum_{n=1}^{N}\hat{\sigma}_n^-, \tag{3.25}$$

allowing the Hamiltonian to be written as:

$$\hat{H}_{TC} = \hbar\omega_0\hat{S}^+\hat{S}^- + \hbar\omega_c\hat{a}^\dagger\hat{a} + \hbar g_N(\hat{a}^\dagger\hat{S}^- + \hat{a}\hat{S}^+). \tag{3.26}$$

Here, the interaction rate is a collective one, i.e. a collective coupling strength that is defined as:

$$g_N = \sqrt{N}g_1 \tag{3.27}$$

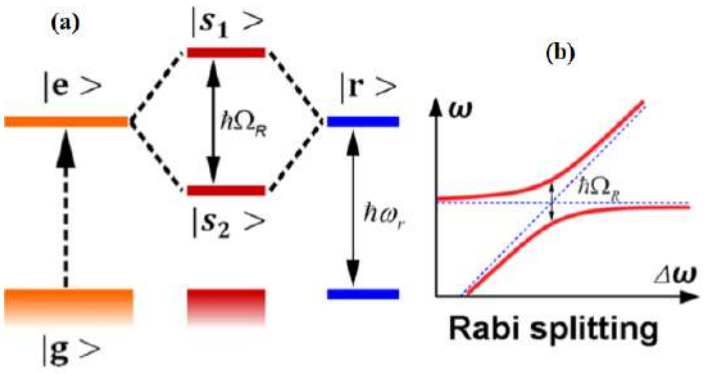

Figure 3.1: Strong coupling and vacuum Rabi splitting. (a) Energy level diagram showing the interaction between ground state $|g\rangle$, upper polariton $|s_1\rangle = |P^+\rangle$ and lower polariton $|s_2\rangle = |P^-\rangle$, and a resonant cavity mode $|r\rangle$ at frequency ω_r. The coupling strength g facilitates energy exchange between the emitter ($|e\rangle$) and cavity mode ($|r\rangle$), resulting in the vacuum Rabi splitting $\hbar\Omega_R = 2\hbar g$. (b) Spectroscopic signature of strong coupling showing the characteristic anticrossing behavior as a function of detuning, demonstrating the formation of upper and lower polariton branches separated by the Rabi splitting Ω_R. (Figure adapted from [69]).

with g_1 being the single-emitter coupling. This $\sqrt{N}$ enhancement arises from the constructive interference of the individual emitter-field interactions and enables strong coupling even when individual emitters are weakly coupled.

The physical origin of this scaling can be understood through the fundamental coupling expression $g = N\mu|E|$, where N is the number of molecules, μ is the molecular transition dipole moment, and $|E|$ is the local electric field enhancement. Since the oscillator strength f scales linearly with the number of molecules ($f \propto N$), the coupling strength follows $g \propto \sqrt{N} \propto \sqrt{f}$. This relationship has been shown for core-shell plasmonic systems, where the vacuum Rabi splitting exhibits a linear dependence on $\sqrt{f}$, confirming that classical electromagnetic treatments can accurately capture the essential physics of quantum light-matter interactions [66]. This scaling demonstrates that coherent coupling can be achieved through either increasing the number of emitters or enhancing the local electromagnetic field through optimized plasmonic geometries.

In plasmon-exciton systems, this collective enhancement enables strong coupling even when individual emitters experience only moderate field enhancement, providing a practical route to strong coupling through ensemble effects in core-shell geometries [66] and other plasmonic nanostructures [71]. The corresponding vacuum Rabi splitting becomes:

$$\hbar\Omega_R = 2\hbar g_N = 2\hbar\sqrt{N}g_1 \tag{3.28}$$

providing a practical route to strong coupling through ensemble effects.

A fundamental limitation of the Tavis-Cummings model is its breakdown for large emitter numbers or high optical densities, as it requires all system rates and frequencies to be small compared to the cavity's free spectral range ν_{FSR} (defined as the reciprocal of the photon round-trip time). Specifically, the model breaks down when either:

$$\nu_{FSR} \ll g_N \quad \text{(ultrastrong coupling regime)} \tag{3.29}$$

$$\nu_{FSR} \ll \frac{g_N^2}{\gamma_{QE}}. \tag{3.30}$$

3.2. Conditions for Strong Coupling

The transition from weak to strong coupling is governed by the relative magnitudes of the coupling strength and the dissipation rates in the system. When losses are included phenomenologically by introducing complex frequencies $\omega_0 - i\gamma_{QE}$ (where γ_{QE} is the atomic decay rate into non-cavity modes) for the emitter and $\omega_c - i\gamma_{cav}$ (where γ_{cav} is the cavity photon decay rate) for the cavity, the eigenvalues in the single excitation subspace become:

$$E_{\pm} = \frac{(\omega_0 + \omega_c)}{2} - i\frac{(\gamma_{QE} + \gamma_{cav})}{2} \pm \frac{1}{4}\sqrt{4g^2 - (\Delta - i(\gamma_{QE} - \gamma_{cav}))^2}, \tag{3.31}$$

where $\Delta = \omega_0 - \omega_c$ is the detuning. The relative coupling strength of a system is characterized by three parameters: the coupling strength g, the photon decay rate of the confined field γ_{cav}, and the non-resonance decay rate of the molecules γ_{QE}. In experimental practice, these decay rates can be determined from the linewidths of the uncoupled cavity resonance and molecular absorption features.

Several criteria have been established to determine whether a system exhibits strong coupling, each with different levels of stringency and practical applicability. Firstly, for the splitting to be experimentally observable and according to Sparrow's criterion [72] for two resolvable peaks, two distinct peaks are visible in the spectrum, with the midpoint between them showing a minimum in intensity. However, care must be taken when applying this criterion, as spectral splitting can also arise from other phenomena [73, 74] such as Fano interference between quantum emitters and plasmonic resonances, which can occur entirely in the weak coupling regime. Therefore, the observation of two peaks alone is not sufficient evidence for strong coupling without additional analysis of the dispersion behavior and anticrossing characteristics.

Secondly, the most fundamental criterion for strong coupling requires that the Rabi splitting remains real-valued. For the system to exhibit coherent energy exchange, the coupling strength must exceed the difference between the individual decay rates [75]:

$$2g > \frac{|\gamma_{QE} - \gamma_{cav}|}{2}. \tag{3.32}$$

This condition preserves the real nature of the square root term in equation 3.31, avoiding overdamped dynamics that eliminate oscillatory behavior. The key distinction of this criterion lies in its comparison of coupling strength with the loss rate difference between uncoupled modes, not with experimentally observed splitting versus uncoupled linewidths. This approach reveals that strong coupling can occur even with high system dissipation, provided the uncoupled resonances have similar loss characteristics. As a result, strong coupling may persist despite polariton linewidths being too broad for experimental detection of the splitting.

Thirdly, the most stringent and commonly adopted criterion combines both previous requirements and ensures clear spectroscopic visibility. This condition requires that the splitting be greater than the average linewidth of the uncoupled resonators [76, 77]:

$$\Omega_R > \frac{|\gamma_{QE} + \gamma_{cav}|}{2} \tag{3.33}$$

or equivalently:

$$2g > \frac{|\gamma_{QE} + \gamma_{cav}|}{2}. \tag{3.34}$$

This criterion ensures that the energy difference between the polariton modes is larger than their combined linewidths, guaranteeing both the reality of the splitting and its experimental

observability. The condition can be derived by requiring that the real part of the energy splitting exceeds the imaginary part, which after algebraic manipulation yields the requirement that the coupling strength must be greater than the average of the decay rates. This criterion is the preferred standard in most experimental studies as it provides a clear, unambiguous threshold for strong coupling that directly relates to observable spectroscopic features. For this dissertation, the criterion used is equation 3.33.

The avoided crossing behavior, clearly visible in anticrossing dispersion measurements such as shown in Figure 3.1(b), serves as the definitive signature of strong coupling and appears whenever the coupling rate Ω_R exceeds the relevant damping rates according to the chosen criterion.

3.3. Strong Coupling in Plasmonic Nanostructures

This section discusses strong coupling in plasmonic nanostructures as the current state-of-the-art baseline for subsequent relation to the topic of this dissertation, in which hyperbolic nanospheroids composed of a plasmonic metal and dielectric are investigated for coupling to excitons.

Plasmonic nanostructures provide one of the most effective platforms for achieving strong light–matter interactions at room temperature. In these systems, localized surface plasmon resonances (LSPRs) confine electromagnetic fields at subwavelength scales, producing intense local field enhancements. When coupled to excitonic materials such as quantum dots, molecular dyes, J-aggregates, and two-dimensional (2D) semiconductors, strong plasmon–exciton hybridization occurs. The resulting coupling strength depends primarily on spectral overlap, spatial proximity, and electromagnetic mode confinement. This section reviews experimental demonstrations of strong coupling in plasmonic nanostructures, organized by geometry.

The simplest approach to achieving strong coupling in plasmonic systems begins with individual nanoparticles that support localized surface plasmon resonances (LSPRs). These single-particle resonators serve as the fundamental building blocks for understanding light-matter interactions, where the particle geometry, size, and material composition directly determine the coupling efficiency with nearby quantum emitters. By examining single nanoparticle systems first, we establish the baseline coupling mechanisms that will be enhanced and modified in more complex architectures.

3.3.1. Single Nanoparticle Resonators

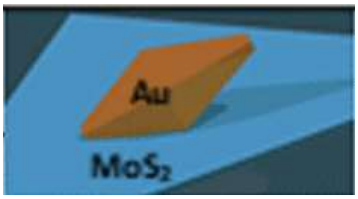

Figure 3.2: Schematic diagram of plasmonic nanostructures consisting of Gold bipyramids and MoS_2 monolayers (Figure adapted from [78]).

Single nanoparticles demonstrate strong coupling across a broad range of Rabi splitting values from 55 meV to 450 meV at room temperature. Gold bipyramids coupled to MoS_2 monolayers as shown in Figure 3.2 give Rabi splitting values of approximately 55 meV for 70-nm long bipyramids, increasing to 80 meV for 100-nm structures, with coupling strength depending

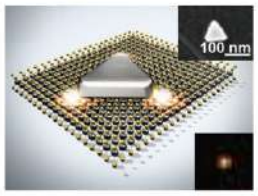

Figure 3.3: Schematic diagram of plasmonic nanostructures consisting of silver nanoprisms coupled to WS_2 monolayers (Figure adapted from [81]).

on both tip radius and length, requiring sharp tips with radii less than 7 nm for optimal field enhancement [78]. Gold nanocubes with PIC J-aggregates exhibit splitting of approximately 100 meV through electrostatic interactions, while similar systems with thiacarbocyanine dye achieve 120 meV [79, 80].

Building upon the success of gold nanostructures, researchers have explored silver nanoparticles, which typically exhibit sharper plasmon resonances and can achieve even larger coupling strengths due to their superior optical properties, albeit with reduced chemical stability. One example of the use of silver in this application are Ag nanoprisms coupled to WS_2 monolayers as shown in Figure 3.3, which demonstrate 120 meV splitting with the capability to couple with both neutral excitons and charged excitons (trions) [81].

Moving beyond simple two-level systems, more complex excitonic configurations can be employed to create multi-component polariton states. Biexcitonic systems, which involve multiple excitonic transitions, demonstrate how strong coupling can be extended to create even richer hybrid light-matter states. Biexcitonic systems operating at room temperature reach splitting values around 163-175 meV, with Au@Ag nanocuboids coupled to DBI and JC-1 J-aggregates exhibiting double Rabi splitting with values of 163 meV and 175 meV respectively, creating multicomponent polariton nanostructures with magneto-optical activity [82]. Au@Ag nanocuboids with PIC J-aggregates demonstrate 196 meV splitting, illustrating the advantages of hybrid metal composition for matching plasmonic resonances to J-aggregate frequencies [83].

Hollow gold nanoprisms coupled to PIC J-aggregates demonstrate enhanced performance with 198 meV splitting due to strong electric field generation at tips and within the central cavity, providing increased surface area and more effective field localization compared to solid counterparts [84]. Additional single nanoparticle systems demonstrate coupling with quantum dots, where gold nanorods achieve substantial Rabi splitting of approximately 234 meV with individual quantum dots when positioned in wedge nanogap cavity configurations [12].

Silver nanoparticles show even larger coupling strengths, with silver nanodisks coupled

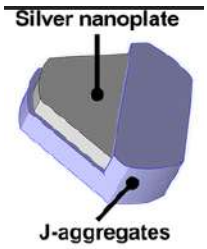

Figure 3.4: Schematic diagram of plasmonic nanostructures consisting of silver nanoprisms coupled with tetrachlorobenzimidazolocarbocyanine (JC-1) J-aggregates (Figure adapted from [85]).

to TDBC J-aggregates achieving 350 meV splitting, and silver nanoprisms with lead halide perovskites achieving similar values of approximately 350 meV at room temperature, leveraging strong absorption and oscillator strengths that remain stable under ambient conditions [86, 87]. The coupling strength can be tuned in situ, as was demonstrated in a system composed of silver nanoprisms coupled with tetrachlorobenzimidazolocarbocyanine (JC-1) J-aggregates as shown in Figure 3.4. These achieve very large coupling strengths, yielding Rabi splitting on the order of 450 meV under ambient conditions with pH-dependent tunability, where splitting decreases from 450 meV at pH 8-11 to approximately 200 meV at pH 2.5 [85].

3.3.2. Nanoparticle Dimers

Figure 3.5: Schematic diagram of plasmonic bowtie antenna with quantum dot in the gap where the field enhancement is maximum (Figure adapted from [88]).

While single nanoparticles demonstrate substantial coupling strengths up to 450 meV, even greater field enhancement and coupling efficiency can be achieved by creating closely spaced nanoparticle pairs. The key advantage lies in the formation of gap plasmon modes in the narrow spaces between metallic particles, where electromagnetic fields become highly concentrated and can interact more strongly with quantum emitters positioned within these "hot spots." This geometric configuration represents the next logical step in complexity, building upon single-particle physics while introducing the powerful concept of field localization through particle proximity.

Santhosh et al. [88] achieved vacuum Rabi splitting by coupling semiconductor quantum dots to silver bowtie plasmonic cavities as shown in Figure 3.5, achieving coupling rates as high as 120 meV even with a single QD. The study employed electron beam lithography to fabricate bowties with gaps of approximately 17-30 nm and used interfacial capillary forces to position CdSe/ZnS quantum dots within the gaps, with polarization-dependent experiments confirming that the observed splitting originates from coupling between the longitudinal plasmon resonance and the quantum dot excitons.

DNA double-strand assembly allows creation of 40 nm gold nanoparticle dimers as shown in Figure 3.6 with controlled incorporation of five dye molecules in the gap, achieving coupling strengths ranging from 50 to 150 meV when interparticle distances decrease below 2 nm [89]. However, only 3% of studied dimers displayed hybrid coupled modes, potentially due to transition dipoles not being appropriately oriented or positioned [89]. Despite this drawback, DNA origami templates are, nonetheless, a promising approach as they enable precise assembly of nanoparticle dimers with approximately 5 nm separation. This precision combined with few-nanometer gaps can lead to strong coupling with few J-aggregates and Rabi splitting of approximately 150 meV [90]. The coupling strength follows a correlation with particle radius

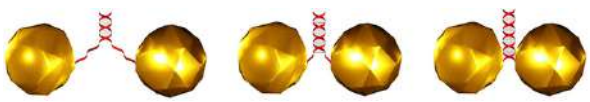

Figure 3.6: Schematic diagram of plasmonic nanostructures consisting of DNA double-strand assembly with gold nanoparticle dimers (Figure adapted from [89]).

($g \sim 1/R^n$ with $n = 0.63$), showing enhanced coupling in particles with reduced dimensions due to improved field confinement [90].

3.3.3. Nanoparticle-on-Mirror (NPoM) Configurations

The success of nanoparticle dimers in achieving enhanced coupling through gap plasmons naturally leads to an even more controlled and reproducible geometry: nanoparticle-on-mirror (NPoM) configurations. Unlike dimers where precise gap control between two curved surfaces presents fabrication challenges, NPoM systems offer the advantage of a perfectly flat mirror surface that ensures consistent and predictable gap dimensions. This configuration not only maintains the benefits of gap plasmon enhancement but also provides superior reproducibility and the potential for single-molecule studies, representing a significant advancement in both fundamental understanding and practical implementation.

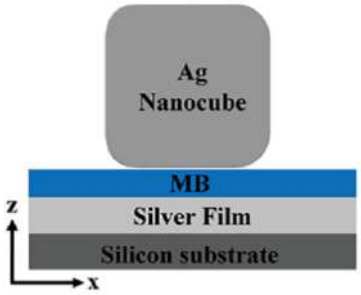

Figure 3.7: Schematic diagram of plasmonic nanostructures consisting of Silver nanocube-on-mirror systems with methylene blue J-aggregates (Figure adapted from [91]).

NPoM configurations prove effective for achieving large coupling strengths through gap plasmons formed between nanoparticles and flat mirror surfaces. The ultimate goal of such structures is single-molecule strong coupling represents a remarkable achievement in NPoM systems, where individual Cy5 molecules positioned in sub-5 nm gaps using DNA origami demonstrate mean Rabi splitting of 80 meV across more than 200 structures, with the presence of single molecules enhancing optical emission due to high local density of optical states while disrupting cavity scattering [92].

Dynamic imaging approaches using chlorophyll-a in NPoM systems demonstrate averaged coupling strength of approximately 125 meV and provide methods for monitoring coupling dynamics in real-time [93]. NPoM systems with transition metal dichalcogenides show similar coupling strengths, with WSe_2 multilayers achieving 140 meV splitting while monolayers show insufficient coupling due to limited interaction with strongly confined gap plasmon modes [94]. Silver nanocubes with WS_2 monolayers reach 145 meV splitting [95], while gold nanoprisms with WS_2 demonstrate 163 meV splitting with precise control over exciton strength through electromagnetic environment manipulation by adjusting spacer thickness [96].

Silver nanocube-on-mirror systems as shown in Figure 3.7 with methylene blue J-aggregates achieve 170 meV splitting, with coupling strength dependent on both dye concentration and nanoparticle size, where the relationship between nanoparticle size and coupling strength is consistent across different cube sizes [91]. Hu et al. [97] studied the strong coupling phenomena in a plasmonic-QD system consisting of QDs integrated into plasmonic NPoM as shown in Figure 3.8, fabricated with a yield of approximately 70% for strong coupling of excitons to

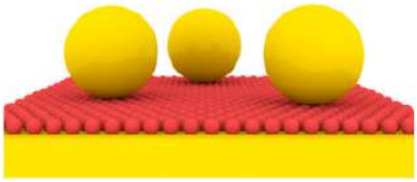

Figure 3.8: Schematic diagram of plasmonic nanostructures consisting of QDs integrated into plasmonic NPoM (Figure adapted from [97]).

plasmon modes by varying QD sizes, achieving an average Rabi splitting of 200 meV.

Gold nanocubes on gold films with PIC J-aggregates show splitting of 345-377 meV, approximately 2.5 times higher than similar hybrids on ITO substrates due to significant electric field amplification at the upper corners of the cube-on-film geometry under ambient conditions [79]. Further investigations show that single Atto647 molecules in similar NPoM configurations can achieve Purcell enhancements exceeding 1000 with emission lifetime decreased from approximately 2.5 ns to below 0.3 ns [98].

3.3.4. Metasurfaces and Hybrid Nanostructures

The individual nanostructure approaches discussed thus far—single particles, dimers, and NPoM configurations—excel at achieving strong coupling in localized regions but are inherently limited by their discrete nature. To scale up these phenomena for practical applications and to introduce additional degrees of control over electromagnetic fields, researchers have turned to metasurfaces and hybrid nanostructures. These extended platforms combine the proven coupling mechanisms of individual nanostructures with the collective behavior of periodic arrays, enabling both enhanced coupling strengths through cooperative effects and new functionalities that emerge from the interplay between multiple resonant elements.

Beyond single particles and dimers, metasurfaces and hybrid nanostructures provide additional versatile platforms for plasmon-exciton strong coupling. Metasurfaces, defined as two-dimensional metamaterials with subwavelength thickness, enable precise control over electromagnetic wave manipulation. For example, metasurfaces composed of nanoholes in optically thin silver films and coated with J-aggregates exhibit a coupling strength with a linear dependence on the square root of the number of J-aggregates, achieving Rabi splitting of 300 meV [99].

More broadly, hybrid nanostructures combine plasmonic, photonic, and dielectric components to leverage their individual strengths and achieve enhanced coupling phenomena. For instance, Tsargorodska et al. [100] studied strong coupling in a system of gold arrays and polypeptide maquettes. Using a coupled harmonic oscillator model, they achieved plasmon-

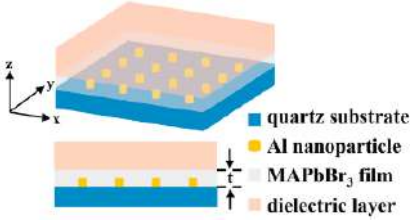

Figure 3.9: Schematic diagram of a hybrid nanostructure consisting of a methylammonium lead bromide thin film on top of an array of aluminium nanoparticles [71].

exciton coupling energies from 80 to 210 meV, with a coupling strength that showed a linear dependence on the square root of the dipole density. Another example is provided by the system shown in Figure 3.9, where perovskite organic-inorganic films are combined with aluminum nanoparticles. This structure demonstrates plasmonic-excitonic coupling with a strength that scales with the square root of the oscillator strength, yielding Rabi splitting values of 230 meV [71].

3.3.5. Specialized Configurations

Beyond the conventional geometries explored in the previous sections, the field has developed several specialized configurations that address specific challenges or exploit unique physical phenomena. These advanced approaches either push the boundaries of spatial control to achieve ultimate precision in coupling interactions, or introduce additional degrees of freedom such as chirality and material heterogeneity that open new pathways for both fundamental studies and applications. While these configurations may not always achieve the highest absolute coupling strengths, they offer unique capabilities that complement the established platforms and provide insights into unexplored aspects of strong coupling physics.

Additional plasmonic nanostructure configurations extend the versatility of strong coupling systems beyond conventional geometries. Tip-enhanced strong coupling (TESC) utilizes sharp scanning metal tips positioned close to metal surfaces, creating nanocavities that couple with single quantum emitters to produce mode splitting from 70 to 163 meV, with tip positioning providing precise control over coupling strength at sub-nanometer precision [101].

Chiral materials introduce additional degrees of freedom through circular dichroism effects, where chiral J-aggregates attached to bimetallic nanocuboids produce bisignate signals in CD spectra with mode splitting up to 214 meV, demonstrating that hybrid modes can be more easily distinguished in CD response due to smaller line width and bisignate line shape compared to extinction measurements [102]. Left-handed and right-handed plasmonic dimers created with DNA origami show chiroptical hybridization with opposite CD signal signs, demonstrating Rabi splitting of 205 meV and 199 meV respectively, where CD spectroscopy proves more helpful in characterizing chiral hybrids with multiple adjacent plasmon resonance modes [103].

Bimetallic nanostructures offer advantages by combining properties of different metals, with Ag-Au-alloyed nanorings achieving splitting values exceeding 300 meV with TDBC J-aggregates through enhanced electromagnetic fields within central holes that facilitate the transition from weak to strong coupling via galvanic displacement processes [104].

In summary, this systematic exploration from single nanoparticles to complex hybrid structures reveals how plasmonic strong coupling has evolved from a fundamental quantum optical phenomenon to a versatile platform technology. Each configuration builds upon the principles established by simpler geometries while introducing new capabilities: single particles establish the basic coupling mechanisms, dimers and NPoM configurations enhance field confinement through gap plasmons, metasurfaces enable scaling and new functionalities, and specialized configurations push the boundaries of control and introduce novel physics. This hierarchical understanding provides the foundation for designing next-generation strong coupling systems, including the hyperbolic nanospheroid geometries that represent the focus of this dissertation, where the combination of plasmonic enhancement and hyperbolic dispersion creates new opportunities for room-temperature quantum optical applications.

Chapter 4

Methods

With the fundamental material concepts introduced in Chapter 2 and Chapter 3, this chapter presents the computational and numerical methods used to investigate strong coupling in hyperbolic multilayer nanospheroids containing excitonic materials. The methodological approach combines several complementary techniques: effective medium theory to characterize the bulk optical properties of multilayer systems, finite-difference time-domain (FDTD) simulations for detailed electromagnetic field analysis, T-matrix calculations for rigorous scattering analysis of anisotropic particles, and coupled harmonic oscillator models to describe the strong coupling dynamics. Each method addresses specific aspects of the complex physics involved in the multilayer/hyperbolic nanospheroid systems.

4.1. Effective Medium Theory

Calculation of the complex optical behavior of nanoparticle ensembles can be simplified through effective medium theory. This theory replaces the heterogeneous distribution of permittivity—arising from distinct contributions of particles and their surrounding medium—with a single, homogeneous effective permittivity. While several approaches exist for calculating this effective permittivity, the Maxwell-Garnett approximation is often used due to its relative simplicity and decent reliability. An anisotropic multilayer composite exhibiting uniaxial symmetry is examined. The structure's alternating metallic and dielectric layers create intrinsic anisotropy, necessitating separate treatment of the permittivity along two primary directions: parallel ($\varepsilon_{\parallel}$) and perpendicular ($\varepsilon_{\perp}$) to the layer interfaces. The analysis employs a generalized Maxwell-Garnett framework to derive analytical expressions for the effective permittivities [28, 105, 106]. This approach allows one to recast the internal multilayer structure of spheroidal nanoparticles into a homogeneous permittivity. Such an effective permittivity can then be used for particles with various aspect ratios, including an example with an aspect ratio of 1, such as the sphere shown in Figure 4.1.

The fill fraction (f_m) defines the relative proportions of metallic and dielectric layers in the system:

$$f_m = \frac{d_m}{d_m + d_d}, \tag{4.1}$$

where d_m is the total thickness of the metallic layers, and d_d is the total thickness of the dielectric layers. This parameter describes the ratio of the metal's contribution to the total material composition and plays an important role in determining the effective permittivities.

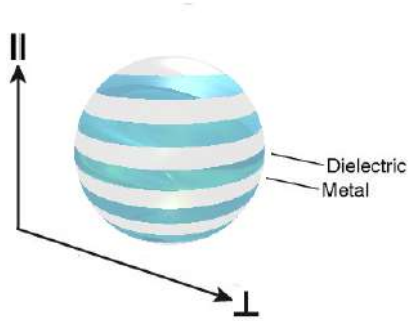

Figure 4.1: Schematic of a spherical multilayer system (aspect ratio = 1), with alternating dielectric and metallic layers. The perpendicular direction is along the radial direction, and the parallel direction is tangential to the spherical surface at any point.

4.1.1. Effective Perpendicular Permittivity

As discussed previously, the electric displacement $\vec{D}$ is proportional to the electric field $\vec{E}$, $\vec{D} = \bar{\varepsilon}_{\text{eff}}\vec{E}$, where ε_{eff} denotes the overall effective medium. The effective perpendicular permittivity is determined by averaging the electric displacement ($D_\perp$) across the layers, assuming the continuity of the electric field ($E_\perp$).

i. From the continuity conditions for the tangential component of $\vec{E}$ across the interfaces one obtains:

$$E_\perp^m = E_\perp^d = E_\perp. \tag{4.2}$$

ii. The total displacement field in the perpendicular direction is thus:

$$D_\perp = f_m D_\perp^m + (1 - f_m) D_\perp^d, \tag{4.3}$$

where $D_\perp^m = \varepsilon_m E_\perp$ is the displacement in metallic layers and $D_\perp^d = \varepsilon_d E_\perp$ is the displacement in dielectric layers.

iii. Substituting and solving for the effective perpendicular permittivity $\mathbf{D} = \varepsilon_{\text{eff}}\mathbf{E}$:

$$\begin{aligned} E_\perp^m &= E_\perp^d = E_\perp, \\ D_\perp &= f_m D_\perp^m + (1 - f_m) D_\perp^d, \\ \varepsilon_\perp^{\text{eff}} E_\perp &= f_m \varepsilon_m E_\perp + (1 - f_m)\varepsilon_d E_\perp, \\ \varepsilon_\perp^{\text{eff}} &= f\varepsilon_m + (1 - f_m)\varepsilon_d. \end{aligned}$$

Thus, the effective permittivity in the perpendicular direction is:

$$\varepsilon_\perp = f_m \varepsilon_m + (1 - f_m)\varepsilon_d. \tag{4.4}$$

4.1.2. Effective Parallel Permittivity

The effective parallel permittivity is derived by assuming continuity of the displacement field ($D_\parallel$) across the layers and averaging the electric fields.

i. The displacement fields are continuous across interfaces:

$$D_\parallel^m = D_\parallel^d = D_\parallel \tag{4.5}$$

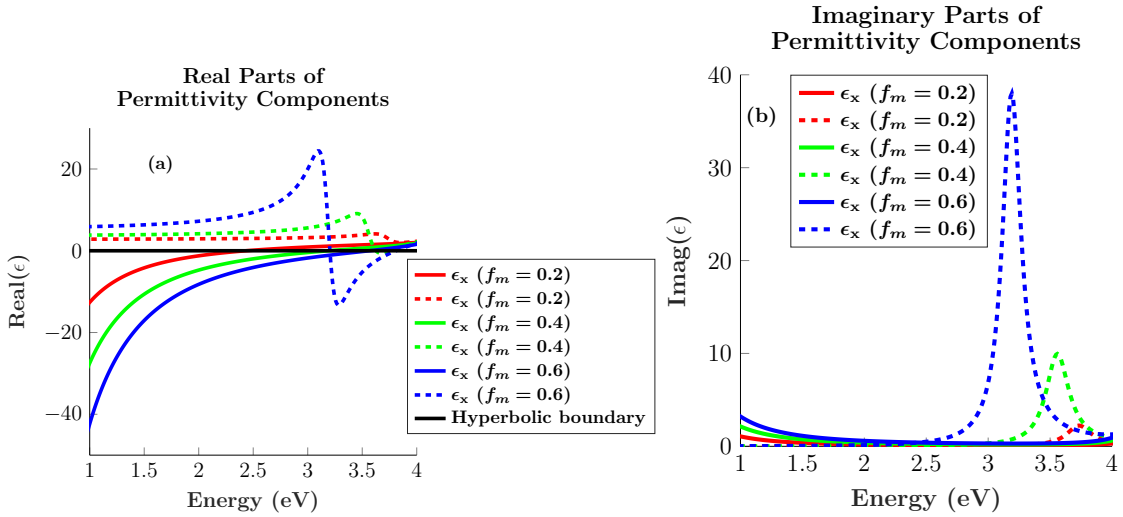

Figure 4.2: Plot of the (a) real part of the permittivity components, (b) imaginary part of the permittivity components. The subsequent lines represent a variable metal fill factor f_m.

ii. The total electric field in the parallel direction is:

$$E_{\parallel} = f_m E_{\parallel}^m + (1 - f_m) E_{\parallel}^d \tag{4.6}$$

iii. Using the constitutive relations and solving for the effective parallel permittivity:

$$\begin{aligned}
D_{\parallel}^m &= D_{\parallel}^d = D_{\parallel}, \\
E_{\parallel} &= f_m E_{\parallel}^m + (1 - f_m) E_{\parallel}^d, \\
\varepsilon_m E_{\parallel}^m &= \varepsilon_d E_{\parallel}^d = \varepsilon_{\text{eff}}^{\parallel} E_{\parallel}, \\
E_{\parallel} &= f_m \frac{D_{\parallel}}{\varepsilon_m} + (1 - f_m) \frac{D_{\parallel}}{\varepsilon_d}, \\
\frac{1}{\varepsilon_{\parallel}} &= \frac{f_m}{\varepsilon_m} + \frac{1 - f_m}{\varepsilon_d}, \\
\varepsilon_{\parallel} &= \frac{\varepsilon_m \varepsilon_d}{f_m \varepsilon_d + (1 - f_m)\varepsilon_m}.
\end{aligned}$$

Thus, the effective permittivity in the parallel direction is:

$$\varepsilon_{\parallel} = \frac{\varepsilon_m \varepsilon_d}{f_m \varepsilon_d + (1 - f_m)\varepsilon_m}. \tag{4.7}$$

As an example, using silver optical constants from Palik and silica ($n = 1.5$), we calculate the effective permittivities for various fill fractions ($f_m = 0.2,\ 0.4,\ 0.6$). The results exhibit hyperbolic dispersion, where $\mathrm{Re}(\varepsilon_x)$ and $\mathrm{Re}(\varepsilon_z)$ have opposite signs across certain energy ranges, with the hyperbolic boundary occurring where $\mathrm{Re}(\varepsilon_x) = 0$, as demonstrated in Figure 4.2. Such an averaged, effective and uniaxial permittivity can then be used in subsequent calculations, in which the internal complexity of a hyperbolic nanoparticle is neglected and described only by a simple diagonal permittivity tensor.

4.2. FDTD Method

The finite-difference time-domain (FDTD) method is a 3D full-wave electromagnetic approach commonly used for modeling nanophotonic devices, processes, and materials [107]. This numerical approach solves Maxwell's equations given in Section 2.1 in their time-domain representation by discretizing both time and space using a grid and applying central finite-difference approximations for temporal and spatial derivatives [108, 109].

An essential feature of FDTD is use of the Yee lattice [108], which offsets the electric and magnetic fields in both time and space. This offset improves numerical stability and accuracy by ensuring updates to the electric and magnetic field components are synchronized in a leapfrog manner [110]. Electric fields are calculated at half-time steps, while magnetic fields are calculated at full-time steps, ensuring interdependency between the updates. In FDTD, each field component is solved at a slightly different location within the grid cell, with the simulation domain being the space truncated by the simulation region and discretized by the mesh [111].

FDTD simulations require proper handling of boundaries within the computational domain [107]. For scattering problems, a total-field/scattered-field (TF/SF) source is employed, splitting the domain into two subregions: the total field region includes both the scattered and incident fields and contains the scatterer, while the scattered field region contains only the scattered field [109]. This separation is important for determining quantities such as absorbed and scattered power. Absorbed power can be calculated using volume integrals over the total field region, while scattered power can be computed using surface integrals in the scattered field region [112].

The FDTD method is generally suitable for design cases in which some or all dimensions of the object are comparable to the size of the wavelength of light [107]. Its accuracy and versatility make FDTD the go-to solver for a wide range of photonic designs, including CMOS image sensors, LEDs, OLEDs, microLEDs and liquid crystals, scattering and diffractive optics, metamaterials, metasurfaces, metalenses and plasmonics, integrated photonics, and photonic crystals [112, 113].

FDTD provides several key advantages. Time and frequency domain analysis capabilities offer a dynamic view of electromagnetic fields' evolution over time, with built-in automated Fourier transform of the time-domain solution easily making frequency analysis possible [114]. The broadband capabilities allow calculation of broadband results much faster from a single simulation because it is a time-domain method [107]. The method excels in modeling complex geometries and can handle any arbitrarily shaped structures [111]. FDTD delivers high accuracy and versatility as it is inherently free of any physical approximations [109]. Material versatility allows permittivity values to be assigned individually to each grid point, enabling simulations of linear, nonlinear, and anisotropic materials. Computational efficiency is achieved as FDTD does not involve solving large linear systems, enabling efficient computation, especially with parallelization techniques like MPI and CUDA [115].

However, FDTD also has limitations. Grid constraints mean fields are only computed at discrete grid points, making interpolation at intermediate points computationally intensive [110]. Available computing power limits the maximum device size for accurate simulation. Simulation time depends on several factors from the simulation setup and volume to the hardware specifications of the computing system, with 3D simulation time expected to scale with the relation $\tilde{V}\,(l/dx)^4$, where $\tilde{V}$ is the simulation volume and dx is the grid size [111]. The sheer number of spatial and temporal unknowns in an FDTD simulation grows exponentially with finer meshes and larger simulation volumes, resulting in extremely large amounts of memory and computing power requirements [107]. Memory bandwidth poses challenges through

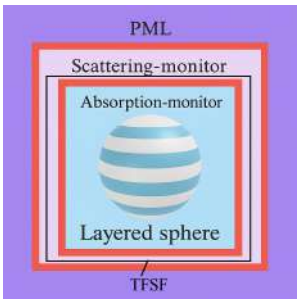

Figure 4.3: FDTD simulation setup showing a multilayer sphere with nested absorption and scattering monitors. The black rectangular region indicates the TFSF (Total Field/Scattered Field) source boundary, surrounded by PML absorbing boundary conditions to eliminate edge reflections.

memory access and heavy data exchange between processors, particularly when dealing with sizable simulations [116]. Special algorithms are required to handle materials with frequency-dependent permittivity for dispersive materials [109]. Absorbing boundary conditions such as Perfectly Matched Layers are required to prevent artificial reflections at the edges of the simulation domain [117].

Modern FDTD implementations leverage multiple advanced approaches to accelerate simulations. The FDTD algorithm has been fine-tuned at a fundamental level over decades to minimize computational overhead while delivering high accuracy [118]. Advanced features and functionalities help streamline the simulation setup, including the mesh, monitors, sources, structures, materials, and analysis groups [114].

High-performance computing solutions utilize highly optimized computational engines able to exploit multicore CPU computing systems and harness the parallel architecture of graphics processing units in high-performance computing clusters [115, 116]. FDTD simulations rely on the parallel processing capabilities of modern CPU and GPU architectures. HPC systems exploit this parallelism to distribute workloads, enabling large-scale simulations of 50-100 billion grid cells to be completed in hours rather than weeks [119]. The necessary computational resources are increasingly accessible through cloud computing platforms, which offer scalable, on-demand access to both CPU and GPU-accelerated simulation software.

In this work, the commercial software ANSYS Lumerical FDTD Solutions is used to perform simulations [120]. The software implements the described methodologies with built-in support for boundary conditions, material definitions, and advanced analysis capabilities, making it suitable for investigating light scattering by nanostructures and complex optical systems [121]. Figure 4.3 illustrates a typical FDTD simulation setup, showing the placement of absorption and scattering monitors around a hyperbolic multilayer sphere. The simulation employs a TF/SF source configuration that divides the computational domain into two distinct regions: the total field region (which includes both scattered and incident fields and contains the scatterer) and the scattered field region (which contains only the scattered field). The TF/SF source is an artificial interface which ensures continuity of the electromagnetic fields across its surface by adding or substracting the analytically- or numerically-calculated source field in such a way, that inside it the total field is present, while outside it only the scattered one remains. The absorption monitor is placed closer to the multilayer sphere within the total field region to record the internal electromagnetic fields and calculate absorbed power using volume integrals. The scattering monitor is positioned further from the object in the scattered field region to capture only the scattered electromagnetic fields, enabling computation of scattered

power through surface integrals. This configuration enables the calculation of both absorbed and scattered power spectra, with PML absorbing boundary conditions ensuring accurate results by eliminating artificial reflections from the simulation edges [117].

4.2.1. Multipole Decomposition in FDTD

Despite the usefulness of FDTD methods, one inherent drawback is that the electromagnetic fields are calculated *as is* without giving clear and simple physical insight into the various interactions between matter and fields. Hence, a postprocessing step is necessary to gain qualitative and quantitative understanding of how a particular structure *works*. One such approach, especially relevant here, is the multipole decomposition which offers insight into the characteristic modes supported by the studied nanoparticles.

The multipole decompositions enables the representation of scattered fields as a sum of multipoles, including electric dipole (ED), magnetic dipole (MD), electric quadrupole (EQ), magnetic quadrupole (MQ), and higher-order multipoles. To perform a multipolar analysis of the scattered fields calculated in FDTD, a multipole decomposition in Cartesian coordinates is implemented using the MENP program (Multipole Expansion for NanoPhotonics) [122]. The MENP program first converts the electric field distributions into current density distributions that result from the light excitation of a nanoresonator. The induced electric current density is obtained using:

$$\mathbf{J}^{\omega}(\mathbf{r}) = i\omega\varepsilon_0(\varepsilon_r - 1)\mathbf{E}^{\omega}(\mathbf{r}), \tag{4.8}$$

where $\mathbf{E}^{\omega}(\mathbf{r})$ is the electric field distribution, ε_0 is the permittivity of free space, and ε_r is the relative permittivity of the material. The multipole derivations, which follow those of Alaee et al. [123] are given in Appendix A, and the final expressions for the multipole moments are presented below.

Exact Multipole Moments

Electric Dipole Moment: The electric dipole moment in Cartesian coordinates is given by:

$$p_{\alpha}^{\omega} = -\frac{1}{i\omega}\int d^3\mathbf{r} J_{\alpha}^{\omega} j_0(kr) + \frac{k^2}{2}\int d^3\mathbf{r}\left[3(\mathbf{r}\cdot\mathbf{J}^{\omega})r_{\alpha} - r^2 J_{\alpha}^{\omega}\right]\frac{j_2(kr)}{(kr)^2}, \tag{4.9}$$

where $\alpha = x, y, z$, $k = \omega/c$ is the wavenumber, and $j_{\ell}(kr)$ are spherical Bessel functions.

Magnetic Dipole Moment: The magnetic dipole moment is expressed as:

$$m_{\alpha}^{\omega} = \frac{3}{2}\int d^3\mathbf{r}(\mathbf{r}\times\mathbf{J}^{\omega})_{\alpha}\frac{j_1(kr)}{kr}, \tag{4.10}$$

where the cross product components in Cartesian coordinates are:

$$(\mathbf{r}\times\mathbf{J}^{\omega})_x = yJ_z^{\omega} - zJ_y^{\omega} \tag{4.11}$$

$$(\mathbf{r}\times\mathbf{J}^{\omega})_y = zJ_x^{\omega} - xJ_z^{\omega} \tag{4.12}$$

$$(\mathbf{r}\times\mathbf{J}^{\omega})_z = xJ_y^{\omega} - yJ_x^{\omega} \tag{4.13}$$

Electric Quadrupole Moment: The electric quadrupole moment has contributions from two different multipolar orders ($\ell = 1$ and $\ell = 3$):

$$Q_{\alpha\beta}^{e} = Q_{\alpha\beta}^{e,\ell=1} + Q_{\alpha\beta}^{e,\ell=3}. \tag{4.14}$$

The combined expression is:

$$Q^e_{\alpha\beta} = -\frac{3}{i\omega}\int d^3\mathbf{r}\left[3(r_\beta J^\omega_\alpha + r_\alpha J^\omega_\beta) - 2(\mathbf{r}\cdot\mathbf{J}^\omega)\delta_{\alpha\beta}\right]\frac{j_1(kr)}{kr} + 2k^2\int d^3\mathbf{r}\left[5r_\alpha r_\beta(\mathbf{r}\cdot\mathbf{J}^\omega) - (r_\alpha J^\omega_\beta + r_\beta J^\omega_\alpha)r^2 - r^2(\mathbf{r}\cdot\mathbf{J}^\omega)\delta_{\alpha\beta}\right]\frac{j_3(kr)}{(kr)^3}, \tag{4.15}$$

where $\delta_{\alpha\beta}$ is the Kronecker delta.

Magnetic Quadrupole Moment: The magnetic quadrupole moment is given by:

$$Q^m_{\alpha\beta} = 15\int d^3\mathbf{r}\left[r_\alpha(\mathbf{r}\times\mathbf{J}^\omega)_\beta + r_\beta(\mathbf{r}\times\mathbf{J}^\omega)_\alpha\right]\frac{j_2(kr)}{(kr)^2}. \tag{4.16}$$

Long-Wavelength Approximations

For nanostructures small compared to the wavelength ($kr \ll 1$), the spherical Bessel functions can be approximated using their small argument expansions, yielding simplified expressions that reveal additional physical insights. These approximations not only reduce computational complexity but also help isolate the contributions of so-called *toroidal moments*, which are higher-order corrections to the electric multipole moments. In particular, the second term in the electric dipole expression corresponds to the toroidal dipole moment, while similar corrections appear in the electric quadrupole moment. These terms are often misinterpreted as a separate family of multipoles but are in fact inherent parts of the exact electric multipole expansion. The long-wavelength approximation thus provides a clearer physical interpretation of how subwavelength structures interact with light, especially in the context of anapole states and non-radiating configurations.

Electric Dipole:

$$p_\alpha \approx -\frac{1}{i\omega}\int d^3\mathbf{r}J^\omega_\alpha + \frac{k^2}{10}\int d^3\mathbf{r}\left[(\mathbf{r}\cdot\mathbf{J}^\omega)r_\alpha - 2r^2J^\omega_\alpha\right]. \tag{4.17}$$

Magnetic Dipole:

$$m^\omega_\alpha \approx \frac{1}{2}\int d^3\mathbf{r}(\mathbf{r}\times\mathbf{J}^\omega)_\alpha \tag{4.18}$$

This is the conventional magnetic dipole moment.

Electric Quadrupole:

$$Q^e_{\alpha\beta} \approx -\frac{1}{i\omega}\int d^3\mathbf{r}\left[3(r_\beta J^\omega_\alpha + r_\alpha J^\omega_\beta) - 2(\mathbf{r}\cdot\mathbf{J}^\omega)\delta_{\alpha\beta}\right] + \frac{k^2}{14}\int d^3\mathbf{r}\left[4r_\alpha r_\beta(\mathbf{r}\cdot\mathbf{J}^\omega) - 5r^2(r_\alpha J^\omega_\beta + r_\beta J^\omega_\alpha) + 2r^2(\mathbf{r}\cdot\mathbf{J}^\omega)\delta_{\alpha\beta}\right]. \tag{4.19}$$

Magnetic Quadrupole:

$$Q^m_{\alpha\beta} \approx \int d^3\mathbf{r}\left[r_\alpha(\mathbf{r}\times\mathbf{J}^\omega)_\beta + r_\beta(\mathbf{r}\times\mathbf{J}^\omega)_\alpha\right]. \tag{4.20}$$

This is the conventional magnetic quadrupole moment.

It is important to note that the expressions for *magnetic* multipole moments (dipole and quadrupole) under the long-wavelength approximation are considered conventional, as they match the forms found in standard electrodynamics textbooks. In contrast, the *electric* multipole expressions are not conventional in the same sense. This is because the conventional electric dipole and quadrupole moments omit higher-order corrections that become significant beyond the long-wavelength limit. The exact expressions derived by Alaee et al. [123] include these corrections through spherical Bessel functions, making them valid for structures of any size relative to the wavelength. Thus, while the magnetic multipole expressions remain unchanged in form under the exact formulation, the electric multipoles require additional terms to account for spatial dispersion effects.

Usage of the MENP Program

The MENP program is a MATLAB-based analytical tool designed to investigate electromagnetic scattering in nanophotonic structures by breaking down total scattering into contributions from multipolar components, such as electric and magnetic dipoles, quadrupoles, and higher-order terms. Its integration with FDTD simulations makes it easy to investigate multipolar interactions. The decomposition process starts with the FDTD simulation of the hyperbolic nanospheroids where the electric field $E(x, y, z, f)$ and refractive index $n(x, y, z, f)$ distributions are recorded using the simulation monitors. These data sets are exported to a MATLAB-compatible `.mat` file (`ENxyzf.mat`) using the `EField2MAT.lsf` (which is an Ansys Lumerical FDTD script) script to facilitate this process, ensuring compatibility with the program's input format. The data file contains four-dimensional matrices representing the electric field components and refractive indices at each spatial and frequency point in the simulation domain.

In MATLAB, the MENP program first converts the electric field distributions into current density distributions as already given in equation 4.8. This conversion is handled by the `E2J.m` function, one of the core utilities in MENP. Once the current density distributions are obtained, MENP calculates the contributions from various multipole components using one of three provided methods: exact multipole expansion (`exactME.m`), an approximated method (`approxME.m`) suitable for long-wavelength approximations, or a formulation including toroidal dipole moments (`toroidalME.m`) for specialized applications such as analyzing anapole states. For this dissertation, the `exactME.m` is used. The computed multipole contributions are expressed as partial scattering cross sections, corresponding to individual multipolar terms like electric dipoles, magnetic dipoles, and electric and magnetic quadrupoles. MENP then sums these partial contributions to determine the total scattering cross-section.

Motivation for Multipole Decomposition in FDTD

The multipole decomposition in FDTD is necessary due to the increased computational complexity of the hyperbolic nanospheroids and the need for detailed field distribution analysis. While FDTD provides full-field solutions, it does not inherently offer physical insight into the multipolar nature of light-matter interactions. Decomposing the scattered fields into multipole moments allows for identifying dominant resonant modes, engineering interference effects, and optimizing structures for specific functionalities such as directional scattering or non-radiating states. The exact expressions implemented in MENP ensure accuracy even for larger or more complex structures where the long-wavelength approximation fails, making it an essential tool for modern nanophotonics research.

Total Scattering Cross Section

The total scattering cross section is calculated as the sum of contributions from all multipole orders:

$$C_{\text{sca}}^{\text{total}} = \frac{k^4}{6\pi\varepsilon_0^2|\mathbf{E}_{\text{inc}}|^2}\left[\sum_{\alpha}\left(|p_\alpha|^2 + \frac{|m_\alpha|^2}{c^2}\right) + \frac{1}{120}\sum_{\alpha\beta}\left(k^2|Q^e_{\alpha\beta}|^2 + \frac{k^2|Q^m_{\alpha\beta}|^2}{c^2}\right) + \cdots\right], \tag{4.21}$$

where $k = \omega/c$ is the wavenumber, ε_0 is the permittivity of free space, $|\mathbf{E}_{\text{inc}}|$ is the amplitude of the incident electric field, c is the speed of light, and $\alpha, \beta = x, y, z$ denote the Cartesian components. The ellipsis indicates contributions from higher-order multipoles that become important for larger structures or higher frequencies.

4.3. T-Matrix Method

The T-matrix method provides a powerful computational framework for solving electromagnetic scattering problems [124, 125]. Its core principle is to characterize how an object scatters an incident wave by establishing a linear relationship between the expansion coefficients of the incident and scattered fields in a basis of vector spherical wave functions (VSWFs). The method is particularly powerful because the resulting matrix, called the T-matrix or transition matrix, depends solely on the physical properties (size, shape, refractive index, orientation) of the scatterer. Once computed for a given particle, it can be used to efficiently calculate scattering for any incident field direction or polarization [125].

4.3.1. General T-Matrix Formulation

The incident ($\mathbf{E}_{\text{inc}}$) and scattered ($\mathbf{E}_{\text{sca}}$) fields are expanded in terms of regular ($\mathbf{M}^1_{mn}, \mathbf{N}^1_{mn}$) and outgoing ($\mathbf{M}^3_{mn}, \mathbf{N}^3_{mn}$) vector spherical wave functions, respectively:

$$\mathbf{E}_{\text{inc}}(\mathbf{r}) = \sum_{n=1}^{\infty}\sum_{m=-n}^{n}\left[a_{mn}\mathbf{M}^1_{mn}(k\mathbf{r}) + b_{mn}\mathbf{N}^1_{mn}(k\mathbf{r})\right], \tag{4.22}$$

$$\mathbf{E}_{\text{sca}}(\mathbf{r}) = \sum_{n=1}^{\infty}\sum_{m=-n}^{n}\left[f_{mn}\mathbf{M}^3_{mn}(k\mathbf{r}) + g_{mn}\mathbf{N}^3_{mn}(k\mathbf{r})\right]. \tag{4.23}$$

Here, k is the wavenumber in the surrounding medium. The coefficients a_{mn} and b_{mn} characterize the known incident wave, while the unknown scattered field coefficients f_{mn} and g_{mn} are the quantities to be determined.

The linear relationship between these sets of coefficients is given by the T-matrix:

$$\mathbf{s} = \mathbf{T}\mathbf{e}, \tag{4.24}$$

where $\mathbf{e} = [a_{mn}, b_{mn}]^T$ and $\mathbf{s} = [f_{mn}, g_{mn}]^T$ are vectors containing the incident and scattered field coefficients, respectively, for all multipole orders n and degrees m. The T-matrix $\mathbf{T}$ is thus the fundamental object that fully describes the scattering properties of the particle.

The T-matrix is computed using the Null-Field Method [124]. This method enforces the boundary conditions on the particle's surface by expanding the internal and scattered fields and projecting the equations onto a complete basis of functions, often the same VSWFs.

For isotropic particles, the resulting matrix elements are given by integrals over the particle surface involving VSWFs (see Eqs. (2.11)–(2.14) in [126]). The T-matrix is then obtained as:

$$\mathbf{T} = -\mathbf{Q}^{11}(k_s, k_i)\left[\mathbf{Q}^{31}(k_s, k_i)\right]^{-1}. \tag{4.25}$$

The matrices $\mathbf{Q}^{pq}$ are defined by surface integrals of cross products between VSWFs of different kinds ($p, q = 1$ for regular, 3 for outgoing) evaluated with the interior (k_i) and exterior (k_s) wavenumbers.

4.3.2. Anisotropic Nanoparticles

For the anisotropic hyperbolic nanospheroids studied in this dissertation, the standard formulation must be modified. The internal field can no longer be described by the regular VSWFs $\mathbf{M}^1_{mn}, \mathbf{N}^1_{mn}$, which are solutions to the Helmholtz equation in an isotropic medium. Instead, one must use vector quasi-spherical wave functions (VQSWFs) $\mathbf{X}^{e,h}_{mn}$ and $\mathbf{Y}^{e,h}_{mn}$ that are solutions to Maxwell's equations in the anisotropic medium [126]. These functions account for the two characteristic waves that propagate in a uniaxial medium: the ordinary wave and the extraordinary wave, which have different dispersion relations.

Let us consider a uniaxial anisotropic particle with its optical axis along z and a permittivity tensor:

$$\boldsymbol{\varepsilon}_i = \begin{pmatrix} \varepsilon_i & 0 & 0 \\ 0 & \varepsilon_i & 0 \\ 0 & 0 & \varepsilon_{iz} \end{pmatrix}. \tag{4.26}$$

The electromagnetic fields inside the particle are expanded as:

$$\mathbf{E}_{\text{int}}(\mathbf{r}) = \sum_{n=1}^{\infty}\sum_{m=-n}^{n}\left[c_{mn}\mathbf{X}^e_{mn}(\mathbf{r}) + d_{mn}\mathbf{Y}^e_{mn}(\mathbf{r})\right], \tag{4.27}$$

$$\mathbf{H}_{\text{int}}(\mathbf{r}) = -j\sqrt{\frac{\varepsilon_i}{\mu_i}}\sum_{n=1}^{\infty}\sum_{m=-n}^{n}\left[c_{mn}\mathbf{X}^h_{mn}(\mathbf{r}) + d_{mn}\mathbf{Y}^h_{mn}(\mathbf{r})\right], \tag{4.28}$$

where the VQSWFs $\mathbf{X}^{e,h}_{mn}$ and $\mathbf{Y}^{e,h}_{mn}$ are defined through integral representations over plane waves (see Appendix B) and reduce to standard VSWFs in the isotropic limit $\varepsilon_{iz} \to \varepsilon_i$.

The dispersion relations for the two waves inside the medium are:

$$k_1^2 = k_0^2\varepsilon_i\mu_i, \quad \text{(ordinary wave)} \tag{4.29}$$

$$k_2^2 = k_0^2\frac{\varepsilon_i\mu_i}{\cos^2\beta + \frac{\varepsilon_i}{\varepsilon_{iz}}\sin^2\beta}. \quad \text{(extraordinary wave)} \tag{4.30}$$

Here, k_0 is the free-space wavenumber, and β is the polar angle of the wave vector inside the medium, illustrating the directional dependence (anisotropy) of the extraordinary wave's propagation constant.

The surface fields are approximated by expanding the tangential fields using VQSWFs:

$$\begin{pmatrix} \mathbf{e}^N_i(\mathbf{r}') \\ \mathbf{h}^N_i(\mathbf{r}') \end{pmatrix} = \sum_{\mu=1}^{N}\left[c^N_\mu\begin{pmatrix} \mathbf{n}(\mathbf{r}')\times\mathbf{X}^e_\mu(\mathbf{r}') \\ -j\sqrt{\frac{\varepsilon_i}{\mu_i}}\mathbf{n}(\mathbf{r}')\times\mathbf{X}^h_\mu(\mathbf{r}') \end{pmatrix} + d^N_\mu\begin{pmatrix} \mathbf{n}(\mathbf{r}')\times\mathbf{Y}^e_\mu(\mathbf{r}') \\ -j\sqrt{\frac{\varepsilon_i}{\mu_i}}\mathbf{n}(\mathbf{r}')\times\mathbf{Y}^h_\mu(\mathbf{r}') \end{pmatrix}\right] \tag{4.31}$$

The index μ is a combined index representing the multipole order and degree, hence we have $\mu = (m, n)$.

Applying the null-field method with discrete sources [127] with this VQSWF basis leads to a modified system matrix. The NFM-DS involves projecting the boundary conditions onto a set of functions (the discrete sources) to enforce the null-field condition inside the particle. This is often more stable than the conventional method using localized VSWFs, especially for particles with extreme geometries or high refractive indices. The elements of the resulting matrix $\mathbf{Q}^{31}_{\text{anis}}$, which is central to the formulation, are given by:

$$(\mathbf{Q}^{31}_{\text{anis}})^{11}_{\nu\mu} = \frac{jk_s^2}{\pi}\int_S \left[(\mathbf{n}\times\mathbf{X}^e_\mu)\cdot\mathbf{N}^3_{\overline{\nu}} + \sqrt{\frac{\varepsilon_i}{\varepsilon_s}}(\mathbf{n}\times\mathbf{X}^h_\mu)\cdot\mathbf{M}^3_{\overline{\nu}}\right] dS, \tag{4.32}$$

$$(\mathbf{Q}^{31}_{\text{anis}})^{12}_{\nu\mu} = \frac{jk_s^2}{\pi}\int_S \left[(\mathbf{n}\times\mathbf{Y}^e_\mu)\cdot\mathbf{N}^3_{\overline{\nu}} + \sqrt{\frac{\varepsilon_i}{\varepsilon_s}}(\mathbf{n}\times\mathbf{Y}^h_\mu)\cdot\mathbf{M}^3_{\overline{\nu}}\right] dS, \tag{4.33}$$

$$(\mathbf{Q}^{31}_{\text{anis}})^{21}_{\nu\mu} = \frac{jk_s^2}{\pi}\int_S \left[(\mathbf{n}\times\mathbf{X}^e_\mu)\cdot\mathbf{M}^3_{\overline{\nu}} + \sqrt{\frac{\varepsilon_i}{\varepsilon_s}}(\mathbf{n}\times\mathbf{X}^h_\mu)\cdot\mathbf{N}^3_{\overline{\nu}}\right] dS, \tag{4.34}$$

$$(\mathbf{Q}^{31}_{\text{anis}})^{22}_{\nu\mu} = \frac{jk_s^2}{\pi}\int_S \left[(\mathbf{n}\times\mathbf{Y}^e_\mu)\cdot\mathbf{M}^3_{\overline{\nu}} + \sqrt{\frac{\varepsilon_i}{\varepsilon_s}}(\mathbf{n}\times\mathbf{Y}^h_\mu)\cdot\mathbf{N}^3_{\overline{\nu}}\right] dS. \tag{4.35}$$

Explanation of indices and notation:

- ν and μ are composite indices representing the pair (m,n) and (m',n') respectively. They index the matrix elements corresponding to different multipole orders and degrees.
- The superscripts pq in $\mathbf{Q}^{pq}$ denote the type of VSWFs used: $p = 1,3$ for the basis functions (regular/outgoing) used to represent the field, and $q = 1,3$ for the functions used to test the boundary condition (via the surface integral). The superscript 31 indicates that the internal field is expanded in regular functions (kind 1) while the null-field condition is tested using outgoing functions (kind 3).
- The subscripts $11, 12, 21, 22$ on the matrix blocks indicate the coupling between different types of modes: 11 for $\mathbf{M}\to\mathbf{M}$ or $\mathbf{X}^e\to\mathbf{N}$, 12 for $\mathbf{N}\to\mathbf{M}$ or $\mathbf{Y}^e\to\mathbf{N}$, 21 for $\mathbf{M}\to\mathbf{N}$ or $\mathbf{X}^e\to\mathbf{M}$, and 22 for $\mathbf{N}\to\mathbf{N}$ or $\mathbf{Y}^e\to\mathbf{M}$.
- $\overline{\nu}$ denotes the index $(-m,n)$, arising from the orthogonality relations of spherical harmonics.
- $\mathbf{n}$ is the outward unit normal vector to the particle surface S.
- k_s and k_i are the wavenumbers in the surrounding medium and the particle, respectively.
- The factor $\sqrt{\varepsilon_i/\varepsilon_s}$ couples the electric and magnetic field contributions and reduces to 1 for non-magnetic media ($\mu_i = \mu_s = 1$) with $\varepsilon_i/\varepsilon_s = m^2$, where m is the refractive index.

The anisotropic T-matrix is then calculated analogously to the isotropic case:

$$\mathbf{T}_{\text{anis}} = -\mathbf{Q}^{11}_{\text{anis}}(k_s,k_i,m_{rz})\left[\mathbf{Q}^{31}_{\text{anis}}(k_s,k_i,m_{rz})\right]^{-1}, \tag{4.36}$$

where $m_{rz} = \sqrt{\varepsilon_{iz}/\varepsilon_s}$ is a relative anisotropy parameter. The matrices $\mathbf{Q}^{11}_{\text{anis}}$ are defined similarly to $\mathbf{Q}^{31}_{\text{anis}}$ but using regular VSWFs $(\mathbf{M}^1,\mathbf{N}^1)$ instead of outgoing ones $(\mathbf{M}^3,\mathbf{N}^3)$, as they are used to project the scattered field representation.

4.3.3. Multipole Decomposition in T-matrix

The SMUTHI package [128] implements the T-matrix method described above along with multipole decomposition in a spherical basis, in contrast to the MENP program which implements multipole decomposition in a Cartesian basis. The scattered electric field can be expanded using spherical multipole terms as:

$$\mathbf{E}(\mathbf{r}) = \sum_{l=1}^{\infty} \sum_{m=-l}^{l} \left(b_{l,m}^{E} \mathbf{M}_{l}^{m}(\mathbf{r}) + b_{l,m}^{M} \mathbf{N}_{l}^{m}(\mathbf{r}) \right), \tag{4.37}$$

where $b_{l,m}^{E}$ and $b_{l,m}^{M}$ represent the electric and magnetic multipole moments, respectively. The functions $\mathbf{M}_{l}^{m}(\mathbf{r})$ and $\mathbf{N}_{l}^{m}(\mathbf{r})$ are VSWFs defined in detail in Appendix C. The expansion coefficients $b_{l,m}^{E}$ and $b_{l,m}^{M}$ encapsulate the physical properties of the scatterer and its interaction with the electromagnetic field.

The induced current density $\mathbf{j}$, which arises due to the interaction of the incident field with the scatterer, is related to the total electric field $\mathbf{E}$ as:

$$\mathbf{j} = \epsilon_0(\epsilon - \epsilon_s)\mathbf{E}. \tag{4.38}$$

To perform a detailed multipole decomposition, the Fourier transform of the induced current density is considered, defined as [123]:

$$\mathcal{F}[\mathbf{j}](\mathbf{p}) = \int \mathbf{j}(\mathbf{r}) e^{i\mathbf{p}\cdot\mathbf{r}} d\mathbf{r}. \tag{4.39}$$

Using this Fourier representation, the induced current can be decomposed into multipole terms as:

$$\mathcal{F}[\mathbf{j}](\mathbf{p}) = \sum_{l,m} \left(b_{l,m}^{E} \mathbf{m}_{l}^{m}(\hat{\mathbf{p}}) + i b_{l,m}^{M} \mathbf{n}_{l}^{m}(\hat{\mathbf{p}}) \right), \tag{4.40}$$

where $\mathbf{m}_{l}^{m}$ and $\mathbf{n}_{l}^{m}$ are vector spherical harmonics defined in the angular Fourier domain. The coefficients of the decomposition are determined by:

$$4\pi^3 q_{lm}^{j} = \int d\mathbf{p} \sum_{l',m'} \mathbf{Q}_{l,m}^{\dagger} Y_{l',m'}(\mathbf{p}) \int d\mathbf{r} \mathbf{j}(\mathbf{r}) Y_{l',m'}^{*} j_l(kr), \tag{4.41}$$

where $j_l(kr)$ is the spherical Bessel function. The induced current density is expressed as a spherical tensor:

$$\mathbf{j}(\mathbf{r}) = \begin{bmatrix} j_{-1} \\ j_0 \\ j_1 \end{bmatrix} = \begin{bmatrix} j_x + ij_y \\ \sqrt{2} j_z \\ -j_x + ij_y \end{bmatrix}. \tag{4.42}$$

The multipole moments of the fields are related to those of the currents via the relations [129]:

$$a_{l,m} = -i^l \sqrt{\frac{(2\pi)^3}{Zk^2}} q_{l,m}^{j}, \quad b_{l,m} = -i^l \sqrt{\frac{(2\pi)^3}{Zk^2}} b_{l,m}^{j}, \tag{4.43}$$

where $Z = \sqrt{\mu/\epsilon}$ is the impedance of the medium embedding the scatterer. The scattered electric field resulting from the multipole moments is expressed as:

$$\mathbf{E}_{\text{scat}}(\hat{\mathbf{n}}) = \frac{k_0^2}{4\pi\epsilon_0} \left([\hat{\mathbf{n}} \times [\mathbf{p} \times \hat{\mathbf{n}}]] + \frac{1}{c} [\mathbf{m} \times \hat{\mathbf{n}}] + \cdots \right). \tag{4.44}$$

The extinction cross-section C_{ext} can be expanded in terms of contributions from individual multipoles as:

$$C_{\text{ext}} = \frac{k_d}{\epsilon_0 \epsilon_d |\mathbf{E}_{0x}|^2} \text{Im} \left\{ E_{0x}^* \left(p_x - i k_d \frac{1}{6} Q_{xz} + \cdots \right) \right\}. \tag{4.45}$$

Similarly, the scattering cross-section C_{scat} accounts for all multipole contributions:

$$C_{\text{scat}} = \frac{k_0^4}{6\pi\epsilon_0^2} |\mathbf{p}|^2 + \cdots. \tag{4.46}$$

4.4. Coupled Harmonic Oscillator Models

The quantum mechanical framework presented in Section 3.1 provides fundamental insight into strong coupling through the Jaynes-Cummings formalism, revealing polariton formation and vacuum Rabi splitting. However, practical analysis of experimental spectra requires computational models that can directly relate these quantum parameters to observable extinction and scattering cross-sections. Coupled harmonic oscillator models [130] bridge this gap, providing a classical interpretation that captures the essential physics while enabling quantitative fitting to measured spectra.

The classical coupled oscillator approach is mathematically equivalent to the quantum treatment when appropriate loss mechanisms are included. The complex eigenfrequencies obtained from the non-Hermitian quantum Hamiltonian correspond exactly to the poles of the classical response functions, demonstrating that both frameworks describe identical underlying physics from complementary perspectives.

4.4.1. Two Peaks Spectra

The extinction and scattering cross-sections for a coupled system consisting of an excitonic system interacting with an optical resonance are derived using a phenomenological coupled oscillator framework. This framework models the interaction between the optical and excitonic systems as coupled damped harmonic oscillators, providing a direct classical analog to the quantum polariton states described in Section 3.1.

The dynamics of the coupled system are governed by the following equations of motion [131]:

$$\ddot{x}_{\text{opt}}(t) + \gamma_{\text{opt}} \dot{x}_{\text{opt}}(t) + \omega_{\text{opt}}^2 x_{\text{opt}}(t) + g \dot{x}_{\text{ex}}(t) = F_{\text{opt}}(t), \tag{4.47}$$

$$\ddot{x}_{\text{ex}}(t) + \gamma_{\text{ex}} \dot{x}_{\text{ex}}(t) + \omega_{\text{ex}}^2 x_{\text{ex}}(t) - g \dot{x}_{\text{opt}}(t) = F_{\text{ex}}(t), \tag{4.48}$$

where:

- x_{opt} and x_{ex} represent the oscillation coordinates for the optical and excitonic systems, respectively
- γ_{opt} and γ_{ex} are the damping constants (linewidths) corresponding to the loss rates γ_{cav} and γ_{QE} in the quantum treatment
- ω_{opt} and ω_{ex} are the resonance frequencies of the optical and excitonic systems
- g is the coupling strength between the systems, identical to the quantum coupling parameter
- $F_{\text{opt}}(t)$ and $F_{\text{ex}}(t)$ are the external driving forces acting on the optical and excitonic oscillators

Assuming the excitonic system is negligibly excited by the external force ($F_{\text{ex}}(t) \approx 0$), the interaction between the two systems is dominated by the optical system. In the steady-state regime, the solutions for the oscillations take the form:

$$x_{\text{opt}}(t) = \text{Re}\left[\frac{(\omega_{\text{ex}}^2 - \omega^2 - i\gamma_{\text{ex}}\omega)F_{\text{opt}}}{(\omega_{\text{opt}}^2 - \omega^2 + i\gamma_{\text{opt}}\omega)(\omega_{\text{ex}}^2 - \omega^2 + i\gamma_{\text{ex}}\omega) - \omega^2 g^2} e^{-i\omega t}\right], \tag{4.49}$$

$$x_{\text{ex}}(t) = \text{Re}\left[\frac{-ig\omega F_{\text{opt}}}{(\omega_{\text{opt}}^2 - \omega^2 + i\gamma_{\text{opt}}\omega)(\omega_{\text{ex}}^2 - \omega^2 + i\gamma_{\text{ex}}\omega) - \omega^2 g^2} e^{-i\omega t}\right]. \tag{4.50}$$

The extinction cross-section, proportional to the power dissipated by the external force on the optical system (note this is $F_{\text{opt}}(t)$, which differs from the negligible excitonic force $F_{\text{ex}}(t) \approx 0$), is given by:

$$C_{\text{ext}}(\omega) \propto \langle F_{\text{opt}}(t)\dot{x}_{\text{opt}}(t)\rangle. \tag{4.51}$$

Substituting the expression for $x_{\text{opt}}(t)$ and simplifying, the extinction cross-section becomes:

$$C_{\text{ext}}(\omega) \propto \omega\, \text{Im}\left[\frac{\omega_{\text{ex}}^2 - \omega^2 - i\gamma_{\text{ex}}\omega}{(\omega_{\text{opt}}^2 - \omega^2 + i\gamma_{\text{opt}}\omega)(\omega_{\text{ex}}^2 - \omega^2 + i\gamma_{\text{ex}}\omega) - \omega^2 g^2}\right]. \tag{4.52}$$

The scattering cross-section, proportional to the square of the induced dipole moment in the optical system, is expressed as:

$$C_{\text{sca}}(\omega) \propto \omega^4 \left|\frac{\omega_{\text{ex}}^2 - \omega^2 - i\gamma_{\text{ex}}\omega}{(\omega_{\text{opt}}^2 - \omega^2 + i\gamma_{\text{opt}}\omega)(\omega_{\text{ex}}^2 - \omega^2 + i\gamma_{\text{ex}}\omega) - \omega^2 g^2}\right|^2. \tag{4.53}$$

These equations describe how the coupling between the excitonic and optical systems leads to hybridized resonances, producing transparency dips and modified spectral features in both extinction and scattering. The parameters provide insight into the physical characteristics of the system: the coupling strength g determines the interaction strength, while the damping constants ($\gamma_{\text{opt}}, \gamma_{\text{ex}}$) dictate the resonance widths. The resonance frequencies ($\omega_{\text{opt}}, \omega_{\text{ex}}$) determine the spectral positions of the optical and excitonic systems.

The quantum mechanical foundation for this phenomenological treatment is provided by the Jaynes-Cummings model detailed in Section 3.1. The Hamiltonian for the coupled QE-cavity system with phenomenological losses yields a non-Hermitian matrix:

$$\hat{H}_{\text{loss}} = \begin{pmatrix} \omega_{\text{cav}} - i\gamma_{\text{cav}}/2 & g \\ g & \omega_0 - i\gamma_{\text{QE}}/2 \end{pmatrix}, \tag{4.54}$$

where γ_{cav} and γ_{QE} represent the amplitude decay rates of the cavity and QE, respectively, corresponding directly to γ_{opt} and γ_{ex} in the classical treatment.

At resonance $\omega_{\text{cav}} = \omega_0 = \omega_o$, the eigenvalues of this quantum system become:

$$E_{\pm} = \omega_o - \frac{1}{2}i\left(\frac{\gamma_{\text{cav}}}{2} + \frac{\gamma_{\text{QE}}}{2}\right) \pm \frac{1}{2}\sqrt{4g^2 - \left(\frac{\gamma_{\text{cav}}}{2} - \frac{\gamma_{\text{QE}}}{2}\right)^2} \tag{4.55}$$

From this equation, the splitting is given by:

$$\Omega_R = E_+ - E_- = \sqrt{4g^2 - \left(\frac{\gamma_{\text{cav}}}{2} - \frac{\gamma_{\text{QE}}}{2}\right)^2} \tag{4.56}$$

For the splitting to be real, $4g^2 - \left(\frac{\gamma_{\text{cav}}}{2} - \frac{\gamma_{\text{QE}}}{2}\right)^2 > 0$, which gives [75]:

$$2g > \frac{|\gamma_{\text{cav}} - \gamma_{\text{QE}}|}{2} \tag{4.57}$$

This condition ensures the coupling rate is larger than the difference of the linewidths . The splitting becomes experimentally detectable when the real part of the energy splitting exceeds the sum of the individual mode linewidths. This condition combines both previous requirements and can be expressed as:

$$\sqrt{4g^2 - \left(\frac{\gamma_{\text{cav}}}{2} - \frac{\gamma_{\text{QE}}}{2}\right)^2} > \frac{\gamma_{\text{cav}}}{2} + \frac{\gamma_{\text{QE}}}{2} \tag{4.58}$$

which gives:

$$4g^2 > \frac{\gamma_{\text{cav}}^2 + \gamma_{\text{QE}}^2}{2} \tag{4.59}$$

This condition is typically stated as: [76, 77]:

$$2g > \frac{\gamma_{\text{cav}} + \gamma_{\text{QE}}}{2} \tag{4.60}$$

This strong coupling condition confirms that the splitting is larger than the average linewidth of the individual, uncoupled resonators. This condition is more stringent than the previous one since it requires the observation of two resolvable peaks in the spectrum, corresponding to Equation 3.34 from Section 3.1. This demonstrates that the classical coupled oscillator model captures the essential physics of quantum strong coupling while providing a direct connection to experimentally observable spectroscopic features.

4.4.2. Three Peaks Spectra

Building upon the two-peak model, some material systems contain multiple excitonic transitions that can simultaneously interact with optical modes, leading to more complex spectral behavior. Alternatively, a single excitonic transition may interact with multiple optical modes. The former situation is particularly relevant for transition metal dichalcogenides (TMDCs), which exhibit both A and B exciton resonances. The increased complexity arises from the additional interactions between the optical mode and the multiple excitonic systems, requiring an extension of the Tavis-Cummings formalism presented in Section 3.1 to multiple exciton species.

The interaction is modeled using coupled equations of motion [132]. The system's dynamic response is described by the amplitude vector (x_{opt}, x_A, x_B), where each component represents the amplitude of the respective oscillator. The time evolution of these amplitudes is governed by the following set of coupled differential equations:

$$\ddot{x}_{opt} + 2\gamma_{opt}\dot{x}_{opt} + \omega_{opt}^2 x_{opt} = F_{opt}(t) + 2g_A\dot{x}_A + 2g_B\dot{x}_B \tag{4.61}$$

$$\ddot{x}_A + 2\gamma_A\dot{x}_A + \omega_A^2 x_A = -2g_A\dot{x}_{opt} \tag{4.62}$$

$$\ddot{x}_B + 2\gamma_B\dot{x}_B + \omega_B^2 x_B = -2g_B\dot{x}_{opt} \tag{4.63}$$

Here, ω_ν and γ_ν $(\nu = opt, A, B)$ represent the resonance frequencies and damping rates (linewidths) of the respective modes. The coupling constants g_A and g_B denote the near-field interactions between the optical mode and the A and B excitons, respectively. The external driving force $F_{opt}(t)$ acts solely on the optical mode, assuming it is the only mode

directly interacting with the incident light. Under harmonic excitation, $F_{opt}(t) = F_{opt}^0 e^{-i\omega t}$, the steady-state solution for the optical amplitude x_{opt} can be obtained:

$$x_{opt} = F_{opt}\big[(\omega_A^2 - \omega^2 - i\gamma_A\omega)(\omega_B^2 - \omega^2 - i\gamma_B\omega)\big] \times \big[(\omega_{opt}^2 - \omega^2 - i\gamma_{opt}\omega)(\omega_A^2 - \omega^2 - i\gamma_A\omega) \times (\omega_B^2 - \omega^2 - i\gamma_B\omega) - 4\omega^2 g_A^2(\omega_B^2 - \omega^2 - i\gamma_B\omega) - 4\omega^2 g_B^2(\omega_A^2 - \omega^2 - i\gamma_A\omega)\big]^{-1} \quad (4.64)$$

The intensity of the scattered light is proportional to the square of the optical amplitude using the Larmor formula:

$$I_{sca} \propto \omega^4 |x_{opt}|^2 \quad (4.65)$$

The eigenenergies of the coupled system are extracted as the eigenvalues of the corresponding 3×3 Jaynes-Cummings-like Hamiltonian:

$$\hat{H} = \hbar \begin{pmatrix} \omega_{opt} - i\frac{\gamma_{opt}}{2} & g_A & g_B \\ g_A & \omega_A - i\frac{\gamma_A}{2} & 0 \\ g_B & 0 & \omega_B - i\frac{\gamma_B}{2} \end{pmatrix}. \quad (4.66)$$

This three-level system represents a natural extension of the two-level Jaynes-Cummings treatment, where the cavity mode now couples simultaneously to two distinct excitonic transitions. The resulting eigenstates are hybrid polariton modes with contributions from all three oscillators, analogous to the dressed states described in Section 3.1 but with increased complexity due to the additional coupling pathways. This formalism effectively captures the interaction between optical and excitonic resonances, allowing for quantitative characterization of coupling strengths and mode hybridization in the complex multi-exciton systems studied in this work. The approach maintains the essential physics revealed by the quantum treatment while providing computational tractability for fitting experimental spectra and extracting material parameters.

Chapter 5

Optical Modes of Uniaxial Hyperbolic Multilayer Nanospheroids

Having introduced the framework for excitonic materials and hyperbolic metamaterials in Chapter 2, and detailed the computational methods in Chapter 4, we now turn to investigating the optical properties of our target nanostructures. This chapter serves as the foundation for all subsequent analyzes by systematically characterizing how shape and material anisotropy influence the optical response of uniaxial hyperbolic multilayer nanospheroids.

Building upon previous detailed study of a uniaxial hyperbolic multilayer nanosphere [133], this investigation extends the analysis to non-spherical geometries, examining how the relationship between particle shape and material anisotropy influences optical mode coupling characteristics. Before exploring strong coupling phenomena with excitonic materials in the later chapters, it is essential to understand the fundamental optical modes that can serve as the optical resonators in these hybrid systems. The goal of this chapter is to demonstrate how various multipoles in uniaxial hyperbolic multilayer nanospheroids combine to produce the observed optical spectra as particle shape transitions from prolate to oblate geometries. This systematic characterization will provide the foundation for understanding which optical modes are most suitable for achieving strong coupling with excitons in subsequent chapters.

The investigation employs multiple numerical techniques, including T-matrix calculations and FDTD simulations, to understand the shape-dependent optical resonances in uniaxial hyperbolic multilayer nanospheroids. All figures and results presented in this chapter are published in Paper 1 [134].

All structures are designed to have volumes equivalent to that of a 50 nm radius sphere, which is a constant reference dimension throughout the dissertation's projects. The choice of a 50 nm radius sphere with equivalent volumes for prolate and oblate geometries represents a carefully considered balance of multiple scientific and practical constraints rather than an arbitrary decision. This dimension places the nanoparticles in the optimal regime for the physics under investigation: they are sufficiently subwavelength (compared to visible/near-IR light wavelengths of 400–2000 nm) to enable rigorous multipole analysis while being large enough to support well-defined electric and magnetic dipole resonances central to this study, in addition to supporting quadrupole resonances. The constant volume constraint across all geometries is essential for isolating shape-dependent effects from size-dependent effects, ensuring that observed differences in coupling strength and mode characteristics arise purely from geometric factors rather than variations in total material content. This size range also represents a practical compromise for the computational methods employed (T-matrix and FDTD simulations), providing sufficient accuracy without prohibitive computational costs while remaining

within current nanofabrication capabilities for potential experimental validation. The 50 nm scale is directly relevant to applications in nanophotonics, plasmonic sensing, and quantum optical devices, making the theoretical insights practically meaningful for device design.

5.1. Methods

This study employs the effective medium theory framework established in Section 4.1 to model a type-II hyperbolic material. The effective permittivities are calculated using the Maxwell-Garnett approach detailed in Section 4.1, with the perpendicular and parallel components given by equations (5.1) and (5.2) respectively:

$$\varepsilon_\perp = f_m\varepsilon_m + (1 - f_m)\varepsilon_d, \tag{5.1}$$

$$\varepsilon_\parallel = \frac{\varepsilon_m\varepsilon_d}{f_m\varepsilon_d + (1 - f_m)\varepsilon_m}, \tag{5.2}$$

where f_m is the metal fill fraction as defined in Section 4.1, ε_m, and ε_d are the permittivities of the metal and dielectric $\varepsilon_d = 1.52$ (to mimic glass), respectively.

Although the outcomes and inferences remain consistent regardless of how permittivity is derived—whether through artificial metal-dielectric structures [135, 136] or natural hyperbolic materials [137, 138]—to demonstrate the spectral characteristics of hyperbolic nanospheroids, the permittivity tensor ϵ is modeled using a silver/silica multilayer, as illustrated schematically in Figure 5.1(a). The optical axis of the hyperbolic material, aligned with the dielectric component $\varepsilon_{zz} \equiv \varepsilon_\parallel$, is oriented parallel to the unique axis of the prolate/oblate nanoparticles. The metallic components $\varepsilon_{xx} = \varepsilon_{yy}$, referred to as $\varepsilon_\perp$, are orthogonal to the optical axis.The tensor elements are expressed using the effective medium equations (5.2) and (5.1), respectively.

Figure 5.1 illustrates the constituent permittivities that form the hyperbolic tensor, along with ε for $f_m = 0.5$. This configuration achieves a low-loss type-II hyperbolic tensor across the near-IR–VIS spectrum, ranging approximately from 0.5–1 to 3 eV. Adjusting the fill factor allows this spectral range to shift continuously [133] toward the red spectrum by deviating from equal proportions of metal and dielectric, as shown in Figures 5.1(c and d).

In this study, the assumption is made that the permittivity of the thin layers remains consistent with their bulk values. This assumption may not hold for nanoscale metal particles, where quantum size effects and surface scattering become important [139]. Consequently, mesoscopic electrodynamics at metal surfaces should be considered as appropriate for a particular case, incorporating quantum-corrected hydrodynamics or detailed surface-response analyses [140]. However, for the initial scope of this study, material-related effects such as thickness-dependent permittivity modifications [141], nonlocality [142], quantum Landau damping[143], and surface roughness [144] are excluded. This decision aligns with the primary objective of examining mode coupling in particles influenced by shape and hyperbolic material anisotropy, rather than going into specific dispersion mechanisms. In essence, the purpose here is to study how a hyperbolic permittivity determines the optical modes of nanoparticles, not whether a particular approximation of the hyperbolic permittivity is always accurate under any conditions.

The assumption of a local, bulk permittivity relies on the fact that supporting FDTD calculations with an explicitly layered medium yield results comparable to those obtained with an effective medium. A nonuniform spatial mesh with a discretization step of 4 Å is employed to capture the fields within 4 nm dielectric and metal layers $f_m = 0.5$, with a 4 nm resolution elsewhere and a graded transition between the meshes. The chosen 4 nm

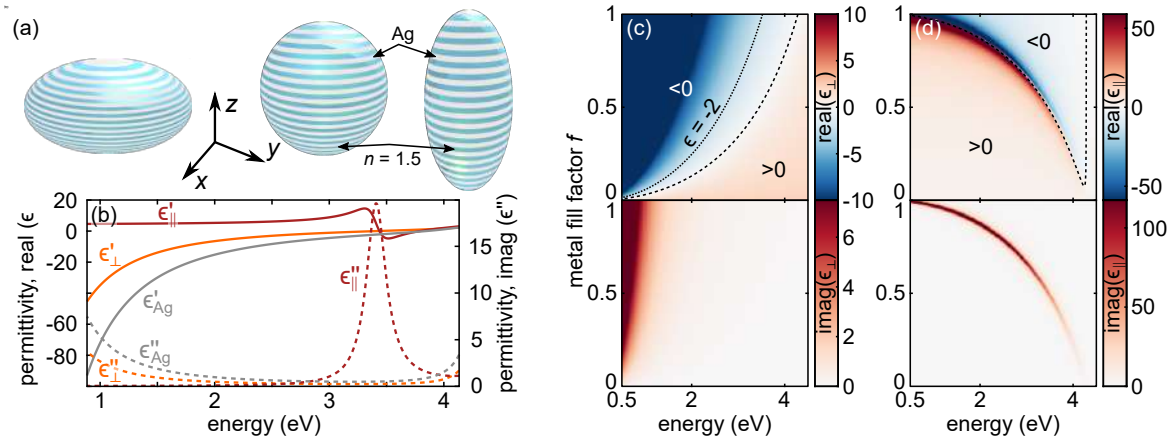

Figure 5.1: Schematic of the studied system and material models. (a) The optical axis of the hyperbolic uniaxial material is aligned with the shorter or longer axis of an oblate or prolate nanospheroid, respectively. (b) Real ε' and imaginary ε'' components of the permittivity of silver (Ag), which is the basis for the effective permittivity of the hyperbolic material, with the dielectric having a refractive index of $n = 1.5$. (c) Effective permittivity as a function of the metal fill factor in an Ag/dielectric multilayer structure.

thickness ensures consistency with T-matrix calculations but does not necessarily account for fabrication considerations. A linearly polarized plane wave is introduced using a total-field/scattered-field approach, spanning frequencies from 0.5 to 4 eV. The simulation volume is truncated using symmetric/asymmetric boundary conditions and perfectly matched layer (PML) absorbing boundaries.

5.1.1. Hyperbolic Nanoparticles T-matrix Calculations

The T-matrix calculations for hyperbolic nanoparticles follow the methodology detailed in Section 4.3 for anisotropic particles. The T-matrix method is an approach to solving scattering problems by expanding the incident (**a**) and scattered (**b**) fields into a chosen basis. Using the VSWF basis set, the relationship between the expansion coefficients is given as:

$$\mathbf{b} = \mathbf{T}\mathbf{a}, \tag{5.3}$$

where **T** is the T-matrix describing a particular scatterer. This matrix is calculated using the null-field method with discrete sources [127, 145], offering computational efficiency for single-particle scattering analysis.

For anisotropic hyperbolic nanoparticles, the standard vector spherical wave functions (VSWFs) are replaced by vector quasi-spherical wave functions (VQSWFs) as described in Section 4.3. The anisotropic T-matrix formulation accounts for the uniaxial permittivity tensor:

$$\boldsymbol{\varepsilon}_i = \begin{pmatrix} \varepsilon_\perp & 0 & 0 \\ 0 & \varepsilon_\perp & 0 \\ 0 & 0 & \varepsilon_\parallel \end{pmatrix}, \tag{5.4}$$

where $\varepsilon_\perp$ and $\varepsilon_\parallel$ are calculated using equations (5.1) and (5.2).

To solve the boundary problem, ensuring the continuity of incident and surface fields on a particle, the T-matrix for each multipole pair is determined by solving a 2×2 block system

following the anisotropic T-matrix approach from Section 4.3:

$$T_{m_1 l_1, m_2 l_2} = -Q^{(1)}_{m_1 l_1, m_2 l_2} \left[Q^{(3)}_{m_1 l_1, m_2 l_2} \right]^{-1}. \tag{5.5}$$

Here, $Q^{(1)}$ and $Q^{(3)}$ are integrals involving the regular and radiating vector spherical wave functions (VSWFs), respectively, with modifications for anisotropic media as detailed in the T-matrix formulation. The $(1,1)$ element of the $Q^{(3)}$ matrix is expressed as:

$$Q^{3,(1,1)}_{m_1 l_1, m_2 l_2} = \frac{ik^2}{\pi} \int \left[m_r \left(\hat{n} \times X^h_{m_1, l_1} \right) \cdot M^3_{-m_2, l_2} + \left(\hat{n} \times X^e_{m_1, l_1} \right) \cdot N^3_{-m_2, l_2} \right] dS. \tag{5.6}$$

In this expression we have that M and N are the VSWFs, m_r is the relative refractive index, k is the wavenumber, $\hat{n}$ is the unit vector normal to the particle surface, X^e and X^h (and then by symmetry Y^e and Y^h) are quasi-spherical wave functions (QSWFs) corresponding to the internal modes of the hyperbolic nanoparticle. The remaining $Q^{(3)}$ matrix elements are obtained by swapping functions or modes. For example: exchanging M for N (or vice versa) modifies the first index, while swapping the second index involves interchanging the X and Y internal modes. Expressions for $Q^{(1)}$ are similar but replace M^3 and N^3 with M^1 and N^1. The QSWFs are parameterized by angles (α, β), determined by the wave vector in spherical coordinates. In essence, (α, β) represent the directional parameters of wave propagation in the anisotropic medium, with β being the polar angle and α being the azimuthal angle in spherical coordinates.

Among the main advantages of the T-matrix is the fact that it takes an especially simple form for nanoparticles with a symmetry axis. In such a case, the surface equation does not depend on the azimuthal angle ϕ, which promotes analytical integration of the Q-integrals over the azimuthal coordinate. Thus, the numerical calculation of Q-integrals reduces to a one-dimensional integral over θ. This simplification has been widely used for isotropic particles. This approach can also be exploited for uniaxial nanoparticles if the particle symmetry axis and the optical axis are parallel. The simplified version of the Q-integrals is used to evaluate the optical properties of hyperbolic nanoparticles at a computational cost similar to that for isotropic nanoparticles. These computations are performed using the T-matrix code as implemented in the SMUTHI package [128], with a custom extension that enables calculating the optical properties of uniaxial nanoparticles with an axis of symmetry.

In this particular case the optical cross-sections are calculated using the standard T-matrix expressions detailed in Section 4.3, with the extinction cross-section given by:

$$C_{\text{ext}} = -\frac{\pi}{k_s^2} \sum_{\nu=1}^{\infty} \text{Re}\{ f^N_\nu a^*_\nu + g^N_\nu b^*_\nu \} \tag{5.7}$$

and the scattering cross-section:

$$C_{\text{scat}} = \frac{\pi}{k_s^2} \sum_{\nu=1}^{\infty} \left(|f^N_\nu|^2 + |g^N_\nu|^2 \right), \tag{5.8}$$

where the scattered field coefficients f^N_ν and g^N_ν are obtained from the anisotropic T-matrix multiplication with the incident field coefficients.

5.2. Results and Discussion

The spectral characteristics of two extreme cases, a prolate and an oblate nanospheroids, are evaluated within the chosen parameter range. These nanospheroids have aspect ratios (AR)

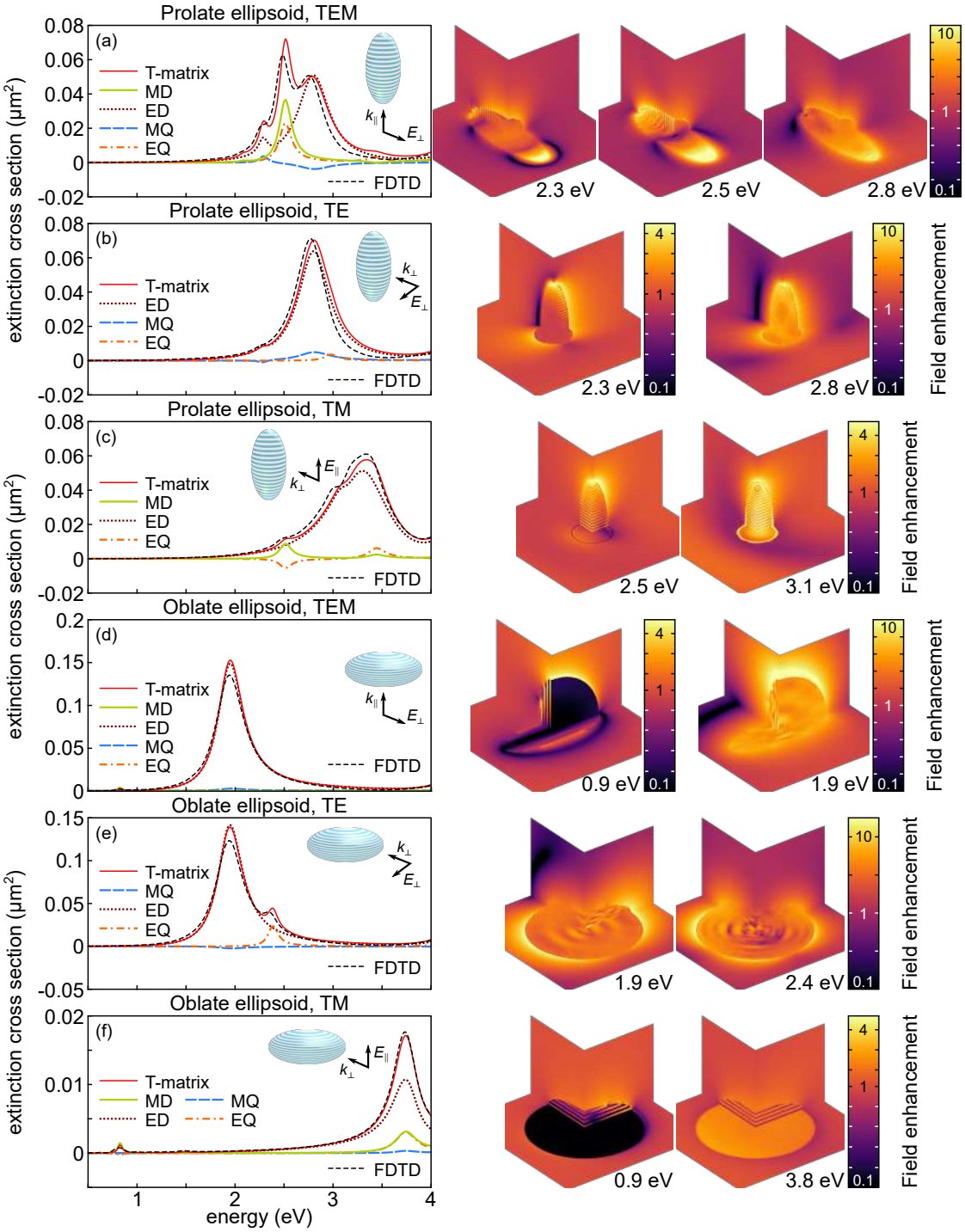

Figure 5.2: Extinction spectra of (a-c) prolate and (d-f) oblate hyperbolic nanospheroids under three unique illumination conditions. The individual multipoles are obtained using the T-matrix approach with an effective permittivity. The total T-matrix extinction is a sum of the individual multipoles and quantitatively agrees with the total extinction calculated using FDTD for an explicit Ag/dielectric multilayer. The right column illustrates the corresponding electric fields calculated using FDTD at selected resonances. The nanoparticle volumes are equivalent to that of a sphere with a 50 nm radius. The semiaxes for the prolate nanoparticle are 34.7 nm and 104 nm, while those for the oblate nanoparticle are 72 nm and 24 nm.

of $A = 1/3$ and $A = 3$, respectively, and maintain identical volumes equivalent to that of a sphere with a radius of 50 nm. The aspect ratio is defined as $A = r_x/r_z$, where $r_x = r_y$ are the lengths of the identical semiaxes, and r_z is the length of the third semiaxis parallel to the optical axis of the hyperbolic material. Both hyperbolic nanospheroids (HNSs) are illuminated by a plane wave with three unique (independent) polarization states to probe all possible optical modes due to symmetry, as illustrated in the insets of Figure 5.2. The permittivity values used, shown in Figure 5.1(b), correspond to a metal fill factor $f_m = 0.5$, with a hyperbolic dispersion region below approximately 3.5 eV.

Figure 5.2 presents the optical extinction cross-section spectra calculated using the T-matrix method, including contributions from the first four multipoles: magnetic dipole (MD), electric dipole (ED), magnetic quadrupole (MQ), and electric quadrupole (EQ). These results are compared to a reference FDTD calculation, where the metal-dielectric multilayer is explicitly defined. The extinction spectra of hyperbolic nanostructures reveal a rich set of electric and magnetic resonances [133, 138, 146].

For prolate HNSs under TEM illumination Figure 5.2(a), the spectrum in the hyperbolic range ($\lesssim 3.5\,\mathrm{eV}$) exhibits three prominent peaks. At 2.8 eV, a peak dominated by an out-of-phase ED-MQ contribution is observed. At 2.5 eV, a strongly mixed and constructively coupled MD-EQ resonance appears, followed by an in-phase ED-MQ resonance at lower energies. These spectral features are qualitatively similar to those of a hyperbolic nanosphere of the same volume [133], with notable differences due to the distinct shape, including a low-energy ED peak.

When the prolate HNS is illuminated normally to the optical axis, the three peaks are selectively excited. Under TE illumination Figure 5.2(b), only two ED-weak MQ resonances are observed, with the MQ phase contribution reversed. The MD-EQ mode, however, is not excited. In contrast, under TM illumination Figure 5.2(c), the MD-EQ mode dominates the spectrum. In addition, a stronger mode, which is almost purely ED, emerges, corresponding to the large permittivity of the ϵ_{zz} component and exhibiting lossy dielectric-like behavior. The extinction spectra for oblate HNSs are shown in Figures 5.2 (d-f). Due to the obvious altered shape, resonances shift towards lower energies (red-shifted). The dominant resonance for TEM and TE illumination (Figures 5.2 (d and e) is an ED mode weakly coupled with the MQ.

This mode is absent under TM illumination (Figure 5.2(f)), where a weak mode appears beyond the hyperbolic range at approximately 3.8 eV. Under TE illumination, a higher-energy EQ resonance is observed. In addition, the coupled MD-EQ mode appears at around 0.9 eV, although it exhibits low amplitude due to the oblate geometry. The multipolar contributions to extinction reveal both positive and negative contributions, depending on the order and illumination conditions. For instance, the MD-EQ resonance at 2.5 eV and the ED-MQ peak at 2.8 eV exhibit such behavior. Negative contributions, as previously reported in silicon nanodisks [147] and hyperbolic nanospheroids [133], arise from the symmetry of the particle and the illumination conditions [133, 148].

These aspects are further discussed in Section 5.2.2. In addition to extinction cross-sections, Figure 5.2 illustrates the induced field enhancements at resonances. These fields are highly localized, with amplitudes reaching 10–20-fold enhancement, characteristic of plasmonic resonances in metallic nanoparticles. Remarkably, such field amplification is also observed for magnetic modes. Prolate particles exhibit the strongest enhancement, exceeding a 10-fold increase, demonstrating very efficient light interaction with the magnetic mode—a phenomenon not typically observed in dielectric particles.

5.2.1. Dependence of Small Nanoparticles

The quasistatic analysis reveals a distinct shape-dependence of both the ED and the coupled MD–EQ modes in small hyperbolic nanospheroids, as illustrated in Figure 5.3.

For the ED resonance, which behaves as a typical localized surface plasmon resonance (LSPR), the T-matrix component in the quasistatic approximation takes the form:

$$T^{1,1}(\mathcal{A}) = -f^{1,1}(\mathcal{A}) i x^3 \frac{\epsilon_{ii} - 1}{\epsilon_{ii} + g^{1,1}(\mathcal{A})}, \tag{5.9}$$

where $x \equiv kr_{eq}$ is the size parameter, ϵ_{ii} is the appropriate diagonal component of the permittivity tensor, and the functions $f^{1,1}(\mathcal{A})$ and $g^{1,1}(\mathcal{A})$ determine the resonance's amplitude and spectral shift respectively.

This expression is consistent with the Rayleigh polarizability for spheroidal particles, where the principal dipolar polarizabilities α_i are given by:

$$\alpha_i \propto \frac{\epsilon - 1}{3L_i(\epsilon - 1) + 3} \quad \text{with} \quad L_z = \frac{1 - e^2}{e^2}\left[\frac{\operatorname{atanh}(e)}{e} - 1\right], \quad L_x = L_y = \frac{1 - L_z}{2}, \tag{5.10}$$

where $i = x, y, z$ and the eccentricity is $e^2 = (r_z^2 - r_x^2)/r_z^2$. The shape factor $g^{1,1}(\mathcal{A})$ corresponds to the term $(1-L_x)/L_x$ from the denominator of the Rayleigh polarizability α_i, and exhibits an approximately linear dependence on the aspect ratio within the studied range ($\mathcal{A} \in [0.33, 3]$).

In contrast, the MD–EQ mode exhibits a significantly stronger sensitivity to shape changes. Its resonant condition in the quasistatic approximation is given by:

$$T^{0,0}(\mathcal{A}) = f^{0,0}(\mathcal{A}) i x^5 \frac{\Psi_1(\epsilon_\perp, \epsilon_\parallel)}{(\epsilon_\perp + g^{0,0}(\mathcal{A})\epsilon_\parallel)\Psi_3(\epsilon_\perp, \epsilon_\parallel)}, \tag{5.11}$$

where Ψ_1 and Ψ_3 are third-order polynomial functions with no roots in the relevant energy range. The magnetic resonance occurs when the denominator condition is satisfied:

$$\epsilon_\perp + g^{0,0}(\mathcal{A})\epsilon_\parallel = 0. \tag{5.12}$$

The proportionality factor $g^{0,0}(\mathcal{A})$ depends quadratically on the aspect ratio, resulting in a much larger redshift of the MD–EQ resonance (approximately 1.8 eV) compared to that of the ED mode (approximately 0.7 eV) when the particle shape evolves from prolate to oblate. For specific aspect ratios, this condition becomes:

$$\text{for } \mathcal{A} = 1/3: \quad \epsilon_\perp + 0.35\epsilon_\parallel = 0, \tag{5.13}$$

$$\text{for } \mathcal{A} = 3: \quad \epsilon_\perp + 10.65\epsilon_\parallel = 0. \tag{5.14}$$

The distinct scaling behaviors highlight the unique material- and shape-dependent nature of the magnetic mode in hyperbolic nanoparticles, which is absent in both purely dielectric and metallic nanospheroids.

Figure 5.3(a) compares the resonant energies of the ED and MD modes obtained from full T-matrix calculations and the quasistatic approximation, showing excellent agreement for sub-20 nm nanoparticles. The black line indicates the absorption maximum for an isotropic spheroid with permittivity $\epsilon_\perp$, further emphasizing the unique dispersion of hyperbolic particles. Figure 5.3(b) illustrates the different scaling trends: the ED follows a nearly linear shape factor (comparing $g^{1,1}(\mathcal{A})$ with $(1 - L_x)/L_x$ from the Rayleigh polarizability), while the MD follows a quadratic trend, underscoring the enhanced tunability of the magnetic resonance via particle geometry.

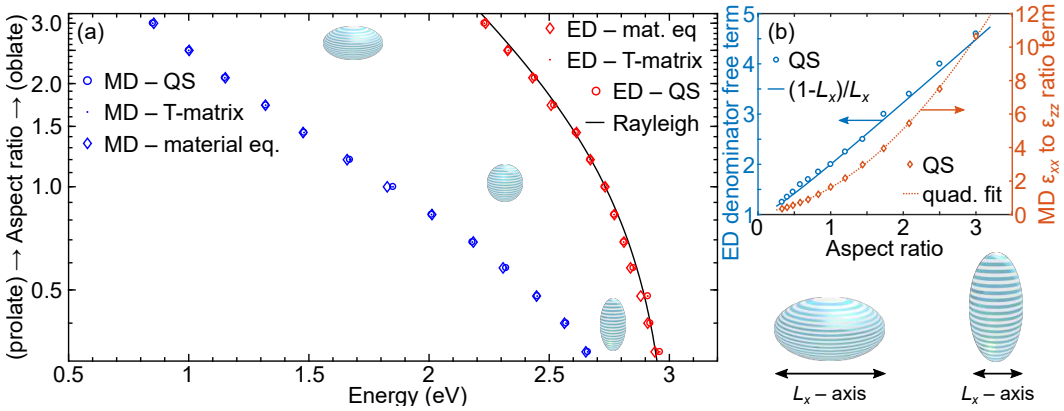

Figure 5.3: (a) Shape-dependence of resonant energy of the magnetic and electric dipole of hyperbolic nanoellipsoids. The ED resonance is the typical LSPR, the magnetic one is the coupled MD-EQ resonance. The exact T-matrix results calculated for a sub-20 nm nanoellipsoid match the quasistatic results. The black line marks the absorption maximum of the Rayleigh polarizability for a spheroidal particle with an isotropic permittivity equal to $\epsilon_\perp$. (b) ED and MD resonance scaling vs. particle aspect ratio. Left y-axis: comparison of the QS-estimated scaling parameter (circles) of the ED resonance and the Rayleigh polarizability free term in the denominator (solid line) assuming vacuum as the surrounding material. Right y-axis: calculated ratio of the QS-derived $-\epsilon_{xx}/\epsilon_{zz}$ (diamonds) MD resonance condition and fitted quadratic (dotted line) trend line.

5.2.2. Aspect Ratio Influence on Mode Coupling and Evolution

Figure 5.4 illustrates the total absorption and scattering cross-sections of the studied hyperbolic nanospheroids, calculated using the T-matrix methodology from Section 4.3, along with a decomposition into electric and magnetic dipole (ED and MD) and quadrupole (EQ and MQ) contributions under TEM, TE, and TM illumination. The numerical values below the descriptions in each plot indicate the maximum value of the respective quantity, showing the relative strength of the spectra. From these plots, two primarily distinct groups of modes—MD–EQ and ED–MQ—are evident, both of which redshift as the aspect ratio (AR) increases. The presence of these two coupling groups arises from particle symmetry, which can be analyzed using group theory approaches [149]. These hyperbolic nanospheroids belong to the $D_{\infty h}$ point group [148], where electric and magnetic multipole coupling occurs only between odd and even orders, while coupling of the same type skips every other order [133].

Under TEM and TM illumination, the MD–EQ modes are efficiently coupled, as evidenced by their identical dependence on the aspect ratio, and form a single coupled peak in the optical spectra. The sign of the coupling for these modes differs between TEM and TM illumination due to excitation and coupling symmetries [133]. However, it is the same for each individual illumination direction in the whole considered aspect ratio range from 0.33 to 3. In contrast, under TE illumination, the particle behaves as a plasmonic system dominated by strong EQ and ED contributions, driven by the unique illumination conditions.

The ED–MQ modes exhibit qualitatively similar behavior under TEM and TM illumination. A prominent ED resonance redshifts from approximately 3 eV to 2 eV with increasing aspect ratio, accompanied by a coupled MQ resonance. Notably, the sign of the MQ contribution switches as the AR transitions through 1 (a spherical geometry) for a given polarization. This behavior is typical of nonspherical particles with isotropic permittivity, as symmetry breaking restricts the system to the $D_{\infty h}$ point group. However, this coupling mechanism is

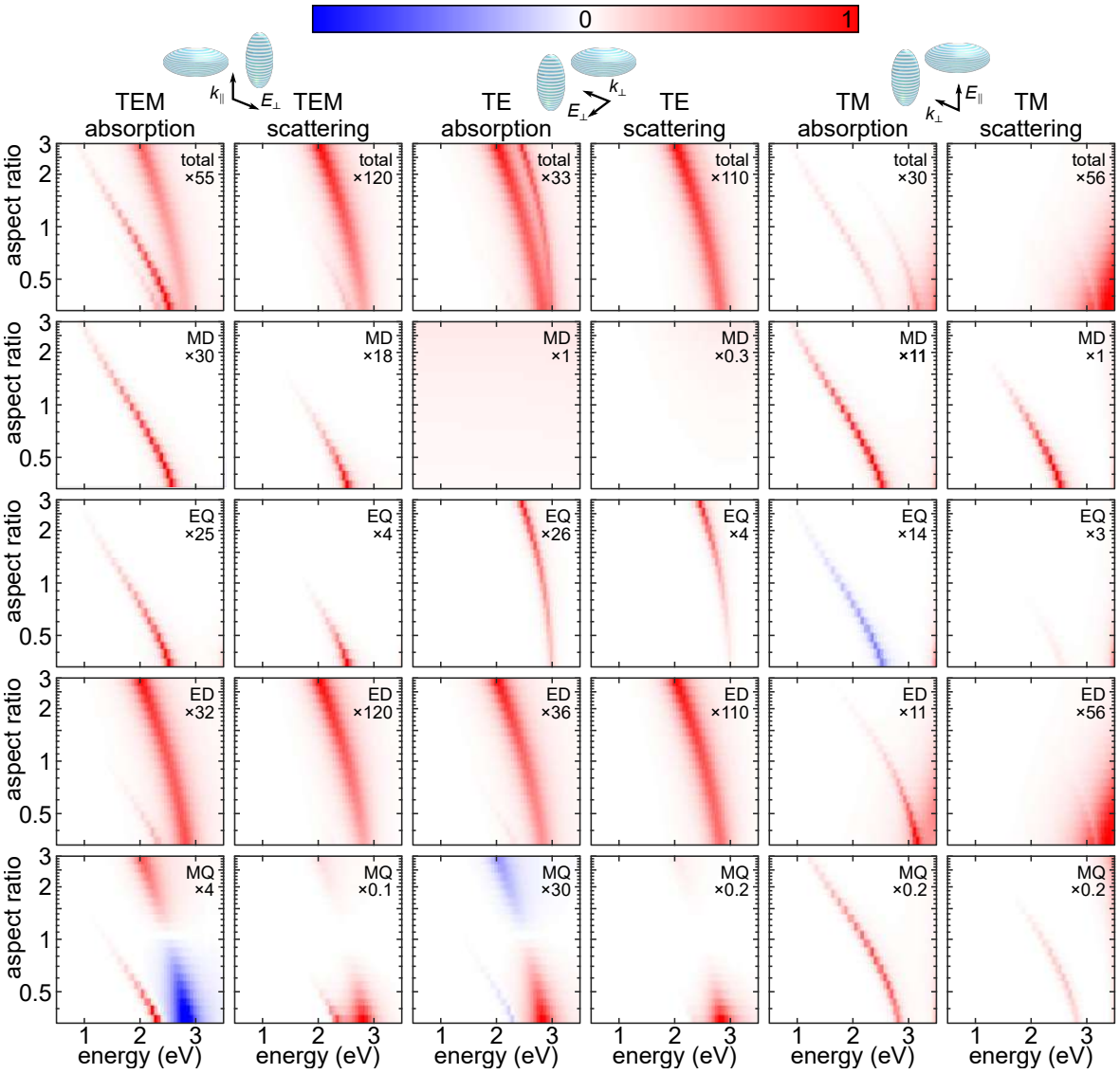

Figure 5.4: Absorption and scattering cross-sections of hyperbolic nanospheroids with a volume equivalent to that of a 50 nm sphere under different plane wave illumination conditions. The left two columns correspond to TEM illumination, where the wave vector **k** is parallel to the optical axis. The middle two columns depict TE illumination, where both **k** and the electric field are perpendicular to the optical axis. The right two columns represent TM illumination, where **k** and the magnetic field are perpendicular to the optical axis.

distinct from that of the material-dependent MD–EQ mode, where the coupling sign remains constant regardless of AR.

In addition to the primary ED–MQ mode, a narrower coupled ED–MQ mode appears at lower energies. For TEM illumination, the MQ contribution to absorption is positive, while under TE illumination it is negative. In both cases, the sign of the MQ contribution remains consistent across the AR range. This behavior suggests that this additional mode is also material-dependent and unique to hyperbolic nanoparticles.

The negative contributions to absorption observed for certain multipoles (e.g., TM for EQ; TEM and TE for MQ) align with the extinction results in Figure 5.2. Mathematically, this phenomenon arises from the solutions of the T-matrix and the projection of the incident plane wave onto the multipoles [126, 133]. Physically, these negative contributions result from internal coupling between the particle's multipoles and the phase of the incident light. While the total extinction or absorption of an isolated system is always positive (assuming no gain), individual modes can exhibit negative contributions due to energy transfer between coupled multipoles.

For instance, in systems with strong out-of-phase coupling, certain modes can effectively return more energy to the electromagnetic field than they receive directly from the source [150]. Although such modes may exhibit negative extinction, the total absorption for an individual particle remains positive. Importantly, scattering contributions for all multipolar components are positive [126]. However, extinction does not follow this rule, as it is determined by both the incident and scattered fields, allowing for the possibility of negative contributions. Fundamentally, this phenomenon shows the role of out-of-phase coupling between interacting multipoles in enabling negative contributions, a characteristic feature of hyperbolic nanoparticles.

5.2.3. Influence of Metal Fill Factor on the Optical Multipoles of Hyperbolic Nanospheroids

The anisotropic optical behavior of hyperbolic nanospheroids (HNSs) can be influenced by several parameters, including the type of metal (characterized by its plasma frequency), the dielectric layer permittivity, and the volume ratio of the constituent materials. Among these, varying the metal fill factor offers a practical method to adjust the plasma frequency of the metallic component in the hyperbolic dispersion, concurrently altering $\varepsilon_{\perp}$. This adjustment can be achieved during fabrication by selecting appropriate layer thicknesses or post-fabrication via electrostatic gating [151] or mechanical strain [152] applied to anisotropic or hyperbolic van der Waals (vdW) materials.

Figure 5.5 illustrates the spectral changes in the first four multipoles (absolute extinction values) calculated using the T-matrix approach detailed in Section 4.3, as the metal fill factor is varied across nanospheroids with aspect ratios ranging from 0.33 (prolate, gray) to 3 (oblate, red). The AR values with values between 0.33 and 3 are marked by the intermediate colors outlined in the inset. A notable red shift of all modes is observed with increasing aspect ratio, consistent with trends seen in Figure 5.4. Within the hyperbolic dispersion region, two distinct behaviors emerge concerning the metal fill factor. Plasmonic modes, similar to those in isotropic metal nanoparticles, display a continuous blue shift with increasing metal fill factor (f_m). This shift is evident in the TEM polarization for the ED and the coupled MQ, and the TE polarization for the ED and EQ. These shifts are attributed to an increase of the effective plasma frequency with higher amount of metal in the multilayer/effective medium (f_m values).

Conversely, the coupled MD and EQ modes exhibit a crescent-like dependence. These modes undergo pronounced red shifts as the nanospheroids transition from prolate to oblate

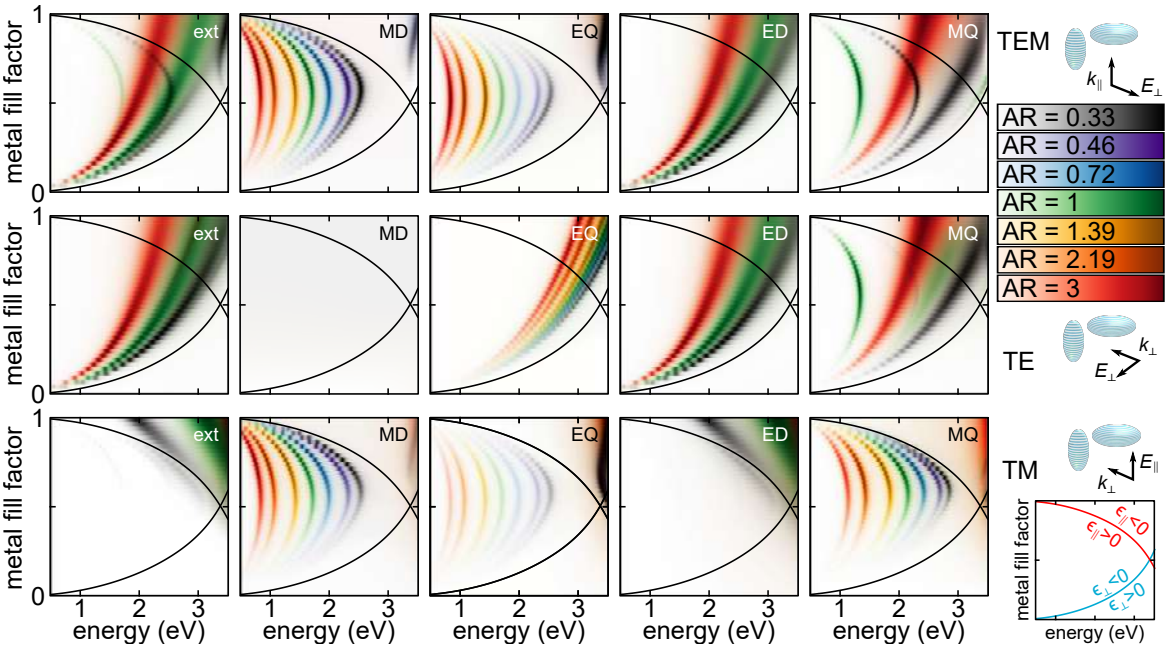

Figure 5.5: The extinction cross section and its multipole components versus metal fill factor for various aspect ratios (ARs, shown in different colors). For TEM and TE modes, the absolute values of total extinction, ED, and MQ are shown at three specific ARs (0.33, 1, and 3). For TM mode, the MD, EQ, and MQ are plotted across all ARs. All calculations use a particle with volume equivalent to a 50 nm radius sphere. Black lines mark where the perpendicular ($\varepsilon_\perp$) and parallel ($\varepsilon_\parallel$) components of the dielectric permittivity reach zero, as shown in the inset.

shapes. Adjusting f_m allows for tuning of these modes, with the most pronounced blue shift occurring around $f_m \approx 0.5$. For nanospheroids with larger aspect ratios, this maximum blue shift converges near $f_m = 0.5$, though the mode amplitudes are more pronounced for $f_m > 0.5$. A similar crescent-shaped pattern is observed for hyperbolic MQ modes under both TEM and TM polarizations, showing the distinct behaviors of plasmonic and hyperbolic modes in HNSs.

The qualitative explanation for these crescent-shaped behaviors lies in the differential influence of the metal fill factor on $\varepsilon_\parallel$ and $\varepsilon_\perp$. For low f_m values, the in-plane metallic permittivity changes more rapidly than the out-of-plane dielectric permittivity, leading to a blue shift in the MD resonance. When f_m exceeds 0.5, $\varepsilon_\perp$ grows more rapidly than $\varepsilon_\parallel$, inducing a red shift. This relationship suggests that enhancing the plasma frequency of $\varepsilon_\parallel$ independently of $\varepsilon_\perp$ could enable further blue shifts in the MD resonance for fixed out-of-plane permittivity. Consequently, HNSs provide a versatile platform for fine-tuning the absolute and relative positions of ED and MD modes, allowing independent red or blue shifts through material and shape modifications.

Chapter 6

Self-Hybridized Strong Coupling of Optical Modes to Exciton in Uniaxial Hyperbolic Multilayer Nanospheroids

Results from Chapter 5 demonstrate that the oblate shape exhibits less favorable optical mode characteristics compared to the prolate and spherical shapes. The oblate geometry shows weaker magnetic dipole modes and reduced field localization—properties important for achieving strong coupling in the MD regime. In contrast, the prolate and spherical geometries support stronger MD resonances with higher field enhancements, as demonstrated in Section 5.2.2, enabling more effective interaction with excitons in the MD regime. Thus, the prolate and spherical shapes are more suitable choices for strong coupling studies involving excitons in hyperbolic nanoparticles. Consequently, this chapter focuses on spherical (aspect ratio of 1) and prolate spheroidal (aspect ratio of 1/3) geometries to achieve self-hybridized strong coupling, with excitons integrated into their material matrix as a function of their optical properties. The sphere has a radius of 50 nm, and the prolate spheroid has a volume equivalent to that of the sphere. The results presented in this chapter are based on the published Paper 2.

Following the approach described in Chapter 5, we explicitly assume bulk permittivity for the few-nanometer layers, even though mesoscopic electrodynamics at metal surfaces may need to be considered [140]. However, this work focuses on exploring mode-exciton coupling, not on how a specific dispersion is obtained. Therefore, while modifications to the permittivity of thin layers based on their thickness [141], nonlocality [142], quantum Landau damping [143], or surface roughnes [144] are relevant under certain conditions, we omit their effects throughout this work, including the study in this chapter, without losing generality.

6.1. Methods

Building upon the hyperbolic multilayer framework established in Chapter 4, we now incorporate excitonic materials to enable self-hybridized strong coupling. Our study employs artificial nanospheroids – namely nanospheres and prolate nanoellipsoids – composed of a silver-silica multilayer with integrated excitons, as depicted in Figures 6.1a and 6.2a, respectively. This approach allows us to explore how excitons embedded directly within the hyperbolic material matrix can achieve strong coupling with the optical modes identified in the previous chapter.

The effective permittivity tensor components are given by the Maxwell-Garnett equations established in Section 4.1 and applied in Chapter 5, where the metallic components $\epsilon_\perp$ are

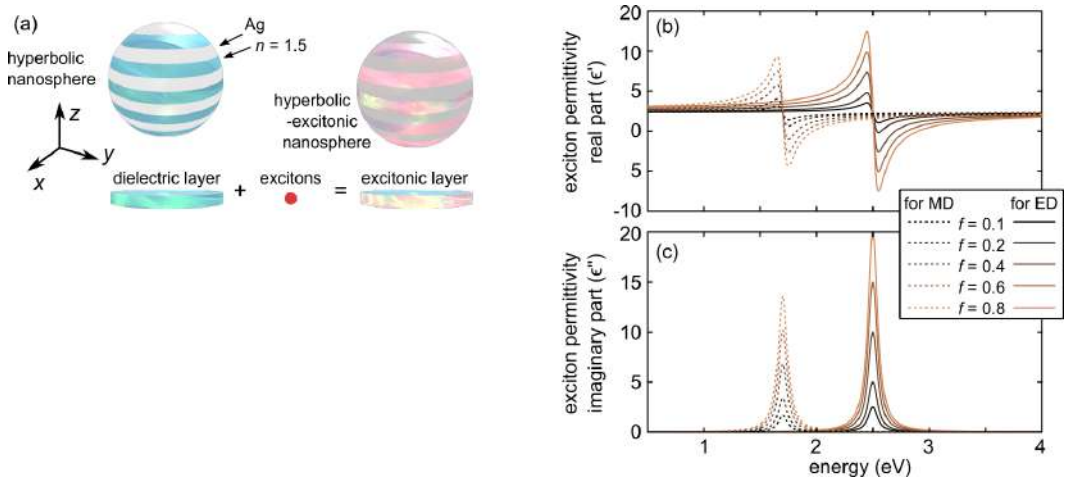

Figure 6.1: System scheme and material models. (a) Hyperbolic Ag/silica nanosphere without (left) and with (right) excitonic inclusions in the dielectric layers. (b) The real and (c) imaginary parts of excitonic inclusions into the dielectric silica layer in hyperbolic nanospheres. The excitons at 1.7 eV match the MD and at 2.5 eV the ED of the hyperbolic nanosphere.

perpendicular to the optical axis (z) and the dielectric component $\epsilon_{\parallel}$ is parallel to the optical axis given by equations (5.1) and (5.2), respectively.

For consistency with Chapter 5, we assume an equal mix ($f_m = 0.5$) of silver and silica ($\epsilon_d = 2.25$), yielding a relatively low-loss hyperbolic nanospheroids with resonances in the near-infrared to visible range, while the filling factor can be adjusted for continuous tuning within a broad energy range as demonstrated in the fill factor analysis from Section 5.2.3.

6.1.1. Excitonic Material Integration

Self-hybridization is enabled through the incorporation of excitonic resonances directly into the dielectric component of the multilayer. The excitonic contribution can originate from various sources, including excitonic [15], interband [153] or molecular transitions [154], vibrational lines [155] or an effective response of nanoscale resonant inclusions in a host medium [156]. The effect of any of these on the permittivity is described by incorporating a Lorentz oscillator into the host material, following the approach established for describing excitonic materials in Section 2.7.2:

$$\epsilon_{\mathrm{ex}}(\omega) = \frac{f\omega_p^2}{\omega_{\mathrm{ex}}^2 - \omega^2 - i\gamma_{\mathrm{ex}}\omega}, \tag{6.1}$$

where ω is the angular frequency, f denotes the oscillator strength, ω_{ex} is the exciton position, $\omega_p \equiv \omega_{\mathrm{ex}}$ is the plasma frequency (assumed equal to the exciton position), and $\gamma_{\mathrm{ex}} = 0.1$ eV is the exciton linewidth. A value of $f = 0$ means there is no excitonic behaviour.

To ensure optimum coupling conditions and best visibility of the two polaritons, we match the exciton positions to the spectral positions of the optical ED and MD modes identified in Chapter 5. These are located at 2.5 eV and 1.7 eV for nanosphere and at 2.8 eV and 2.5 eV for nanoprolate, respectively. Exemplary Lorentzian permittivities for various oscillator strengths, which are used herein, are shown in Figures 6.1b,c and 6.2b,c. It is assumed that the excitons are incorporated in the dielectric layers, hence, the Lorentzian excitonic contribution is added to the background dielectric permittivity as:

$$\epsilon_d \to \epsilon_d + \epsilon_{\mathrm{ex}}(\omega) \equiv \tilde{\epsilon}_d. \tag{6.2}$$

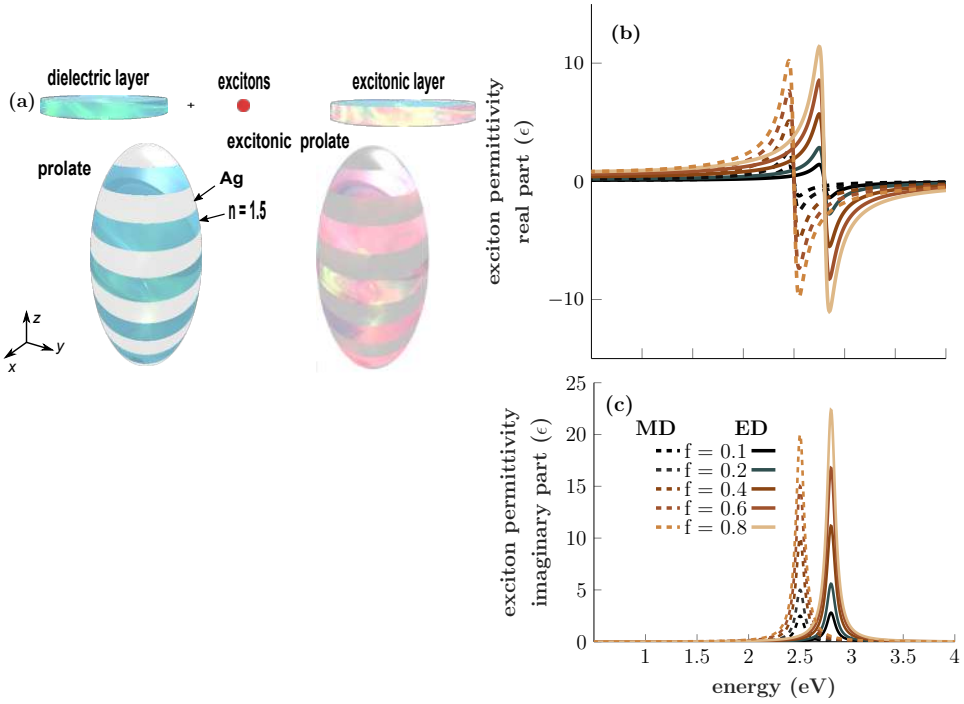

Figure 6.2: System scheme and material models. (a) Hyperbolic Ag/silica nanoprolate without (left) and with (right) excitonic inclusions in the dielectric layers. (b) The real and (c) imaginary parts of excitonic inclusions into the dielectric silica layer in hyperbolic nanoprolates. The excitons at 2.5 eV match the MD and at 2.8 eV the ED of the hyperbolic nanoprolate.

Consequently, in the effective medium approximation that both in- and out-of-plane tensor components of $\boldsymbol{\epsilon}$ acquire an excitonic component.

6.1.2. T-matrix Calculations for Excitonic Systems

The exciton-containing permittivity tensor $\boldsymbol{\epsilon}$ serves as input for the T-matrix method to solve the scattering problem. Following the approach outlined in Section 4.3 for anisotropic particles, we utilize the exact multipole decomposition where the T-matrix relates the expansion coefficients as $\vec{b} = \mathbf{T}\vec{a}$, with the T-matrix evaluated using the null-field method with discrete sources [127, 145].

The anisotropic T-matrix formulation accounts for the uniaxial permittivity tensor with excitonic contributions, which can be expressed as:

$$\boldsymbol{\varepsilon}_i = \begin{pmatrix} \varepsilon_\perp + (1-f_m)\epsilon_{\mathrm{ex}}(\omega) & 0 & 0 \\ 0 & \varepsilon_\perp + (1-f_m)\epsilon_{\mathrm{ex}}(\omega) & 0 \\ 0 & 0 & \tilde{\varepsilon}_\parallel^{\varepsilon_{\mathrm{ex}}} \end{pmatrix}, \tag{6.3}$$

with

$$\tilde{\varepsilon}_\parallel^{\varepsilon_{\mathrm{ex}}} = \frac{\varepsilon_m(\varepsilon_d + \varepsilon_{\mathrm{ex}})}{(1-f_m)(\varepsilon_d + \varepsilon_{\mathrm{ex}}) + f_m\varepsilon_m}. \tag{6.4}$$

We utilize the $D_{\infty h}$ point group symmetry of the hyperbolic nanospheres, as established in Chapter 5, to simplify the T-matrix calculation, reducing the surface integrals to one-dimensional integrals over the polar angle θ. The calculations are performed using the

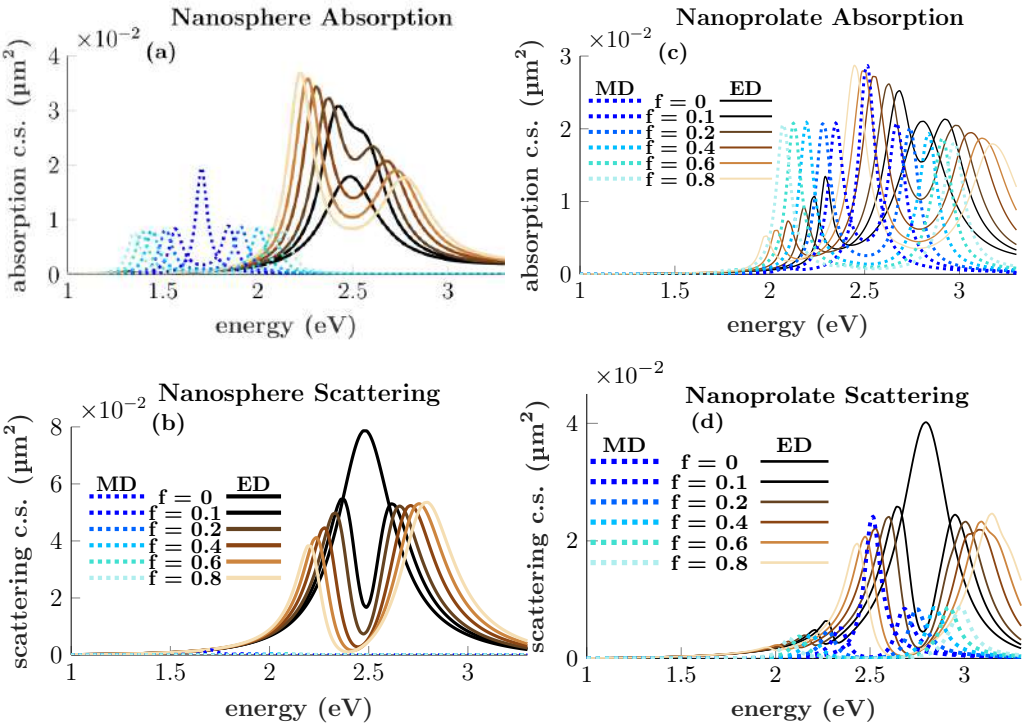

Figure 6.3: Absorption and scattering cross sections of hyperbolic nanospheroids with excitonic inclusions with a variable oscillator strength f. The spectra are decomposed into ED, and MD multipoles for the nanosphere and nanoprolate. (a,b) The exciton energy is 1.7 eV and 2.5 eV that match the MD and ED mode of the nanosphere respectively. (c,d) The exciton energy is 2.5 eV and 2.8 eV that match the MD and ED mode of the nanoprolate respectively.

SMUTHI package [128] with custom extensions for uniaxial nanoparticles, following the computational approach detailed in Section 4.3.

6.2. Results and Discussion

6.2.1. Strong Coupling Characterization

Due to the anisotropic nature of our hyperbolic nanospheroids, as characterized in Chapter 5, we focus on the TEM illumination case where the wave vector is parallel to the anisotropy axis, exciting both ED and MD modes with the linear polarization orientation being unimportant. Under this configuration, both modes can potentially couple to the integrated excitons.

To demonstrate the evolution of coupling between optical modes and excitons, we first examine how the absorption and scattering spectra change with increasing oscillator strength. In Figure 6.3, we present optical cross-sections decomposed into individual multipole orders for varying oscillator strengths, utilizing the multipole decomposition methodology from Section 4.3.3. These spectra clearly reveal the fundamental differences between the MD and ED modes that will prove crucial for understanding their coupling behavior. The MD mode is much narrower than the ED mode, with linewidths of ca. 68 meV and 350 meV for the MD and ED modes, respectively, in the nanosphere, and 105 meV and 319 meV for the MD and ED modes, respectively, in the nanoprolate. The MD is predominantly absorptive with scattering an order of magnitude smaller for the nanosphere [133, 146]. For the prolate nanospheroid

the MD scattering is still smaller than absorption, but the difference is only by a factor of 2–4 despite their relatively large sizes.

For the nanosphere (Figure 6.3a,b), the MD-exciton system at 1.7 eV demonstrates highly efficient coupling, with well-separated polaritons appearing in the absorption spectrum at the smallest plotted oscillator strength ($f = 0.1$). In contrast, the ED case requires $f > 0.2$ before spectral splitting occurs, though the scattering spectrum consistently shows a dip at the exciton linewidth, indicating electromagnetically induced transparency [66]. The MD mode coupled to an exciton exhibits rapid Rabi splitting increase with f, forming two narrow polaritons. For large $f > 0.5$, a third peak emerges at 1.7 eV, reminiscent of findings in prior studies for metal core-exciton shell systems [66], though here it is identified as an ED mode appearing due to increased refractive index.

For the nanoprolate, the uncoupled MD mode ($f = 0$) exhibits a double-peak structure in absorption (a very small peak at ∼2.1 eV which becomes smaller as the oscillator strength increases, and a resonance peak at 2.5 eV) and a single peak in scattering. The MD-exciton system at 2.5 eV shows well-separated polaritons appearing in the absorption and scattering spectra with a characteristic dip at 2.5 eV (Figure 6.3c,d) at the smallest plotted oscillator strength ($f = 0.1$). In the ED case, the uncoupled mode ($f = 0$) has two peaks in both the absorption and scattering spectra (a smaller peak at ∼2.3 eV, which decreases as the oscillator strength increases, and a resonance peak at 2.8 eV). The ED-exciton system at 2.8 eV exhibits well-separated polaritons in both the absorption and scattering spectra with a dip at 2.8 eV (Figure 6.3c,d) at the smallest plotted oscillator strength ($f = 0.1$).

6.2.2. Coupling Strength Analysis

To quantify the interaction regime and determine the onset of strong coupling, we employ the coupled harmonic oscillator model for the extinction spectrum from equation 4.52 recast as:

$$C_{\text{ext}}(\omega) \propto \omega \,\text{Im}\left[\frac{\omega_{\text{ex}}^2 - \omega^2 - i\gamma_{\text{ex}}\omega}{(\omega_{\text{MD/ED}}^2 - \omega^2 + i\gamma_{\text{MD/ED}}\omega)(\omega_{\text{ex}}^2 - \omega^2 + i\gamma_{\text{ex}}\omega) - \omega^2 g^2}\right] \tag{6.5}$$

to fit the extinction cross-section spectra separately for ED and MD interactions. The fits assume fixed optical mode energies and linewidths at their uncoupled values, following the two-peak spectra model from Section 4.4.1. For the nanoprolate, a Lorentz-Drude term as given in Section 2.3 is added to the coupled harmonic oscillator model to account for the smaller peak at 2.3 eV observed for the ED. The fixed linewidths for the nanosphere are those of the exciton (100 meV), MD mode ($\lesssim$ 90 meV), and ED mode (350 meV). For the nanoprolate the linewidths are equal as follows: exciton 100 meV, MD mode 112 meV, and ED mode 325 meV.

Figure 6.4 demonstrates the excellent quality of fits for selected oscillator strengths and plots the fitted coupling strengths as functions of $\sqrt{f}$. This relationship is linear as expected from the theoretical framework established in Chapter 3, where the collective coupling strength for N emitters follows $g_N = \sqrt{N} g_1$ (equation 3.27), and since the oscillator strength f scales linearly with the number of molecules, the coupling strength follows $g \propto \sqrt{f}$. Notably, the MD coupling strength is approximately 50% larger than the ED coupling strength, highlighting the better coupling efficiency of magnetic dipole modes. Despite the larger linewidth of the MD in the nanoprolate compared to the nanosphere, the coupling efficiency of the nanoprolate is higher, demonstrating that geometry plays a crucial role beyond simply optimizing linewidths.

Before a quantitative discussion of the coupling strengths, we briefly recall the strong

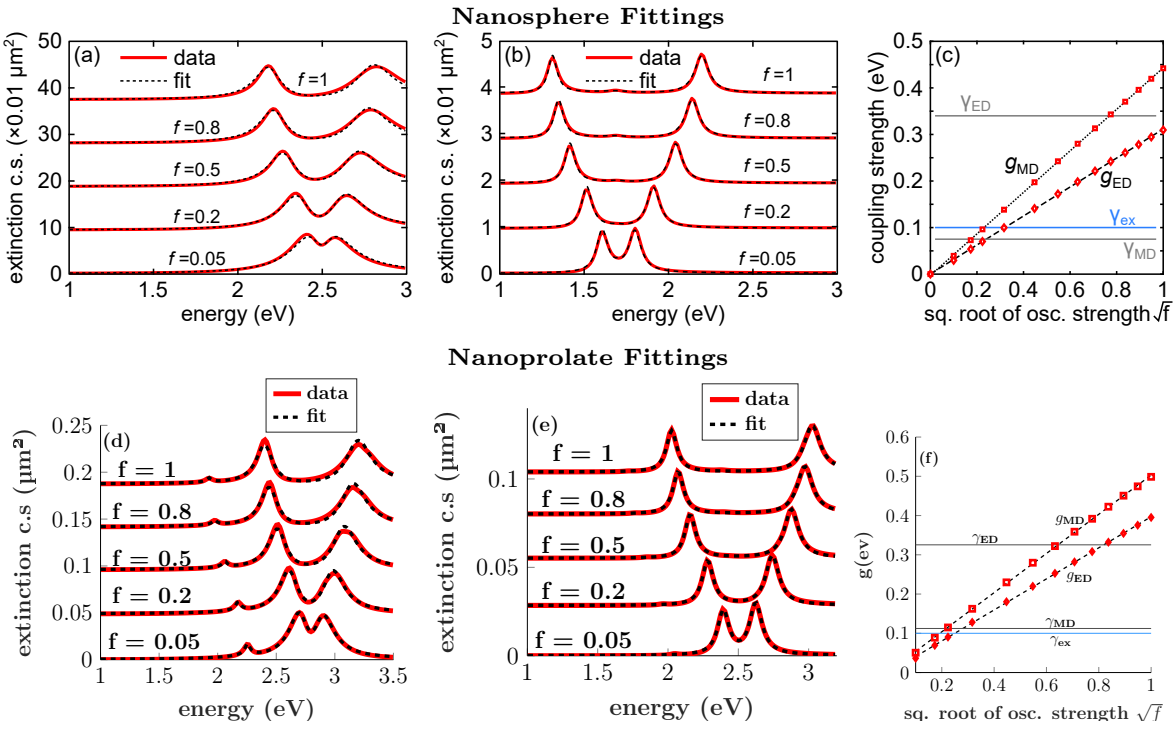

Figure 6.4: Calculated extinction cross sections and coupled harmonic oscillator model fits (black dashed) for (a, b) nanosphere and (d, e) nanoprolate geometries (red lines). Panels (a, d) show ED-exciton coupling while (b, e) show MD-exciton coupling (spectra offset for clarity). (c, f) Fitted coupling strengths for ED (g_{ED}, diamonds) and MD (g_{MD}, squares) modes exhibit linear dependence on $\sqrt{f}$. Gray lines indicate ED (γ_{ED}) and MD (γ_{MD}) mode linewidths.

coupling condition established in Section 4.4, which require that:

$$g > \frac{\gamma_{\mathrm{MD/ED}} + \gamma_{\mathrm{ex}}}{2} \tag{6.6}$$

or, equivalently, that the Rabi splitting satisfies:

$$\Omega_R > |\gamma_{\mathrm{ex}} + \gamma_{\mathrm{ED/MD}}|/2, \tag{6.7}$$

where g is the coupling strength, $\gamma_{\mathrm{MD/ED}}$ are the optical mode linewidths, and γ_{ex} is the exciton linewidth.

For the nanosphere, due to the narrow linewidths of both the exciton (100 meV) and, more importantly, the MD mode ($\lesssim$ 90 meV), the strong coupling regime is reached at remarkably small oscillator strengths, $f_{\mathrm{MD}}^{\mathrm{sc}} \approx 0.04$. The MD-exciton interaction is so efficient that the system enters the ultra-strong coupling regime for $f_{\mathrm{MD}}^{\mathrm{usc}} \approx 0.15$, where $g \geq 0.17$ begins to exceed 10% of the resonance energy. Conversely, for the ED-exciton system, the coupling is less efficient, and the greater width of the ED mode (350 meV) means that strong coupling can only be achieved at significantly larger oscillator strengths, i.e., $f_{\mathrm{ED}}^{\mathrm{sc}} \geq 0.36$. Similarly, ultra-strong coupling is only reached for $f_{\mathrm{ED}}^{\mathrm{usc}} \geq 0.64$.

For the nanoprolate, the narrow linewidths of both the exciton (100 meV) and the MD mode (112 meV) allow the strong coupling regime to be reached at even smaller oscillator strengths, $f_{\mathrm{MD}}^{\mathrm{sc}} \approx 0.03$. The MD-exciton interaction is highly efficient, enabling the system to

enter the ultra-strong coupling regime for $f_{\mathrm{MD}}^{\mathrm{usc}} \approx 0.22$, where $g \geq 0.25$ begins to exceed 10% of the resonance energy. For the ED-exciton system, the coupling remains less efficient, and the greater width of the ED mode (325 meV) means strong coupling requires larger oscillator strengths, $f_{\mathrm{ED}}^{\mathrm{sc}} \geq 0.28$. Similarly, ultra-strong coupling is only achieved for $f_{\mathrm{ED}}^{\mathrm{usc}} \geq 0.50$.

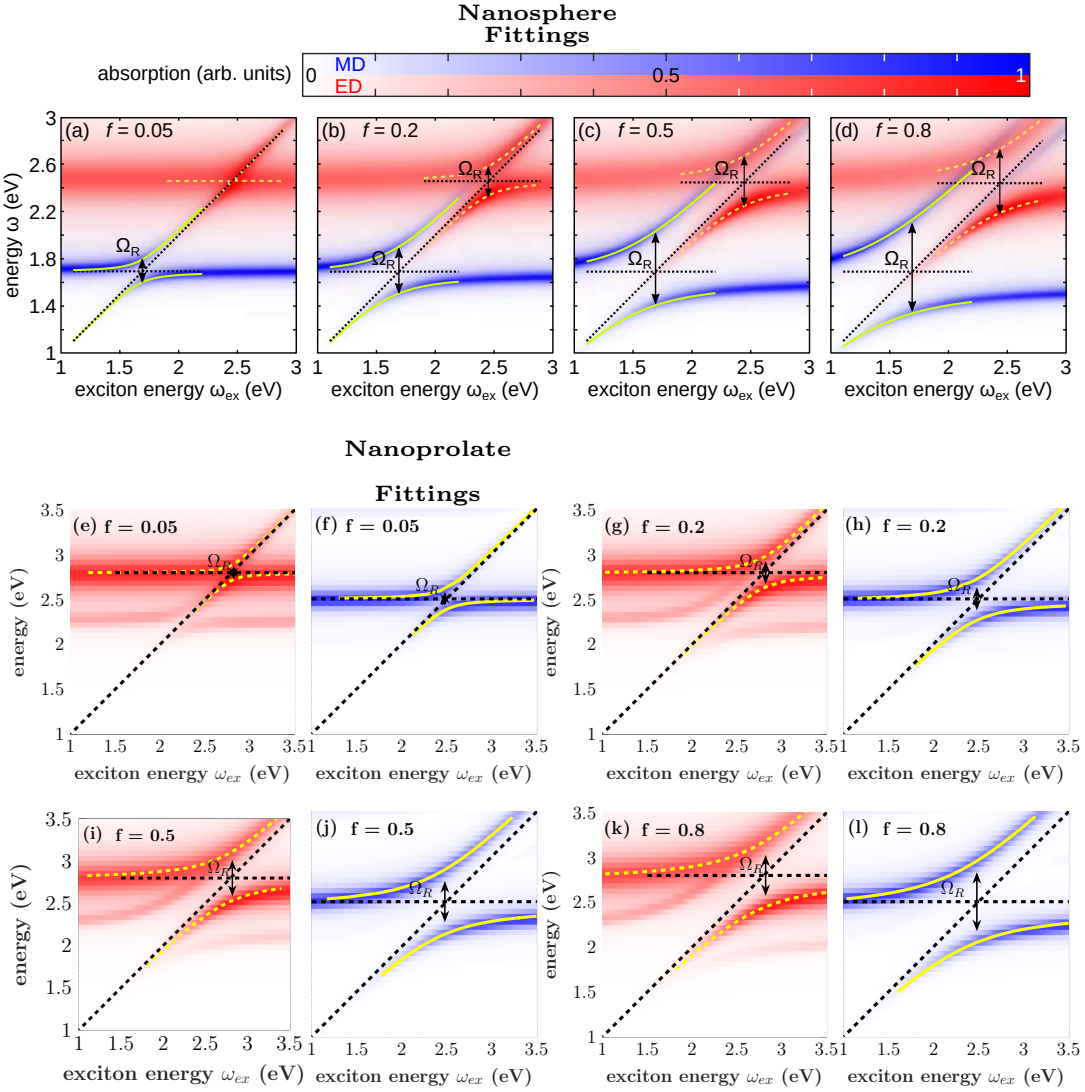

Figure 6.5: The anticrossing dependence on the mode type (ED—red; MD—blue) is shown as a function of the oscillator strength f, with values of (a) 0.05, (b) 0.2, (c) 0.5, and (d) 0.8 for the nanosphere, and (e, f) 0.05, (g, h) 0.2, (i, j) 0.5, and (k, l) 0.8 for the nanoprolate. The colormaps of the spectra are normalized to their respective maximum values in each plot, independently for the ED and MD modes. The black dotted lines indicate the exciton position, and the positions of the ED and MD modes. The curved lines represent the UP (upper polariton) and LP (lower polariton) branches.

6.2.3. Anticrossing Behavior

To further characterize the strong coupling regime and validate our coupling strength analysis, we examine the anticrossing behavior as the exciton energy is systematically tuned across the optical resonances. Figure 6.5 illustrates this anticrossing behavior for ED and MD interactions as functions of exciton energy ω_{ex}, providing direct evidence of the avoided crossing characteristic of strong coupling.

The absorption spectra (blue for MD, red for ED) are fitted using a non-Hermitian Hamiltonian approach given in Section 4.4.1:

$$\begin{bmatrix} \omega_{\mathrm{ED}} - i\gamma_{\mathrm{ED}} & g_{\mathrm{ED}} & 0 & 0 \\ g_{\mathrm{ED}} & \omega_{\mathrm{ex}} - i\gamma_{\mathrm{ex}} & 0 & 0 \\ 0 & 0 & \omega_{\mathrm{MD}} - i\gamma_{\mathrm{MD}} & g_{\mathrm{MD}} \\ 0 & 0 & g_{\mathrm{MD}} & \omega_{\mathrm{ex}} - i\gamma_{\mathrm{ex}} \end{bmatrix}, \tag{6.8}$$

where ω_x, γ_x, and g_x represent the resonance frequency, linewidth, and coupling strength of mode $x = \mathrm{MD}, \mathrm{ED}$. This formulation is analogous to the nonhermitian Hamiltonian from equation (4.54) but extended to include both ED and MD modes simultaneously.

The fitting results shown in Figure 6.5 use black dotted lines to mark the exciton and optical modes, while the polaritons are denoted by colored lines. The lower polariton (LP) and upper polariton (UP) fits agree excellently with the calculated values, demonstrating progressively increasing Rabi splitting with f. A pronounced polaritonic gap appears at large f, particularly for the MD-exciton coupling, starting around $f = 0.5$. This observation aligns with the onset of the ultra-strong coupling regime.

For the nanoprolate, the ED exhibits two distinct anticrossing behaviors (lower and upper anticrossing behaviors), which result from the exciton coupling to both the smaller peak at 2.3 eV and the main resonance peak at 2.8 eV, as the exciton position is varied from 1 to 3.5 eV. The coupling with the smaller peak represents weak coupling, while our focus is on the upper anticrossing behavior, dominated by the ED resonance at 2.8 eV, which strongly couples to the exciton.

6.3. Practical Implementation: Multilayer Nanodisks

While hyperbolic nanospheres demonstrate strong coupling capabilities, practical fabrication considerations motivate the study of multilayer nanodisks [157]. Current fabrication tools enable facile creation of multilayered nanodisks, making them a robust alternative for achieving self-hybridized strong coupling. We now examine how the coupling phenomena observed in idealized spheroidal geometries translate to more readily fabricated multilayer nanodisk structures, which represent a crucial step toward real-world device applications.

We investigate hyperbolic nanodisks with radius $r = 40$ nm and aspect ratio $h/2r = 1$, where h is the height, initially focusing on spectral differences between spherical and disk geometries by varying edge rounding from 0 (perfect disk) to 40 nm (sphere). This systematic variation allows us to understand how geometric modifications affect the coupling strength and mode characteristics. To that end, in this particular case, the nanoparticles are modeled with explicit metal/dielectric layers, what requires use of numerical calculations using the FDTD approach. The hyperbolic material consists of alternating layers of approximately 5 nm of silver and silica, with both ends covered by silver. The permittivities are taken from the input values ϵ_m and ϵ_d used to construct the hyperbolic dispersion in the T-matrix approach.

Simulation parameters include a non-uniform spatial mesh ranging from 4 nm to 1 nm over the nanoparticle, a TFSF plane wave source incident along the z-axis, symmetric and

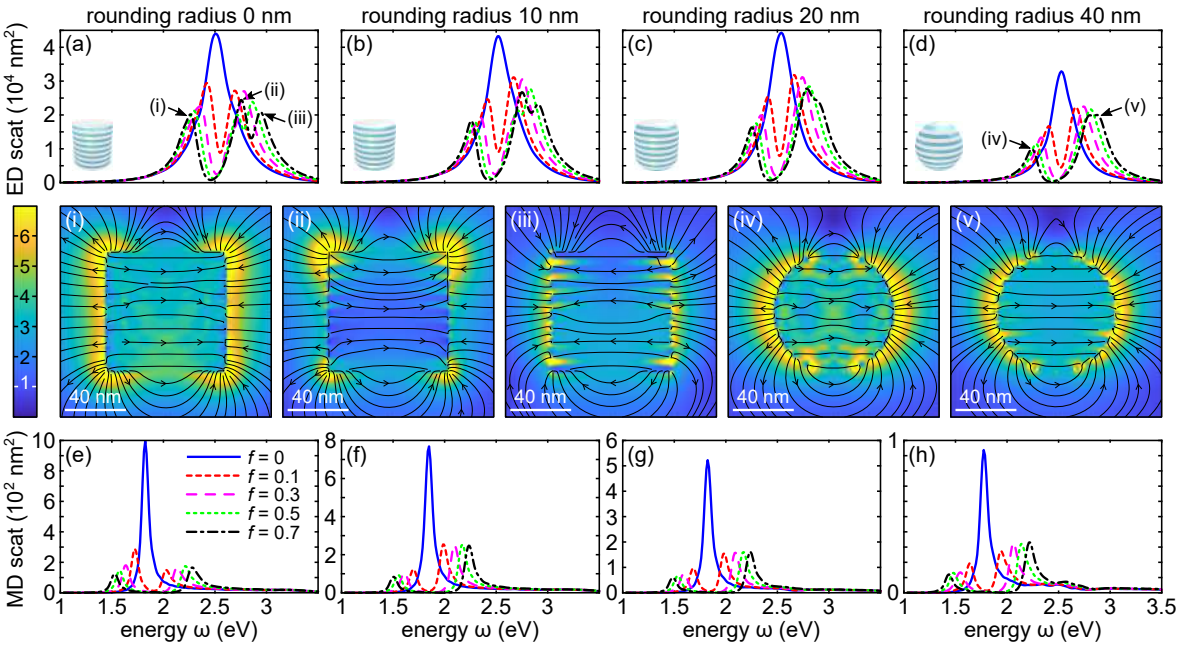

Figure 6.6: Spectra of strongly coupled (a-d) ED and (e-h) MD modes of hyperbolic nanodisks ($r = 40$ nm, $h = 80$ nm) as function of edge rounding for oscillator strengths from 0 to 0.7. (i)-(v) Electric field xz cross sections (intensity and field lines) of the LP/UP of the ED with $f = 0.7$ show that (ii, iii) the UP splits into two modes for sharp nanodisk edges, while (v) for a nanosphere ($r = 40$ nm) it reverts to one high energy mode. The plane wave is incident from the top along z with the electric field polarized along x.

anti-symmetric boundary conditions through the center to reduce computational effort by a factor of 4, and perfectly matched layer (PML) absorbing boundaries elsewhere.

For multipole analysis, we employ the Multipole Expansion for NanoPhotonics (MENP) toolbox, implementing the multipole decomposition approach detailed in Section 4.2.1. The electric field $\mathbf{E}(\mathbf{r})$ is used to calculate equivalent current density distributions:

$$\mathbf{J}(\mathbf{r}) = -i\omega\epsilon_0(\epsilon - 1)\mathbf{E}(\mathbf{r}), \tag{6.9}$$

where ϵ_0 is the vacuum permittivity. Subsequently, multipole contributions are calculated from current densities using the exact multipole expansion formulas from Section 4.2.1, focusing on ED and MD partial scattering cross-sections.

Figure 6.6 displays the multipolar scattering cross-sections for the two primary modes: ED and MD multipoles. The cross-sections are analyzed across varying oscillator strengths from 0.1 to 0.7 for ED modes (Fig. 6.6a-d) and MD modes (Fig. 6.6e-h), with comparisons made against structures without excitons. Beyond oscillator strength variations, the particle geometry is systematically modified from a sharp hyperbolic nanodisk to a rounded nanosphere by progressively rounding the top and bottom edges (shown in insets).

For both mode types, the metal-exciton multilayer structure clearly exhibits lower LP and UP branches, with Rabi splitting that strengthens as oscillator strength f increases. A notable feature appears in the ED mode of the sharp nanodisk: when $f > 0.3$, the UP branch bifurcates into two separate branches (Fig. 6.6a, 0 nm edge rounding). This splitting gradually disappears as edge rounding increases, though some UP broadening persists even in the fully rounded nanosphere configuration (Fig. 6.6d, 40 nm maximum edge rounding).

To understand this splitting behavior, Figure 6.6i-v shows xz cross-sections of electric field intensities and field line distributions at selected resonance peaks for both the hyperbolic nanodisk (i-iii) and nanosphere (iv, v) geometries. The field patterns reveal predominantly uniform internal fields and external field profiles characteristic of electric dipole sources across all cases. This uniformity in ED-like field distributions indicates minimal contribution from higher-order multipolar effects to the observed splitting.

Symmetry analysis confirms that these particles possess $D_{h\infty}$ point group symmetry, making the MQ the lowest-order multipole that can couple to the ED mode. However, quantitative evaluation shows the MQ contribution is five orders of magnitude weaker than the ED values in Fig. 6.6a. Therefore, the mode splitting stems purely from the geometric effect of sharp particle edges. As edge rounding increases, the distinction between edge-localized and volume-distributed modes diminishes, causing the split peaks to merge into a single UP branch while maintaining pure ED character. The LP branch consistently exhibits single-mode behavior across all ED configurations.

In contrast, MD scattering spectra demonstrate straightforward LP/UP profiles regardless of edge rounding or oscillator strength, indicating that magnetic dipole modes represent collective excitations spanning the entire hyperbolic nanodisk volume. The MD mode couples inherently with the EQ mode, as depicted in Figure 6.3.

6.3.1. Metal Fill Factor Dependence

Having established the existence of strong coupling in nanodisks with explicit metal-exciton multilayers, we investigate the impact of metal fill factor on coupling strength, building upon the fill factor analysis from Section 5.2.3. Understanding this dependence is crucial for optimizing device performance and provides insights into the fundamental mechanisms underlying the coupling process. We retain the $r = 40$ nm and $h = 2r$ geometry with 5 nm edge rounding radius. The metal fill factor varies from 0.1 to 0.9, with oscillator strength restricted to $f \leq 0.3$ to maintain well-defined polaritons and enable accurate fitting with the coupled oscillator model.

Exemplary scattering spectra for metal fill factors f_m of 0.1, 0.3, and 0.5 are presented in Figure 6.7a-f. These results demonstrate unambiguous blue shifts of both ED and MD resonances as metal fill factor increases, consistent with previous observations from Chapter 5. The ED mode initially increases in amplitude but begins to broaden for larger fill factors. In contrast, the uncoupled MD only increases in amplitude while maintaining constant, small width.

Coupled spectra for the considered f-values are fitted using the coupled oscillator model for scattering from equation 4.53, with resulting coupling strengths plotted in Figure 6.7g. The analysis confirms the previous results which show, that for self-hybridized hyperbolic nanospheres with metal fill factor 0.5 the MD consistently shows larger coupling strength than the ED. Indeed, for the nanodisks studied here, the MD interaction strength with embedded excitons exceeds ED when $f_m \geq 0.35$, with maximum MD coupling at $f_m \approx 0.7$.

Conversely, ED interaction strength peaks at $f_m \approx 0.3$ then rapidly decreases, falling below MD for $f_m > 0.4$. The self-hybridized MD coupling strength varies less across the entire metal fill factor range than ED, highlighting greater robustness under geometric variations. This monotonous MD coupling strength increase to $f_m = 0.7$ occurs while excitonic material volume decreases, indicating very strong internal electric field localization in hyperbolic nanoparticles.

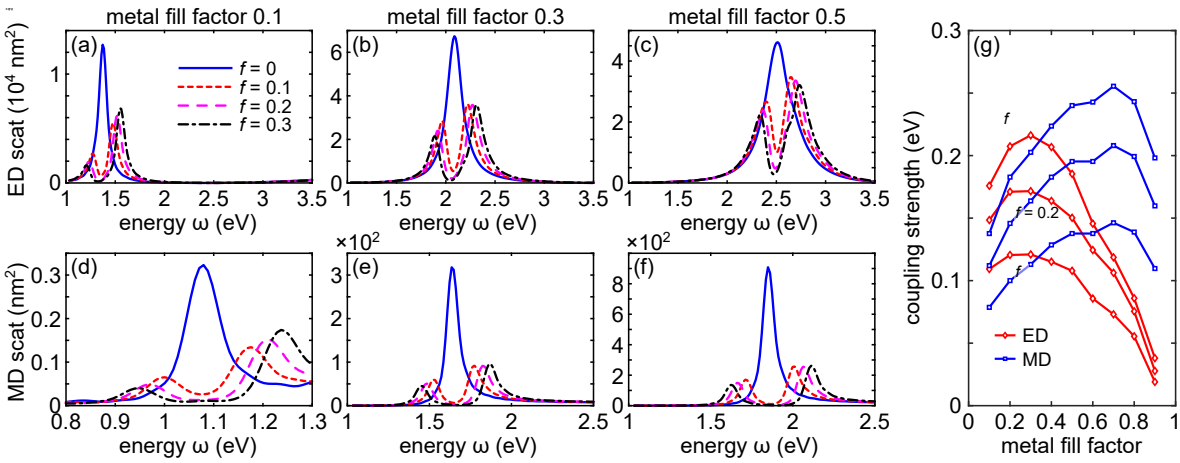

Figure 6.7: Dependence of the coupling strength on the metal fill factor 0.1, 0.3, 0.5 for nanodisks with $r = 40$ nm, $h = 2r$, and rounding radius of 5 nm. (a–c) Electric dipole and (d–f) magnetic dipole scattering spectra. In both cases a blue shift of the modes is observed with increasing fill factor. (g) Coupling strength dependence on the metal fill factor for the (red diamonds) ED and (blue squares) MD shows stronger interaction of the ED with excitons for fill factors smaller than ca. 0.35. Conversely, the MD consistently exhibits stronger coupling than the ED at larger fill factors.

6.3.2. Size and Aspect Ratio Dependence

Finally, we examine the influence of size and aspect ratio on self-hybridized coupling strength in hyperbolic nanodisks to understand scalability and design optimization. Given that MD modes in oblate structures are relatively weak, as established in Chapter 5, and thus detrimental to efficient light-matter coupling, we focus on nanodisks with aspect ratio 1 (termed quasi-spherical nanodisks) and aspect ratio 3 (prolate nanodisks), where aspect ratio is defined as $A = h/2r$. We consider structures with $f_m = 0.5$, where for a given quasi-spherical nanodisk size, the corresponding prolate nanodisk has equal volume. Quasi-spherical disks have radii from 40 to 70 nm with equal height, while prolate nanodisks have equivalent volumes. Rounding radii equal 1/8th of respective radii, with f varied from 0.1 to 0.3 to ensure well-defined polariton formation.

All studied systems show self-hybridized ED and MD scattering spectra characterized by two well-developed polaritons whose spectral separation increases with oscillator strength. These spectra are fitted with coupled harmonic oscillator models following the approach from Section 4.4, obtaining coupling strengths g plotted in Figure 6.8.

The coupling strength values are consistently larger for prolate nanodisks in both ED and MD modes. This agrees with the better optical mode traits of prolate shapes discussed in Chapter 5. However, coupling strengths are more similar for magnetic dipoles than electric ones. For MD, the maximum coupling strength difference between quasi-spherical and prolate nanodisks is less than 20 meV, while for ED it exceeds 40 meV.

Moreover, MD coupling strength is less sensitive to increases in resonator volume. It usually decreases by less than 5% when the volume increases more than five-fold. In contrast, for ED, this decrease is usually about 30%. This behavior highlights the strong self-hybridization abilities of magnetic dipoles and emphasizes the advantages of prolate geometry in achieving strong coupling in hyperbolic nanoparticles.

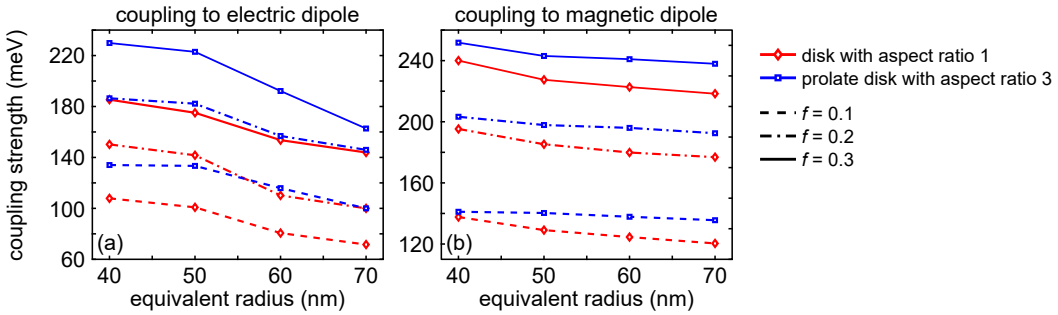

Figure 6.8: Dependence of the self-hybridized coupling strength of (a) the ED and (b) the MD of nanodisks with aspect ratio of $A = 1$ and equal-volume $A = 3$ nanodisk to excitons embedded in the dielectric matrix. The coupling strengths are obtained from fitting the scattering spectra by a coupled harmonic oscillator model. The oscillator strength is $f = 0$, 0.1, 0.2, and 0.3. The coupling strength for both ED and MD modes as a function of nanodisk size and oscillator strength shows consistently larger values for prolate nanodisks.

6.3.3. Comparing Coupling Efficiency of MD and ED Modes in Spherical and Prolate Geometries

The comprehensive analysis presented in this chapter reveals that MD modes achieve strong coupling at significantly lower oscillator strengths than ED modes due to several key factors, building upon the mode characteristics established in Chapter 5:

Linewidth Differences: The MD mode exhibits a significantly narrower linewidth compared to the ED mode in both geometries. For nanospheres, the MD linewidth is ca. 68 meV versus 350 meV for the ED mode, while nanoprolates show 105 meV for MD versus 319 meV for ED. These narrow MD linewidths enable the MD-exciton system to reach strong coupling at remarkably small oscillator strengths of $f_{\mathrm{MD}}^{\mathrm{sc}} \approx 0.04$ for nanospheres and $f_{\mathrm{MD}}^{\mathrm{sc}} \approx 0.03$ for nanoprolates, while the ED-exciton systems require much larger values of $f_{\mathrm{ED}}^{\mathrm{sc}} \geq 0.36$ and $f_{\mathrm{ED}}^{\mathrm{sc}} \geq 0.28$ for nanospheres and nanoprolates, respectively.

Geometric Optimization: Despite having larger MD linewidth than nanospheres, nanoprolates demonstrate stronger coupling efficiency for both MD and ED modes. This counterintuitive result highlights that geometric optimization can overcome linewidth limitations through enhanced field localization and improved mode-exciton overlap. The prolate geometry consistently requires lower oscillator strengths to achieve both strong and ultra-strong coupling regimes compared to spherical geometry.

Ultra-Strong Coupling Accessibility: The efficient MD-exciton interaction enables ultra-strong coupling at remarkably low oscillator strengths. For nanospheres, ultra-strong coupling ($g \geq 0.17$, exceeding 10% of resonance energy) is achieved at $f_{\mathrm{MD}}^{\mathrm{usc}} \approx 0.15$, while nanoprolates reach this regime at $f_{\mathrm{MD}}^{\mathrm{usc}} \approx 0.22$. In contrast, the ED-exciton systems require significantly higher values: $f_{\mathrm{ED}}^{\mathrm{usc}} \geq 0.64$ for nanospheres and $f_{\mathrm{ED}}^{\mathrm{usc}} \geq 0.50$ for nanoprolates. This shows that magnetic dipole modes are better for achieving extreme coupling in both geometries. Prolate structures perform better overall.

Geometric Sensitivity and Robustness: Analysis of nanodisk geometries reveals that MD coupling strength varies less across different metal fill factors compared to ED coupling, indicating greater robustness under geometric variations. The self-hybridized MD coupling strength shows monotonous increase to $f_m = 0.7$ while maintaining consistent performance, whereas ED interaction strength peaks at $f_m \approx 0.3$ then rapidly decreases. This robustness is particularly important for practical device implementations where fabrication tolerances must

be considered.

Size and Volume Scaling: MD coupling strength shows less sensitivity to increases in resonator volume than ED modes. For both spherical and prolate nanodisks, MD coupling usually goes down by less than 5% when volume increases by over five times. In contrast, ED modes typically decrease by around 30%. This better scalability of magnetic dipole interactions is important for practical device applications where size optimization is necessary.

These fundamental differences establish MD modes as the preferred choice for achieving efficient self-hybridized strong coupling in hyperbolic multilayer nanospheroids, with prolate geometries offering the best overall performance. The results demonstrate that hyperbolic metamaterials provide a unique platform for exploring strong light-matter interactions, with magnetic dipole modes offering very good coupling efficiency compared to conventional electric dipole-based approaches. The geometric flexibility of these systems allows for further optimization, making them highly promising for polaritonic device applications.

Chapter 7

Self-Hybridized Strong Coupling of MD Mode to Excitons in Transition Metal Dichalcogenides in Uniaxial Hyperbolic Multilayer Nanospheroids

Results from Chapter 6 demonstrate that the MD mode consistently exhibits greater coupling characteristics compared to the ED mode in both spherical and prolate spheroidal geometries. Building upon these findings of MD mode dominance, this chapter explores the self-hybridized strong coupling of optical modes and excitons using transition metal dichalcogenides (TMDCs) – considering specifically MoS_2, WS_2, $MoSe_2$, and WSe_2 – which exhibit excitons with considerable oscillator strengths. This study focuses on proposing realistic nanostructures, based on spherical or prolate geometries, that will efficiently enable strong coupling to the MD regime. The study maintains consistent dimensions, using a sphere radius of 50 nm and a prolate spheroid with a volume equivalent to that of the sphere.

7.1. Optical Modes in Ag/TMDC Hyperbolic Nanospheroids

Following previous investigations, we consider initially two-layer systems composed of a silver layer and a TMDC layer as shown in Figure 7.1 for spherical and prolate geometries, where the TMDC materials include MoS_2, WS_2, $MoSe_2$, and WSe_2. These TMDCs are character-

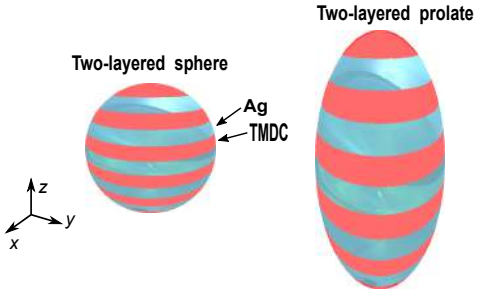

Figure 7.1: Illustrations of the two-layered nanospheroids. Two-layered systems consist of a silver layer and a transition metal dichalcogenide (TMDC) layer. These geometries are represented in both spherical and prolate configurations.

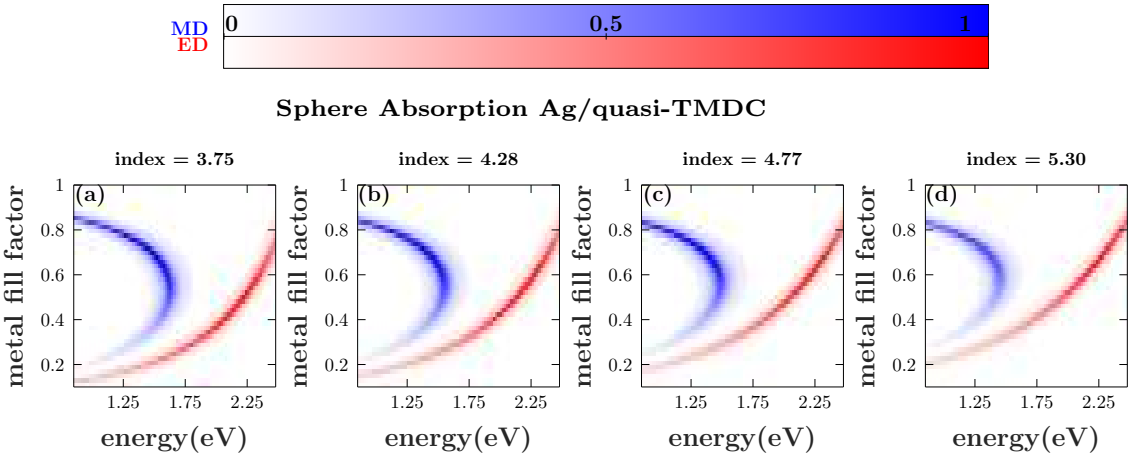

Figure 7.2: Normalized absorption cross-sections, MD (blue color) and ED (red color) mode decompositions for spherical two-layered nanospheroids for dispersionless case under TEM illumination. Results are shown for silver (Ag) and quasi-TMDC: (a-d) for index 3.75, 4.28, 4.77, and 5.30 respectively. The straight vertical mode visible in the plots corresponds to the ED mode. The crescent-like dependence of the MD mode reflects the influence of the metal fill factor on anisotropic optical properties.

ized by an anisotropic dielectric permittivity tensor with large birefringence values and low absorption in the near-infrared range, categorizing them as uniaxial hyperbolic TMDCs [158]. The T-matrix method is used as established in Section 4.3 with a homogenised anisotropic effective diagonal permittivity tensor components given by equations (5.1) and (5.2). The only qualitative difference is that in the above equations the dielectric permittivity of the TMDCs is already anisotropic, hence the ε_d is in tensor form.

Use of TMDCs instead of silica as the dielectric medium in a hyperbolic stack introduces an important difference. The dielectric permittivity is in this case significantly different and will affect the spectral positions of the ED and MD modes. To establish the magnitude of this fundamental change, we begin with a simple case of a dispersionless material (i.e. quasi-TMDC with large refractive indices) that isolates geometric and structural effects from the influence of material resonances. This approach creates clear reference points for mode positions and strengths across varying metal fill factors, providing essential baseline data for subsequent comparison with dispersive systems.

Figure 7.2(a-d) shows the normalized absorption cross-sections and mode decompositions for spherical Ag/quasi-TMDC nanospheroids in the dispersionless case under TEM illumination. The constant refractive indices are 3.75, 4.28, 4.77, and 5.30 and are in the range of typical TMDCs. The characteristic behavior of each mode is preserved with the MD mode (blue) exhibiting the distinctive crescent-like shape (see Chapter 5) for uniaxial hyperbolic nanospheroids. The ED mode is shifted to the blue of the MD mode and exhibits a constant blue shift with increasing metal fill factor. The clear separation between the two mode types in a spherical geometry is as before for a Ag/silica hyperbolic material, however, the modes are considerably shifted to the red.

Having established the baseline mode characteristics, specifically the spectral position of both modes, we now examine how excitons in the selected TMDCs interact with the ED and MD optical modes. Figure 7.3(a-d) presents absorption spectra of these modes in the presence of TMDCs (MoS_2, $MoSe_2$, WS_2, WSe_2) modeled using their full dispersive permittivity for

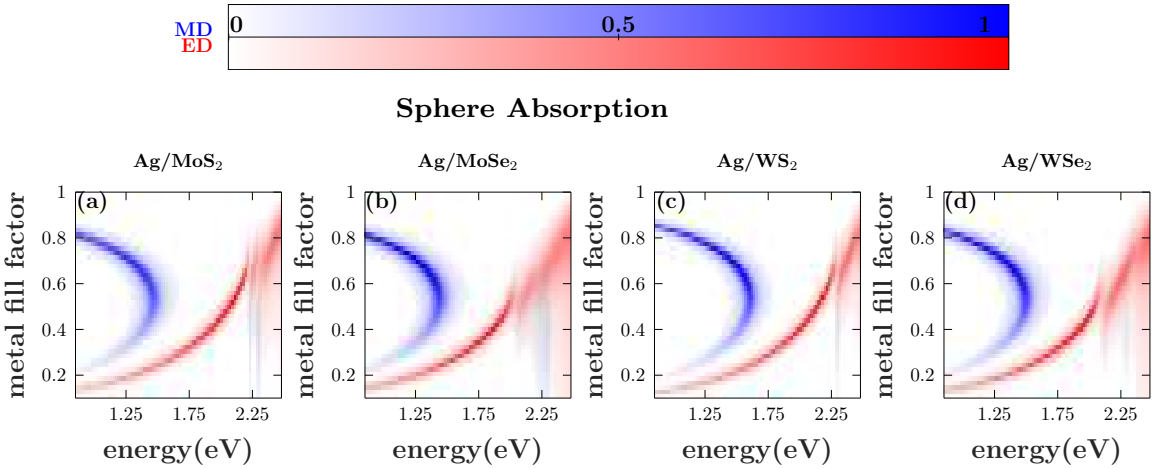

Figure 7.3: Normalized absorption cross-sections, MD (blue color) and ED (red color) mode decompositions for spherical two-layered nanospheroids for dispersive case under TEM illumination. Results are shown for silver and TMDC materials: (a-d) for MoS_2, $MoSe_2$ WS_2, and WSe_2 respectively. The anticrossing behavior visible in the plots is the coupling of ED mode to the exciton. The crescent-like dependence of the MD mode reflects the influence of the metal fill factor on anisotropic optical properties.

spherical nanoparticles under TEM illumination. Unlike in the dispersionless case, the presence of excitons (in the range of ca. 1.5 to 2.1 eV) modifies the spectra in the relevant energy range. Due to the spectral characteristics of the modes, only coupling of excitons to the ED mode is observed. The MD mode maintains its characteristic crescent-like shape, though its spectral position and strength are now additionally influenced by the real dispersion. However, it does not interact with excitons of any of the TMDCs.

Clearly the high refractive index of TMDCs shifts the modes, especially the MD one, too far to the red. Based on previous results, this effect can be reversed by employing geometrical effects established in Chapter 5. Hence, we now examine prolate nanospheroids using identical material compositions and analytical approaches. Figures 7.4 and 7.5 present the results for Ag/TMDC prolate nanospheroids in both dispersionless (quasi-TMDC) and dispersive cases, respectively. For the dispersionless case (Figure 7.4), we retain the refractive indices as in the spherical analysis (3.75, 4.28, 4.77, and 5.30), while the dispersive case (Figure 7.5) uses the same fully dispersive TMDCs as in the spherical case.

A key distinction emerges when comparing the two geometries: in the prolate nanospheroids, the MD mode is significantly shifted to the blue and partially overlaps with the ED mode, as evidenced in Figure 7.4 This contrasts sharply with the spherical geometry, which demonstrates a clearer separation between the MD and ED modes with no significant overlap. However, despite the blue shift, full coupling between both ED and MD modes with excitons is not observed. As with the spherical geometry in the dispersive case, the prolate nanospheroids exhibit anticrossing behavior only with the ED mode, Figure 7.5(a-d). Only very weak mixing of the MD mode with the excitons is visible for $MoSe_2$ and WSe_2, however, it is not clear if this is a strong couplign effect or the generation of a mode due to an increased refractive index (pure dielectric-like response).

The absence of MD-exciton coupling in two-layered systems presents a significant limitation for achieving the desired self-hybridized strong coupling in the MD regime. From these initial calculations it is clear, that simple geometric manipulation by the metal filling factor

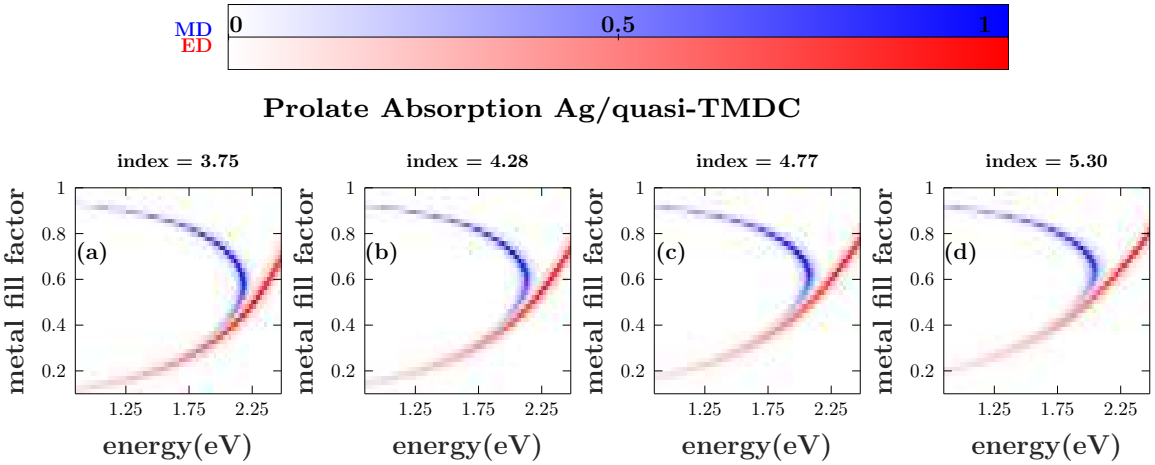

Figure 7.4: Normalized absorption cross-sections, MD (blue color) and ED (red color) mode decompositions for prolate two-layered nanospheroids for dispersionless case under TEM illumination. Results are shown for silver (Ag) and a dispersionless quasi-TMDC material: (a-d) for index 3.75, 4.28, 4.77, and 5.30 respectively. The straight vertical mode visible in the plots corresponds to the ED mode. The prolate geometry exhibits an overlap between the MD and ED modes, contrasting the clearer separation observed in the spherical geometry.

and geometry is insufficient to enable MD-exciton coupling. While the shift to a prolate geometry partially overcomes the red shift of the modes caused by the large refractive index of TMDCs, its effect clearly too weak. Hence, it is necessary to address the former effect and a simple solution is by decreasing the refractive index of the dielectric layers that form part of the hyperbolic metamaterial stack. However, at the same time it is necessary to keep the TMDCs for their excitonsic properties. To address this challenge and enable MD-exciton interactions, it is proposed to utilize a modified three-layered design, that will incorporate an additional dielectric spacer layer with a lower refractive index than that of TMDCs. Such an approach is expected to yield a *corrective* blue shift of the modes while retaining the strong excitonic response of TMDCs.

7.2. Optical Modes in Three-Layer Ag/TMDC/Silica Hyperbolic Nanospheroids

The results from the preceding section demonstrate that MD coupling to excitons is not feasible in two-layer Ag/TMDC nanospheroids. To address this limitation, an additional material (silica, $n = 1.5$) is introduced as a dielectric spacer between the silver and TMDC layers, as depicted in Figure 7.6. This structural modification is designed to effectively decrease the dielectric component of the hyperbolic metameterial to modify the electromagnetic field distribution and enable MD-exciton interactions that were absent in the two-layer configuration.

For the three-layer Ag/TMDC/silica nanospheroids, the FDTD method is employed instead of the T-matrix approach due to the failure of the Maxwell-Garnett mixing for three-component multilayers, increased computational complexity of the three-layer system and the need for detailed field distribution analysis. In the FDTD approach we utilize a non-uniform spatial mesh with discretization of 4 nm outside the nanoparticle and 1 nm resolution over the nanoparticle, incorporating a graded transition between mesh regions. A plane wave propagating along the z-axis is implemented via TFSF in the energy range of 1 to 2.5 eV. The

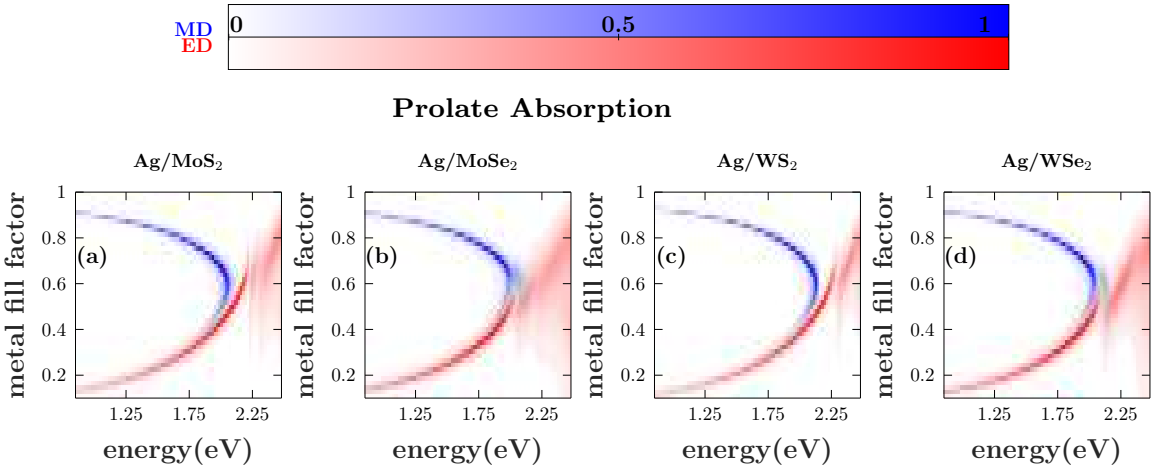

Figure 7.5: Normalized absorption cross-sections, MD (blue color) and ED (red color) mode decompositions for prolate two-layered nanospheroids for dispersive case under TEM illumination. Results are shown for silver and TMDC materials: (a-d) for MoS_2, $MoSe_2$ WS_2, and WSe_2 respectively. The anticrossing behavior visible in the plots is the coupling of ED mode to the exciton. The prolate geometry exhibits an overlap between the MD and ED modes, contrasting the clearer separation observed in the spherical geometry.

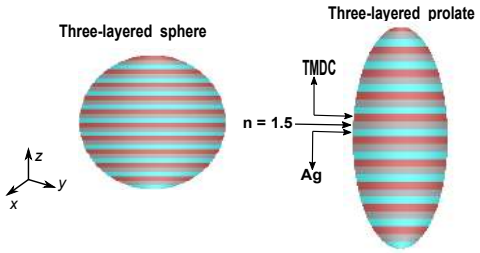

Figure 7.6: Illustrations of the three-layered nanospheroids. Three-layered systems include an intermediate silica layer (refractive index $n = 1.5$) between the silver and TMDC layers. These geometries are represented in both spherical and prolate configurations.

simulation volume is reduced using anti-symmetric and symmetric boundary conditions along the x- and y-axis, respectively, and perfect matching layer (PML) absorbing boundaries in other directions. The simulation monitors include near-field probes to record electric field distributions $E(x, y, z, f)$ and far-field monitors to measure scattering and absorption cross-sections. Convergence is ensured through divergence checking and an auto shutoff criterion with a threshold of energy remaining in the simulation to 10^{-5} of the maximum.

When considering a metal fill factor analysis, it is now necessary to consider the total thickness as a sum of three values with the fractional sum being equal to 1. Following the methodology established for two-layer systems, we first investigate the dispersionless case to establish the spectral shifts with a quasi-TMDC ($n = 4.28$) and silica (Ag/silica/quasi-TMDC). We consider two material cases with the quasi-TMDC fraction fixed at 0.1 and 0.3, while the silver/silica fractions vary from 0 to the respective maxima ensuring total volume fraction of 1.

The resulting normalized total absorption plot for the spherical geometry is shown in Figure 7.7(a-b), while the prolate geometry results are shown in Figure 7.7(c-d). The modes

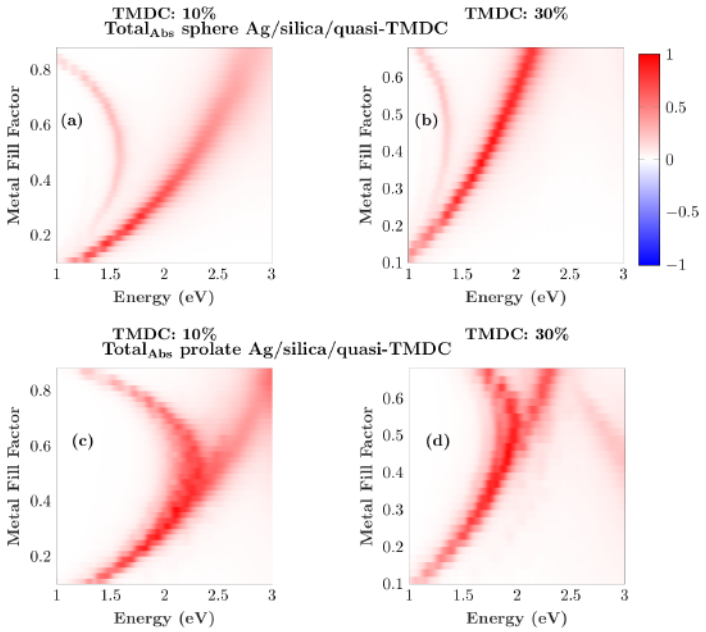

Figure 7.7: Normalized total absorption cross-section calculated using the FDTD method for dispersionless case under TEM illumination for (a-b) three-layered spherical nanospheroids and (c-d) three-layered prolate nanospheroids. Results are shown for Ag/silica/quasi-TMDC structure, where the quasi-TMDC fraction is fixed at 10% and 30%. The metal fill factor and silica are varied.

are qualitatively similar to those plotted for the two-layer Ag/quasi-TMDC systems. The MD mode maintains a crescent-like shape and the ED mode curves vertically to the blue. For both spherical and prolate geometries and both quasi-TMDC factions the results are similar, but a significant blue shift is observed for the lower amount of the quasi-TMDC. This proves conclusively that mixing of TMDCs and silica as the dielectric with silver is a solid approach to enabling MD-exciton coupling. Thus, we can now examine how the three-layer hyperbolic material operates in practice when accounting both for dispersion and the excitonic features.

For the dispersive material case, two distinct configurations are investigated to systematically explore the parameter space: First, the TMDC volume fraction is fixed at 0.1 while the silver and silica volume fractions are varied from 0.1 to 0.8, with their combined sum maintaining the total volume fraction of 1. Second, the silica volume fraction is fixed at 0.1 while the silver and TMDC volume fractions are varied from 0.1 to 0.8, with their combined sum maintaining the total volume fraction of 1. The results for both configurations are shown in Figures 7.8 and 7.9, respectively, for spherical and prolate geometries using four TMDCs: MoS_2, $MoSe_2$, WS_2, and WSe_2.

These results demonstrate that anticrossing behavior in the MD regime emerges when systematically varying the volume fractions while maintaining a fixed volume of either silica or TMDC. For spherical geometries, no strong MD coupling with the excitons is observed, despite the introduced modifications. The MD mode maintains its characteristic crescent-shaped dependence, while the anticrossing behaviors shown in Figure 7.8 arise from the ED mode strongly coupling to the excitons. The anticrossing behavior occurs at different metal fill factor ranges depending on the fixed material: for fixed TMDC fraction, it appears at lower metal fill factors (0.1 to 0.4), while for fixed silica, it occurs at higher metal fill factors

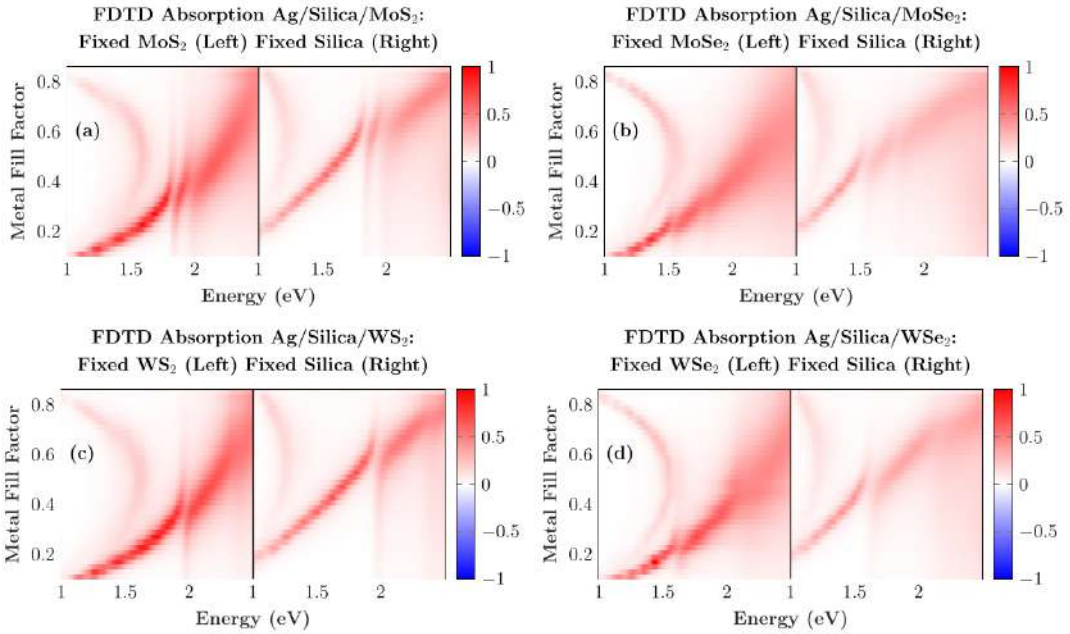

Figure 7.8: Normalized total absorption cross-section for three-layered spherical nanospheroids calculated using the FDTD method. Results are shown for TMDCs: MoS_2 (a), $MoSe_2$ (b), WS_2 (c), and WSe_2 (d). Left panels represent cases with fixed TMDC volume fraction of 0.1, and right panels represent cases with fixed silica volume fraction of 0.1. Anticrossing behavior of the ED mode is observed as the metal fill factor is varied.

(0.42 to 0.8).

In contrast, prolate geometries demonstrate that efficient MD-exciton coupling is possible. While the MD mode overlaps with the ED one, what is consistent with the mode properties of two-layer prolate nanospheroids and the geometric effects established in Chapter 5, full minima and anticrossing behavior is seen in Figure 7.9. Most significantly, strong MD coupling to excitons is observed for specific configurations: when TMDC is fixed at 0.1, MoS_2 and WS_2 show strong MD coupling to excitons, as demonstrated in Figure 7.9(a,c). Conversely, when silica is fixed, $MoSe_2$ and WSe_2 exhibit MD anticrossing with weak exciton coupling, as shown in Figure 7.9(b,d). The anticrossing behavior exhibits a distinct pattern with respect to the metal fill factor: in the range of 0.1 to 0.5, the modes shift toward the red region, while from 0.52 to 0.88 metal fill factor, the modes reverse direction and begin shifting toward the blue region.

These findings show the first successful instance of MD-exciton self-hybridized strong coupling through careful geometric and compositional design. To confirm the practical use of these results and offer a way for experimental realization, we will now look at multilayer nanodisk structures that can be made using standard lithographic techniques [157].

7.3. Self-Hybridization in Ag/Silica/TMDC Nanodisks

The subsequently investigated nanostructures are based on a realistic possiblity of fabricating a three layer Ag/silica/TMDC hyperbolic nanodisk via lithography and reactive ion etching of a preassembled stack with a hard metal mask to protect and form the nanopatricles. A

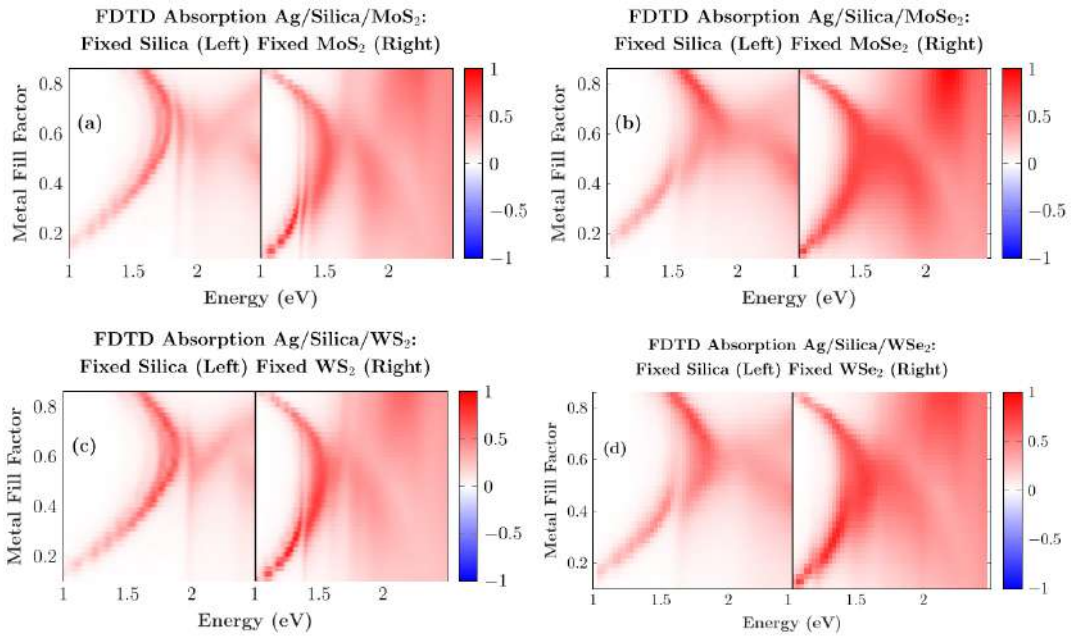

Figure 7.9: Normalized total absorption cross-section for three-layered prolate nanospheroids calculated using the FDTD method. Results are shown for TMDCs: MoS_2 (a), $MoSe_2$ (b), WS_2 (c), and WSe_2 (d). Left panels represent cases with fixed silica volume fraction of 0.1, and right panels represent cases with fixed TMDC volume fraction of 0.1. Strong MD coupling to excitons is observed in MoS_2 and WS_2, with anticrossing behaviors marked by distinct red and blue shifts depending on the metal fill factor.

nanodisk geometry provides a more experimentally accessible platform while maintaining the essential physics of the spheroidal systems. The geometrical parameters are based on those investigated in the previous section for both quasi-spherical (aspect ratio of 1) and prolate nanodisks. The sphere has a radius of 50 nm, and the prolate spheroid has a volume equivalent to that of the sphere, although the edges are not rounded. With the larger losses due to absorption in the TMDCs, the nanodisk has narrow spectral features even with sharp edges, as in the case of idealized spheroidal geometries. The FDTD simulations are carried out with the same parameters as for the spheroidal nanostructures.

Figures 7.10 and 7.11 show the normalized total absorption for, respectively, spherical and prolate nanodisks using four TMDCs: MoS_2, $MoSe_2$, WS_2, and WSe_2 for the case of fixed TMDC. The results are consistent with Figures 7.8 and 7.9, showing similar optical responses and confirming that the nanodisk geometry successfully preserves the essential physics observed in the spheroidal systems. This consistency validates the use of nanodisks as a practical platform for experimental implementation of MD-exciton strong coupling. Most importantly, clear anticrossing spectra are visible in both Figures. In the subsequent quantification of strong coupling we will focus only on the hyperbolic nanoparticles with WS_2 and MoS_2, since their spectra demonstrate the clearest/largest anticrossing.

To quantify the interaction rates in the self-hybridized nanoparticles a detailed analysis of the spectra decomposed into the constituent modes is essential. The analysis of MD strong coupling involves the decomposition of the FDTD total scattering cross-section into its MD components using the MENP program, following the multipole decomposition methodology detailed in Section 4.2.1.

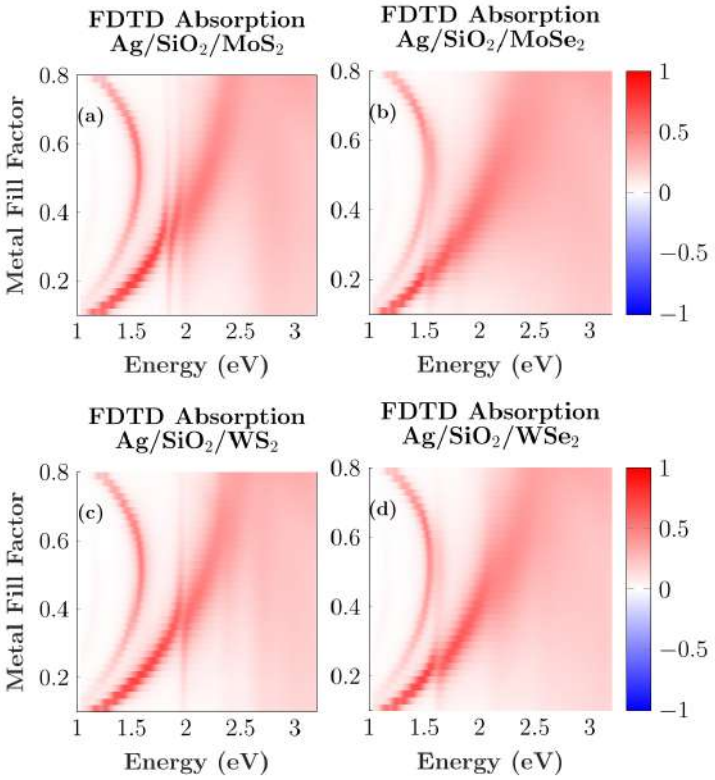

Figure 7.10: Normalized total absorption cross-section for three-layered spherical nanodisk calculated using the FDTD method. Results are shown for TMDCs: MoS_2 (a), $MoSe_2$ (b), WS_2 (c), and WSe_2 (d). These represent cases with fixed TMDC volume fraction of 0.1. Anticrossing behavior of the ED mode is observed as the metal fill factor is varied.

The scattering cross section decomposed into MD and ED modes for WS_2 and MoS_2 is shown in Figure 7.12. This decomposition provides the foundation for quantitative analysis of the coupling strength and Rabi splitting characteristics, enabling precise characterization of the strong coupling regime. The clear separation of MD and ED contributions allows for individual analysis of each mode's interaction with the exciton resonances.

7.4. Strong Coupling in Ag/Silica/WS_2 and Ag/Silica/MoS_2 Prolate Nanodisk

Building upon the mode decomposition results, we now provide comprehensive characterization of the strong coupling phenomena in the most promising material systems: Ag/silica/WS_2 and Ag/silica/MoS_2 prolate nanodisks. The characterization of the strong coupling in the system focuses on the metal fill factor range of 0.2 to 0.4, as this range properly captures the anticrossing behavior and enables accurate extraction of coupling parameters. The characterization proceeds through two consecutive steps: first, we establish the uncoupled mode behavior by removing exciton contributions from the material response, then we analyze the full coupled system to extract coupling strengths and anticrossing characteristics.

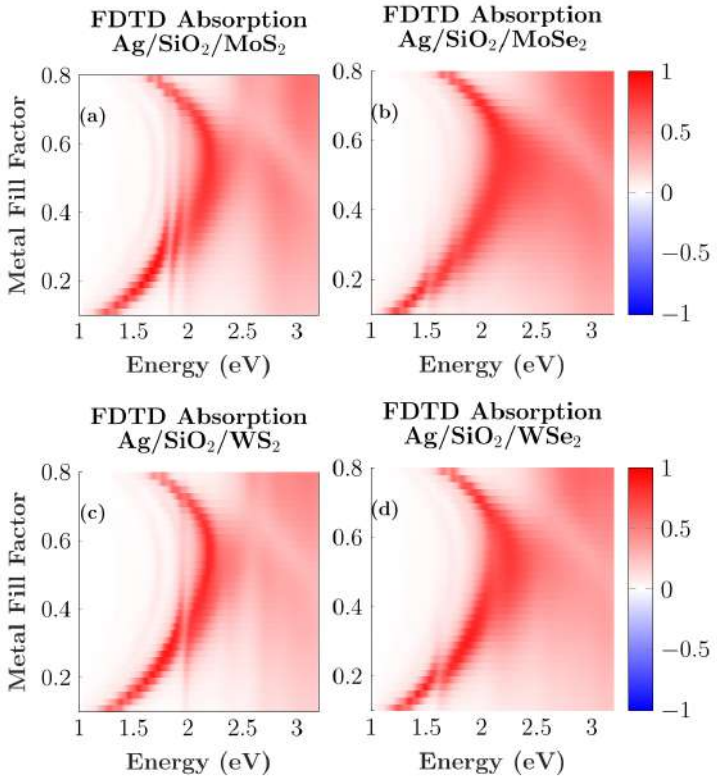

Figure 7.11: Normalized total absorption cross-section for three-layered prolate nanodisk calculated using the FDTD method. Results are shown for TMDCs: MoS_2 (a), $MoSe_2$ (b), WS_2 (c), and WSe_2 (d). These represent cases with fixed TMDC volume fraction of 0.1. The ED and MD modes overlap which is consistent with prolate geometry. Strong MD coupling to excitons is observed in MoS_2 and WS_2.

7.4.1. Uncoupled and Coupled Mode Characterisation

To characterize the strong coupling regime, we first establish the dispersion relations of the uncoupled modes (MD and ED) and the exciton as a function of metal fill factor (f_m). The uncoupled modes are determined by calculating the scattering cross-section of equivalent structures whose TMDC material dispersion has had its excitonic response removed. This is achieved by fitting the permittivity data of WS_2 and MoS_2 using the Tauc-Lorentz oscillator model [159, 160]

$$\mathrm{Im}\left[\varepsilon_{t,n}(E)\right] = \begin{cases} \frac{A_n E_{0n} B_{nm}(E-E_{gn})^2}{\left((E^2-E_{0n}^2)^2+B_{nm}^2E^2\right)E}, & E > E_{gn} \\ 0, & E \leq E_{gn} \end{cases} \tag{7.1}$$

where n is the number of oscillators, E_{0n} is the center energy of the nth element, E_{gn} the band gap energy of the oscillator of the nth element, B_{nm} the broadening of the oscillator of the nth element, and A_n the amplitude of the oscillator of the nth element. The real part is calculated via the Kramers-Kronig transformation.

Here the fit is done over an energy range of 0.7 to 2.5 eV and then we omit the A, and if needed the B, excitons (that couple to the ED and MD modes) from the permittivity. This fitted permittivity, representing the background dielectric response, is used as the third layer in the Ag/silica/TMDC stack. The total scattering cross-section of this uncoupled system is

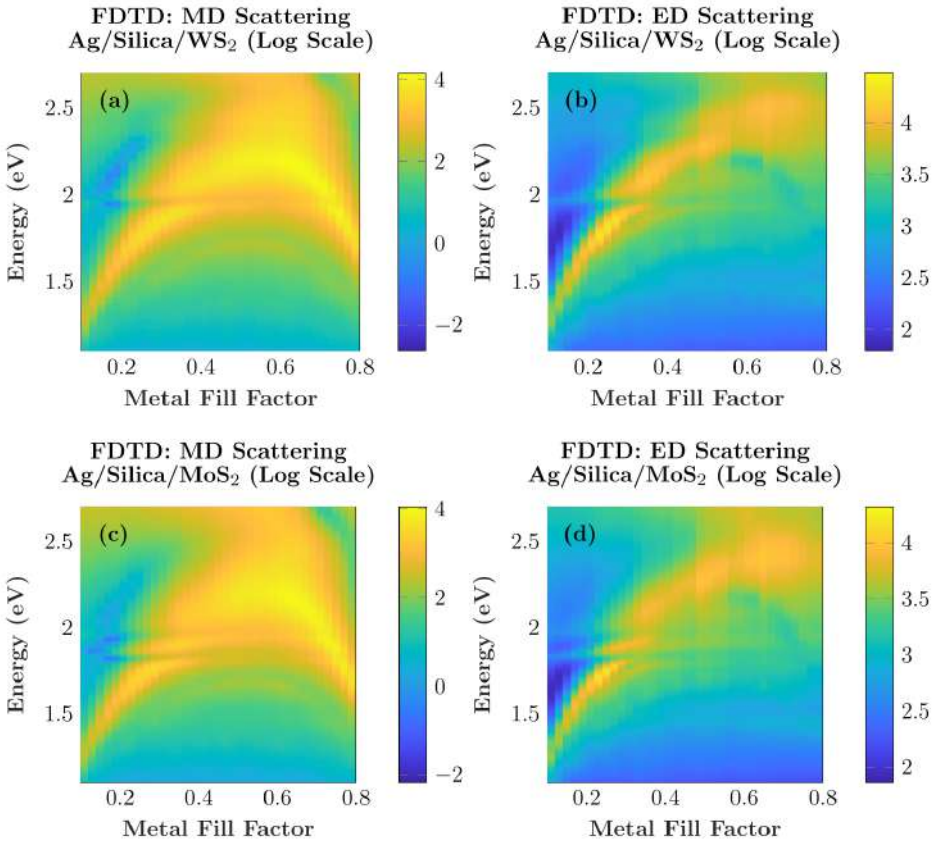

Figure 7.12: Disperstion of the scattering cross-sections decomposed into MD and ED contributions for (a-b) Ag/silica/WS_2 and (c-d) Ag/silica/MoS_2 prolate nanodisks.

then decomposed into MD and ED contributions using the MENP program (as detailed in Section 4.2.1). A Lorentzian model is fitted to these decomposed spectra for each fill factor to extract the uncoupled MD and ED resonance energies, with linewidths fixed at $\gamma_{\mathrm{MD}} = 0.11$ eV and $\gamma_{\mathrm{ED}} = 0.10$ eV.

For the WS_2 system, which features a single exciton, the coupled scattering spectra for each fill factor are fitted using a coupled harmonic oscillator model (from equation 4.53) for the MD and ED modes individually:

$$C_{\mathrm{sca}}(\omega) \propto \omega^4 \left| \frac{\omega_{\mathrm{ex}}^2 - \omega^2 - i\gamma_{\mathrm{ex}}\omega}{(\omega_{\mathrm{MD/ED}}^2 - \omega^2 - i\gamma_{\mathrm{MD/ED}}\omega)(\omega_{\mathrm{ex}}^2 - \omega^2 - i\gamma_{\mathrm{ex}}\omega) - \omega^2 g^2} \right|^2 . \tag{7.2}$$

Here, $\gamma_{\mathrm{ex}} = 0.05$ eV is fixed. From these fits, we extract the coupled mode energies and the coupling strength g. The dispersion of the coupled MD (blue color) and ED (red color) modes is well-described by the quadratic functions as depicted in Figure 7.13(a):

$$\omega_{\mathrm{MD}} = -2.02 f_m^2 + 3.17 f_m + 1.10,$$
$$\omega_{\mathrm{ED}} = -5.48 f_m^2 + 5.13 f_m + 0.90.$$

A comparison between the uncoupled (black dashed lines) and coupled (black solid lines) MD and ED modes is shown in Figure 7.13(c,e). The agreement is relatively good, with only small systematic shifts that likely arise from neglecting part of the dispersion when evaluating the

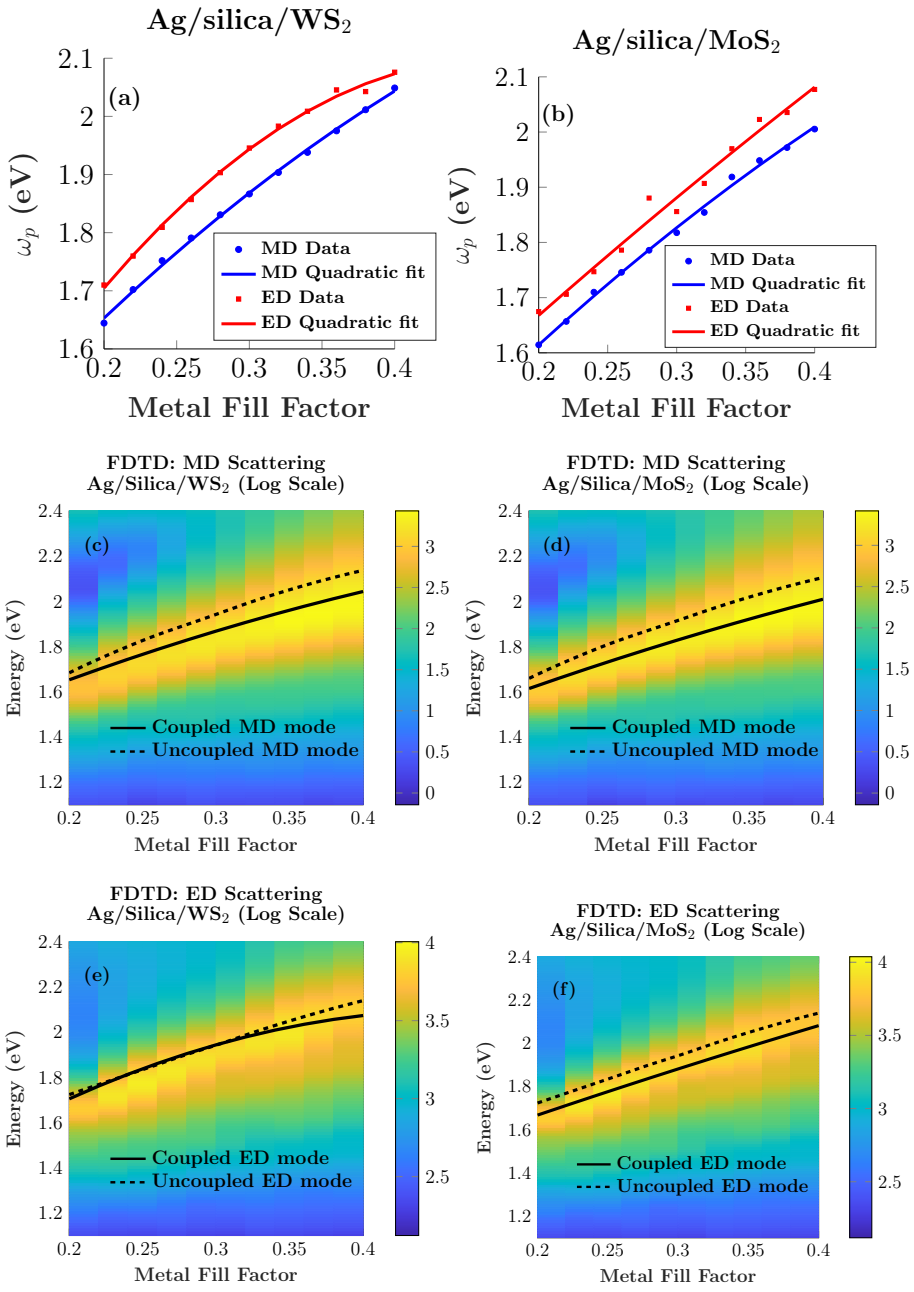

Figure 7.13: (a-b) Coupled MD (blue color) and ED (red color) modes fitted plot for Ag/silica/WS_2 and Ag/silica/MoS_2 compositions respectively. (c-d) Decomposed uncoupled MD modes and (e-f) decomposed uncoupled ED modes for the same compositions, with uncoupled modes as black dashed lines and coupled MD and ED modes as black solid lines.

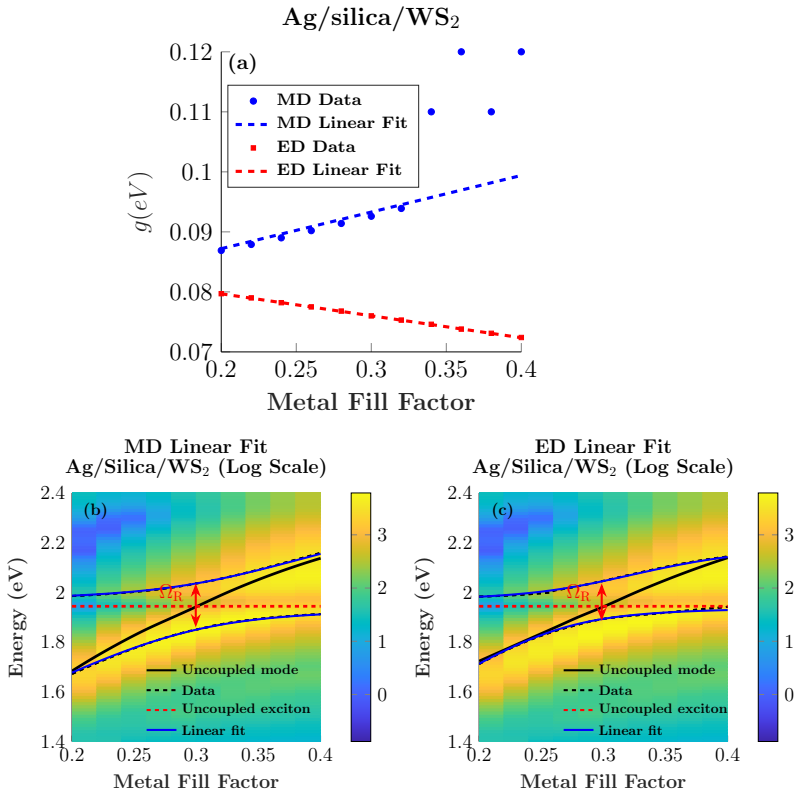

Figure 7.14: (a) The fitted coupling strength plot for MD (blue color) and ED (red color) modes for Ag/silica/WS_2. (b-c) The fitted anticrossings using the linear fitted functions of g for MD and ED modes.

uncoupled modes. The coupling strengths for the MD (blue color) and ED (red color) modes show a linear dependence on f_m as depicted in Figure 7.14(a):

$$\begin{aligned} \text{MD mode:} \quad & g = 0.061 f_m + 0.075, \\ \text{ED mode:} \quad & g = -0.037 f_m + 0.087. \end{aligned}$$

Note, that the signs of the linear terms of the ED- and MD-exciton coupling terms are different. However, they are consistent with the observations made in the preceding Chapter in Figure 6.7g.

In the case of the MoS_2 TMDC inclusion, the behavior is similar to that reported in previous studies [132], but with a key difference: two excitons (A and B) interact with the MD and ED modes rather than with a plasmon mode. We follow a similar methodology, fitting the permittivity data while excluding both A and B exciton transitions. The coupled scattering spectrum for the MD mode is modeled with an extended harmonic oscillator equation from Section 4.4.2:

$$C_{\text{sca}} \propto \omega^4 \Big| \big[(\omega_A^2 - \omega^2 - i\gamma_A\omega)(\omega_B^2 - \omega^2 - i\gamma_B\omega)\big] \times \big[(\omega_{MD}^2 - \omega^2 - i\gamma_{MD/ED}\omega)(\omega_A^2 - \omega^2 - i\gamma_A\omega) \times (\omega_B^2 - \omega^2 - i\gamma_B\omega) - 4\omega^2 g_A^2(\omega_B^2 - \omega^2 - i\gamma_B\omega) - 4\omega^2 g_B^2(\omega_A^2 - \omega^2 - i\gamma_A\omega)\big]^{-1} \Big|^2 \quad (7.3)$$

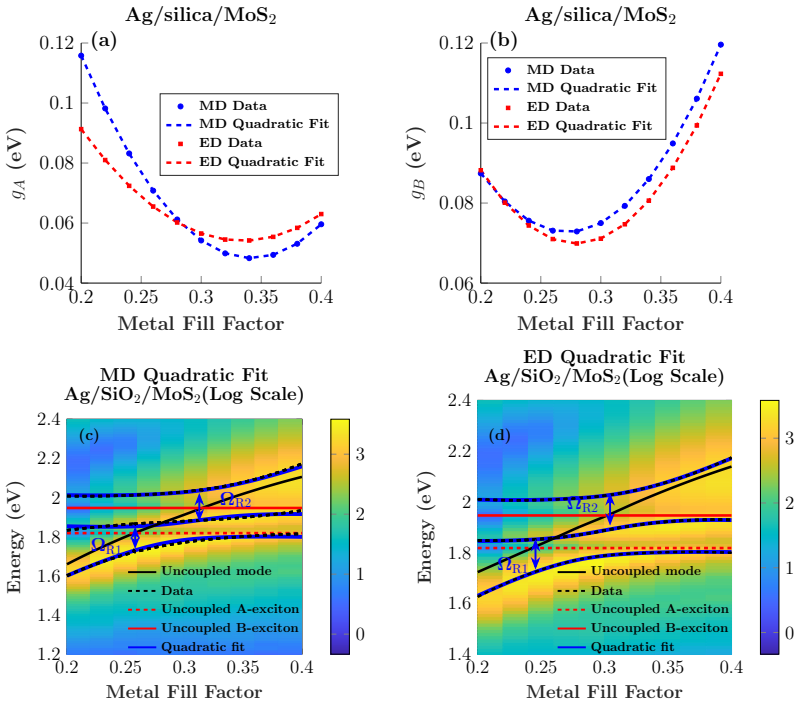

Figure 7.15: (a-b) Fitted coupling strengths g_A and g_B for MD (blue color) and ED (red color) modes in Ag/silica/MoS_2. (c-d) Fitted anticrossings using quadratic functions of g_A and g_B for MD and ED modes.

The linewidths are fixed to $\gamma_{\mathrm{MD}} = 0.1$ eV, $\gamma_{\mathrm{A}} = \gamma_{\mathrm{B}} = 0.05$ eV for the MD mode (blue color), and $\gamma_{\mathrm{ED}} = 0.125$ eV, $\gamma_{\mathrm{A}} = 0.04$ eV, $\gamma_{\mathrm{B}} = 0.08$ eV for the ED mode (red color). The resulting coupled mode dispersions, as depicted in Figure 7.13(b), are:

$$\omega_{\mathrm{MD}} = -1.50 f_m^2 + 2.87 f_m + 1.10,$$
$$\omega_{\mathrm{ED}} = -0.65 f_m^2 + 2.463 f_m + 1.20.$$

Figure 7.13(d,f) compares the uncoupled and coupled MD and ED modes for MoS_2, demonstrating rather good agreement. The coupling strengths g_A and g_B for both MD (blue color) and ED (red color) modes exhibit a quadratic dependence as depicted in Figure 7.15(a-b):

$$\text{MD mode:} \quad g_A = 3.35 f_m^2 - 2.29 f_m + 0.44, \tag{7.4}$$
$$g_B = 2.85 f_m^2 - 1.55 f_m + 0.28, \tag{7.5}$$
$$\text{ED mode:} \quad g_A = 2.06 f_m^2 - 1.38 f_m + 0.28, \tag{7.6}$$
$$g_B = 2.91 f_m^2 - 1.63 f_m + 0.30. \tag{7.7}$$

7.4.2. Anticrossing Characterisation

The strong coupling regime is confirmed by the characteristic anticrossing behavior observed in the polariton dispersion. We model this using a non-Hermitian Hamiltonian approach. For WS_2, the non-Hermitian Hamiltonian model from Section 4.4.1 is used:

$$\hat{H} = \begin{pmatrix} \omega_{\mathrm{opt}} - i\gamma_{\mathrm{opt}}/2 & g \\ g & \omega_{ex} - i\gamma_{ex}/2 \end{pmatrix}, \tag{7.8}$$

where opt stands for the optical ED or MD mode. The optical mode frequencies $\omega_{\text{opt}}(f_m)$ and coupling strengths $g(f_m)$ are given by the quadratic and linear functions defined in the preceding section. To fit the anticrossing data, the linewidths γ_{ex} and γ_{opt} are fixed, and the exciton resonance ω_{ex} is treated as a free parameter. The functional forms for the mode frequency and coupling strength are scaled by independent fitting parameters a_1 and a_2 (where $0 \leq a_1, a_2 \leq 1$) such that $\omega_{\text{opt}} = a_1 \cdot \omega_{\text{opt}}(f_m)$ and $g = a_2 \cdot g(f_m)$. This two-parameter approach allows for independent adjustment of the energy scaling and interaction strength to achieve the optimal fit to the anticrossing data.

In our model, the scaling parameters a_1 and a_2 are introduced not as arbitrary fitting factors, but to account for systematic deviations between the simplified coupled-oscillator Hamiltonian and the full-field FDTD simulations with experimental material data. Without scaling, the fitted dispersion fails to reproduce the expected condition at zero detuning, where the Rabi splitting must satisfy $\Omega_R = 2g$. The scaling ensures consistency between the theoretical coupling strength and the simulated response, which is particularly important since the TMDC permittivity is directly taken from experiment, and the multilayer geometry (Ag/silica/TMDC) supports both MD and ED optical modes that couple differently to the exciton. Importantly, the scaling factors remain within the physical range (0–1) and are applied globally across all fill factors rather than tuned locally, which avoids overfitting. They act as correction factors that bridge the gap between the simplified analytical model and the rigorous numerical results. Thus, their use is justified as a minimal adjustment ensuring quantitative consistency with physical constraints, rather than an artificial fitting tool.

The eigenvalues of this parameterized Hamiltonian are calculated to generate the fitted anticrossing plots in Figure 7.14(b-c) for the hyperoblic nanostructure with WS_2.

To validate the self-consistency of the anticrossing fit, we confirmed that the Rabi splitting at zero detuning (Ω_R) matched the value expected from the scaled coupling strength used in the Hamiltonian as given below, i.e., $\Omega_R = 2(a_2 \cdot g(f_m))$. This ensures the observed splitting in the anticrossing plot is directly proportional to the coupling parameter that generated it.

Figure 7.14(a) shows the distinct linear dependence of g on fill factor for both modes. The MD mode's (blue color) coupling strength increases with f (positive slope), while the ED mode's (red color) decreases (negative slope), revealing their different interaction mechanisms with the TMDC exciton. The anticrossing behavior shown in Figure 7.14(b-c) exhibits clear Rabi splitting at zero detuning ($\delta = 0$), occurring at $f = 0.30$. The MD mode demonstrates stronger coupling with a larger Rabi splitting ($\Omega_R = 186$ meV and $g = 93$ meV) compared to the ED mode ($\Omega_R = 152$ meV and $g = 76$ meV). These anticrossing patterns reveal distinct upper and lower polariton branches with characteristic avoided crossing behavior. In the figures, the uncoupled exciton is represented by a red dashed line, the uncoupled MD/ED mode by a black solid line, the anticrossing data by black dashed lines, and the fitted anticrossings by blue solid lines.

For the MoS_2 system, we employ the extended non-Hermitian Hamiltonian model from Section 4.4.2:

$$\hat{H} = \hbar \begin{pmatrix} \omega_{\text{opt}} - i\frac{\gamma_{\text{opt}}}{2} & g_{\text{A}} & g_{\text{B}} \\ g_{\text{A}} & \omega_{\text{A}} - i\frac{\gamma_{\text{A}}}{2} & 0 \\ g_{\text{B}} & 0 & \omega_{\text{B}} - i\frac{\gamma_{\text{B}}}{2} \end{pmatrix} \tag{7.9}$$

A similar fitting procedure is used. The functional forms for $\omega_{\text{opt}}(f_m)$, $g_A(f_m)$, and $g_B(f_m)$ from the preceding section are scaled by independent parameters a_1, a_2, and a_3 (where $0 \leq a_1, a_2, a_3 \leq 1$), such that $\omega_{\text{opt}} = a_1 \cdot \omega_{\text{opt}}(f_m)$, $g_{\text{A}} = a_2 \cdot g_{\text{A}}(f_m)$, and $g_{\text{B}} = a_3 \cdot g_{\text{B}}(f_m)$. The exciton resonances ω_{A} and ω_{B} are free parameters, while the linewidths $\gamma_{\text{A/B}}$ and γ_{opt} are fixed. This multi-parameter scaling provides greater flexibility to accurately capture the

complex interactions in the three-level system.

Similarly, for the MoS_2 system, the scaling parameters a_1, a_2, and a_3 serve the same purpose of reconciling the simplified Hamiltonian with the full numerical simulations. The complex multilayer structure and the presence of two distinct excitonic resonances necessitate these corrections to maintain physical consistency across the entire parameter space.

The eigenvalues of this parameterized Hamiltonian are calculated to generate the fitted anticrossing plots in Figure 7.15(c-d).

The self-consistency of the fit was validated by confirming that the observed Rabi splittings at zero detuning for the A and B excitons matched the relations $\Omega_{R1} = \Omega_{R,\mathrm{A}} = 2(a_2 \cdot g_{\mathrm{A}}(f_m))$ and $\Omega_{R2} = \Omega_{R,\mathrm{B}} = 2(a_3 \cdot g_{\mathrm{B}}(f_m))$, ensuring the splittings were consistent with the scaled coupling strengths used in the Hamiltonian. The coupling strengths g_{A} and g_{B} follow the quadratic fits from the preceding subsection. As shown in Figure 7.15(a-b), these strengths exhibit a pronounced U-shaped dependence on f_m.

The resulting anticrossing plots, Figure 7.15(c-d), reveal three polariton branches: lower, middle, and upper, with the uncoupled A-exciton (red dashed line), uncoupled B-exciton (red solid line), and uncoupled MD/ED mode (black solid line) clearly separated from the fitted anticrossings (blue solid lines). Zero detuning for the A-exciton occurs at $f_m = 0.26$ (MD) and $f_m = 0.24$ (ED), and for the B-exciton at $f_m = 0.32$ (MD) and $f_m = 0.30$ (ED). The MD mode again shows stronger coupling particularly for B exciton interactions, with Rabi splittings of $\Omega_{R,\mathrm{A}} = 124$ meV and $\Omega_{R,\mathrm{B}} = 151$ meV, compared to $\Omega_{R,\mathrm{A}} = 132$ meV and $\Omega_{R,\mathrm{B}} = 136$ meV for the ED mode.

These results for the MD mode-exciton coupling in the prolate geometry are consistent with the findings in Chapter 6, confirming that it is stronger than ED mode-exciton coupling. Furthermore, they demonstrate that the prolate geometry outperforms the spherical geometry in self-hybridized systems. Finally, we conclude that it is possible to realize strongly coupled hyperbolic systems with self-hybridization based on combining TMDC materials with metallic layers while using a passive dielectric third layer to tune the exact properties.

Chapter 8

Conclusions

This dissertation has systematically investigated the optical properties and self-hybridized strong coupling phenomena in uniaxial hyperbolic multilayer nanospheroids. Through comprehensive numerical modeling using the T-matrix method and FDTD simulations, this work establishes a framework for understanding and designing these nanostructures for advanced polaritonic applications. The following conclusions synthesize key findings from each chapter, demonstrating the progression from fundamental mode characterization to successful demonstration of strong coupling with realistic materials.

Summary of Findings

Optical Modes of Hyperbolic Nanospheroids (Chapter 5)

The research foundation was established through detailed characterization of the rich optical modes in hyperbolic nanospheroids. These nanostructures support both plasmonic-like ED resonances and unique magnetic responses originating from the coupling of MD and EQ modes—a distinctive feature of hyperbolic dispersion where the perpendicular and parallel components of the permittivity tensor exhibit opposite signs.

- The MD-EQ mode exhibits a constant phase relationship under shape transformations, unlike the phase-reversing behavior observed in isotropic particles. This material-dependent mode shows high sensitivity to shape variations, demonstrating a pronounced redshift (approximately 2.6 times greater than the ED mode) when transitioning from prolate to oblate geometries.

- Optical response tuning is effectively achieved through the metal fill factor (f_m), which controls the hyperbolic dispersion range. Plasmonic ED modes blueshift with increasing f_m, while the MD-EQ mode displays a distinct crescent-shaped dependence, enabling independent control over mode positions through both material and geometric parameters.

- This chapter established the optical characteristics of prolate and spherical geometries compared to oblate configurations, such as enhanced field localization and stronger magnetic resonances, providing the foundation for subsequent strong coupling investigations.

Self-Hybridized Strong Coupling with Idealized Excitons (Chapter 6)

Building upon the fundamental understanding of optical modes, Chapter 6 demonstrated successful achievement of self-hybridized strong coupling through direct integration of excitonic resonances into the dielectric layers of hyperbolic nanospheroids.

- The MD mode consistently outperformed the ED mode, achieving strong coupling at significantly lower oscillator strengths ($f_{\mathrm{MD}}^{\mathrm{sc}} \approx 0.04$ for spheres, 0.03 for prolate) compared to the ED mode ($f_{\mathrm{ED}}^{\mathrm{sc}} \geq 0.36$ for spheres, ≥ 0.28 for prolate). This advantage originates from the MD mode's inherently narrower linewidth and predominantly absorptive character.

- Coupling strength for both modes followed the expected $\sqrt{f}$ dependence, with the MD mode exhibiting approximately 50% larger coupling strength. The system reached the ultra-strong coupling regime ($g > 10\%$ of the resonance energy) at remarkably low oscillator strengths for the MD mode ($f_{\mathrm{MD}}^{\mathrm{usc}} \approx 0.15$ for spheres, 0.22 for prolate).

- Practical implementation using multilayer nanodisks confirmed the robustness of these findings. The MD mode's coupling strength showed reduced sensitivity to size increases and varied monotonically with metal fill factor, peaking around $f_m \approx 0.7$. In contrast, ED coupling demonstrated greater volatility, peaking at $f_m \approx 0.3$ before decreasing. Prolate geometries consistently yielded stronger coupling than their spherical counterparts.

- The self-hybridized approach successfully validated the elimination of external cavity requirements through co-location of optical resonator and excitonic material, showcasing a versatile platform for compact polaritonic devices.

Strong Coupling with Realistic TMDC Excitons (Chapter 7)

The study was extended to realistic excitonic materials—transition metal dichalcogenides (TMDCs: MoS_2, WS_2, $MoSe_2$, WSe_2)—bridging the gap between idealized models and practical implementation.

- Initial two-layer structures (metal-TMDC) successfully demonstrated ED-exciton coupling but revealed an important limitation: no MD-exciton coupling was observed, regardless of geometry. This was the result of a very large red shift of both the ED and MD modes, well beyond the typical energies of excitons. This red shift could not be fully reversed by using prolate nanoparticles.

- Introduction of a three-layer design, incorporating a silica spacer between metal and TMDC layers, proved to be an effective approach. This modification enabled the first observation of strong MD-exciton coupling in specific prolate geometries and material compositions. The approach works due to a lowering of the dielectric permittivity that mixes with the metallic one and inhibits such a large red shift as above, while keeping the strong ecitonic transition of the TMDCs. Even this reduced amount of TMDC materials allows for observation of strong coupling.

- For prolate nanospheroids with fixed TMDC volume fraction (10%), strong MD-exciton coupling with clear anticrossing behavior was achieved for MoS_2 and WS_2. Coupling strength tuning via metal fill factor exhibited redshift for $f_m = 0.1$–0.5 and blueshift for $f_m = 0.52$–0.88.

- Quantitative analysis of prolate nanodisks confirmed MD mode dominance. For WS_2 (single exciton), the MD mode exhibited Rabi splitting of $\Omega_R = 186$ meV ($g = 93$ meV), outperforming the ED mode ($\Omega_R = 152$ meV). For MoS2 (dual excitons), the MD mode also showed stronger coupling to the B exciton ($\Omega R, B = 151$ meV) compared to the ED mode.

- This chapter conclusively demonstrated that while spherical geometries are limited to ED-exciton coupling, the prolate geometry is essential for achieving desired MD-exciton strong coupling in practical, multi-layered systems.

Summary

This research successfully demonstrates that uniaxial hyperbolic multilayer nanospheroids represent a highly versatile and powerful platform for achieving self-hybridized strong coupling. The work systematically reveals that optimal approach for efficient light-matter interaction in these systems requires synergy of three key design principles:

Material Composition: A metal fill factor (f_m) near 0.5–0.7 optimizes hyperbolic dispersion and maximizes MD coupling strength. Employing high-quality TMDCs as excitonic material is crucial for achieving strong coupling.

Particle Geometry: Prolate geometry demonstrates significant advantages over spherical and oblate shapes, providing stronger field localization, more robust MD resonances, and necessary conditions for MD-exciton interaction in practical multi-layered designs.

Structural Design: A three-layered architecture (metal/dielectric spacer/excitonic material) is essential for facilitating MD-exciton coupling, unattainable in simple two-layered structures.

Outlook and Future Perspectives

The findings of this work open several promising avenues for future research:

- **Experimental Realization:** The proposed multilayer nanodisks, particularly prolate Ag/Silica/WS_2 and Ag/Silica/MoS_2 systems, represent prime candidates for experimental validation using advanced nanofabrication techniques such as lithography and thin-film deposition.

- **Active Tunability:** Integration of actively tunable materials (e.g., using electrostatic gating on TMDCs or phase-change materials) could enable dynamic control of coupling strength *in situ* post-fabrication.

- **Quantum and Nonlinear Optics:** These efficient MD-based polaritonic systems could serve as platforms for exploring quantum correlations, polariton lasing, or enhanced nonlinear optical effects within deeply subwavelength volumes.

- **Extended Material Platforms:** The established design principles could be applied to other emerging excitonic and anisotropic materials, including perovskites, black phosphorus, or other van der Waals heterostructures.

- **Device Integration:** Future work should explore integration of these optimized nanostructures into functional devices for applications in quantum information processing, sensing, and low-energy optoelectronics.

Chapter 9

Appendix A

This appendix is adapted from [123]

9.1. Multipole Decompostion in Cartesian Coordinates

This appendix provides the key mathematical expressions for multipole decomposition used in this dissertation. The detailed derivations follow the theoretical framework developed by Alaee et al. [123].

Notation and Symbols

The following symbols are used throughout this appendix:

- ω - angular frequency of the electromagnetic field
- $k = \omega/c$ - wavenumber, where c is the speed of light in vacuum
- ε_0 - permittivity of free space
- ε_r - relative permittivity of the material
- $j_\ell(kr)$ - spherical Bessel functions of order ℓ
- r_{-1}, r_0, r_1 - spherical tensor components of position vector $\mathbf{r}$
- $J^\omega_{-1}, J^\omega_0, J^\omega_1$ - spherical tensor components of current density $\mathbf{J}^\omega$
- $\alpha, \beta = x, y, z$ - Cartesian coordinate indices
- $\delta_{\alpha\beta}$ - Kronecker delta function

9.1.1. Current Density Conversion

The induced electric current density is obtained from the electric field distribution as:

$$\mathbf{J}^\omega(\mathbf{r}) = i\omega\varepsilon_0(\varepsilon_r - 1)\mathbf{E}^\omega(\mathbf{r}) \tag{9.1}$$

9.1.2. Coordinate System Relations

The transformation between spherical and Cartesian coordinates for position and current density components are given by:

Position Coordinates

$$x = \frac{1}{\sqrt{2}}(r_{-1} - r_1) \tag{9.2}$$

$$y = \frac{1}{\sqrt{2}i}(r_{-1} + r_1) \tag{9.3}$$

$$z = r_0 \tag{9.4}$$

Current Density Components

$$J_x^\omega = \frac{1}{\sqrt{2}}(J_{-1}^\omega - J_1^\omega) \tag{9.5}$$

$$J_y^\omega = \frac{1}{\sqrt{2}i}(J_{-1}^\omega + J_1^\omega) \tag{9.6}$$

$$J_z^\omega = J_0^\omega \tag{9.7}$$

Cross Product Relations

The cross product components in Cartesian coordinates are:

$$(\mathbf{r} \times \mathbf{J}^\omega)_x = yJ_z^\omega - zJ_y^\omega \tag{9.8}$$

$$(\mathbf{r} \times \mathbf{J}^\omega)_y = zJ_x^\omega - xJ_z^\omega \tag{9.9}$$

$$(\mathbf{r} \times \mathbf{J}^\omega)_z = xJ_y^\omega - yJ_x^\omega \tag{9.10}$$

9.1.3. Exact Multipole Expressions

The exact expressions for multipole moments in Cartesian coordinates, derived from spherical multipole theory [123], are:

Electric Dipole Moment

$$p_\alpha^\omega = -\frac{1}{i\omega}\int d^3\mathbf{r} J_\alpha^\omega j_0(kr) + \frac{k^2}{2}\int d^3\mathbf{r}\left[3(\mathbf{r}\cdot\mathbf{J}^\omega)r_\alpha - r^2 J_\alpha^\omega\right]\frac{j_2(kr)}{(kr)^2} \tag{9.11}$$

where $\alpha = x, y, z$, $k = \omega/c$ is the wavenumber, and $j_\ell(kr)$ are spherical Bessel functions.

Magnetic Dipole Moment

$$m_\alpha^\omega = \frac{3}{2}\int d^3\mathbf{r}(\mathbf{r}\times\mathbf{J}^\omega)_\alpha \frac{j_1(kr)}{kr} \tag{9.12}$$

Electric Quadrupole Moment

The electric quadrupole moment has contributions from two different multipolar orders ($\ell = 1$ and $\ell = 3$):

$$\begin{aligned} Q_{\alpha\beta}^e = &-\frac{3}{i\omega}\int d^3\mathbf{r}\left[3(r_\beta J_\alpha^\omega + r_\alpha J_\beta^\omega) - 2(\mathbf{r}\cdot\mathbf{J}^\omega)\delta_{\alpha\beta}\right]\frac{j_1(kr)}{kr} \\ &+ 2k^2\int d^3\mathbf{r}\left[5r_\alpha r_\beta(\mathbf{r}\cdot\mathbf{J}^\omega) - (r_\alpha J_\beta^\omega + r_\beta J_\alpha^\omega)r^2 - r^2(\mathbf{r}\cdot\mathbf{J}^\omega)\delta_{\alpha\beta}\right]\frac{j_3(kr)}{(kr)^3} \end{aligned} \tag{9.13}$$

where $\delta_{\alpha\beta}$ is the Kronecker delta.

Magnetic Quadrupole Moment

$$Q^m_{\alpha\beta} = 15 \int d^3\mathbf{r}\, [r_\alpha (\mathbf{r} \times \mathbf{J}^\omega)_\beta + r_\beta (\mathbf{r} \times \mathbf{J}^\omega)_\alpha] \frac{j_2(kr)}{(kr)^2} \tag{9.14}$$

9.1.4. Long-Wavelength Approximations

For nanostructures small compared to the wavelength ($kr \ll 1$), the spherical Bessel functions can be approximated, yielding:

Spherical Bessel Function Expansions

$$j_0(kr) \approx 1 - \frac{(kr)^2}{6} + O((kr)^4) \tag{9.15}$$

$$j_1(kr) \approx \frac{kr}{3} - \frac{(kr)^3}{30} + O((kr)^5) \tag{9.16}$$

$$j_2(kr) \approx \frac{(kr)^2}{15} - \frac{(kr)^4}{210} + O((kr)^6) \tag{9.17}$$

$$j_3(kr) \approx \frac{(kr)^3}{105} + O((kr)^5) \tag{9.18}$$

Long-Wavelength Multipole Expressions

Electric Dipole:

$$p_\alpha \approx -\frac{1}{i\omega} \int d^3\mathbf{r} J^\omega_\alpha + \frac{k^2}{10} \int d^3\mathbf{r} \left[(\mathbf{r} \cdot \mathbf{J}^\omega) r_\alpha - 2r^2 J^\omega_\alpha \right] \tag{9.19}$$

The first term represents the conventional electric dipole moment, while the second term corresponds to the toroidal dipole contribution.

Magnetic Dipole:

$$m^\omega_\alpha \approx \frac{1}{2} \int d^3\mathbf{r} (\mathbf{r} \times \mathbf{J}^\omega)_\alpha \tag{9.20}$$

This is the conventional magnetic dipole moment.

Electric Quadrupole:

$$\begin{aligned} Q^e_{\alpha\beta} \approx & -\frac{1}{i\omega} \int d^3\mathbf{r} \left[3(r_\beta J^\omega_\alpha + r_\alpha J^\omega_\beta) - 2(\mathbf{r} \cdot \mathbf{J}^\omega)\delta_{\alpha\beta} \right] \\ & + \frac{k^2}{14} \int d^3\mathbf{r} \left[4r_\alpha r_\beta (\mathbf{r} \cdot \mathbf{J}^\omega) - 5r^2 (r_\alpha J^\omega_\beta + r_\beta J^\omega_\alpha) + 2r^2 (\mathbf{r} \cdot \mathbf{J}^\omega)\delta_{\alpha\beta} \right] \end{aligned} \tag{9.21}$$

The first term is the conventional electric quadrupole moment, while the second term represents the toroidal quadrupole contribution.

Magnetic Quadrupole:

$$Q^m_{\alpha\beta} \approx \int d^3\mathbf{r}\, [r_\alpha (\mathbf{r} \times \mathbf{J}^\omega)_\beta + r_\beta (\mathbf{r} \times \mathbf{J}^\omega)_\alpha] \tag{9.22}$$

This is the conventional magnetic quadrupole moment.

9.1.5. Physical Interpretation

The long-wavelength approximations reveal that electric multipole moments contain both conventional and toroidal contributions. The toroidal terms, which are often misidentified as a separate family of multipoles, are actually higher-order corrections that become significant beyond the long-wavelength limit. In contrast, magnetic multipole moments retain their conventional forms under the exact formulation.

For detailed step-by-step derivations of these expressions, including the spherical-to-Cartesian transformations and algebraic manipulations, see the supplemental material of Alaee et al. [123].

Chapter 10

Appendix B

This appendix is adapted from [126, 127]

10.1. Vector Quasi-Spherical Wave Functions for Anisotropic Media

For electromagnetic wave propagation in uniaxial anisotropic media, the conventional vector spherical wave functions must be generalized to vector quasi-spherical wave functions (VQSWFs). The electromagnetic fields can be expressed as integrals over plane waves, and for each plane wave, the Maxwell equations yield specific dispersion relations [126].

Symbol Definitions and Notation

The following symbols are used throughout this appendix:

- ω - angular frequency; c - speed of light in vacuum
- $k_0 = \omega/c$ - free space wavenumber
- $k_s = k_0\sqrt{\varepsilon_s\mu_s}$ - wavenumber in exterior medium
- $k_i = k_0\sqrt{\varepsilon_i\mu_i}$ - wavenumber for ordinary wave in interior
- ε_s, μ_s - relative permittivity and permeability of surrounding medium
- $\varepsilon_i, \mu_i, \varepsilon_{iz}$ - permittivity components and permeability of interior medium
- D_i, D_s - interior and exterior domains; S - boundary surface
- $\mathbf{n}$ - outward unit normal vector on surface S
- (r, θ, ϕ) - spherical coordinates with unit vectors $(\mathbf{e}_r, \mathbf{e}_\theta, \mathbf{e}_\phi)$
- (k, β, α) - wave vector spherical coordinates with unit vectors $(\mathbf{e}_k, \mathbf{e}_\beta, \mathbf{e}_\alpha)$
- ν, μ - composite indices representing pairs (m, n) and (m', n') respectively
- $m_{rz} = \sqrt{\varepsilon_{iz}/\varepsilon_s}$ - relative anisotropy parameter
- $g(k_s, \mathbf{r}, \mathbf{r}') = \frac{e^{jk_s|\mathbf{r}-\mathbf{r}'|}}{4\pi|\mathbf{r}-\mathbf{r}'|}$ - Green's function

- $\pi_n^{|m|}(\beta) = \frac{mP_n^{|m|}(\cos\beta)}{\sin\beta}$, $\tau_n^{|m|}(\beta) = \frac{dP_n^{|m|}(\cos\beta)}{d\beta}$ - angular functions
- $P_n^{|m|}(\cos\beta)$ - associated Legendre polynomials
- $\lambda_{k\beta}(\beta) = \left(\frac{1}{\varepsilon_i} - \frac{1}{\varepsilon_{iz}}\right)\sin\beta\cos\beta$
- $\lambda_{\beta\beta}(\beta) = \frac{1}{\varepsilon_i}\cos^2\beta + \frac{1}{\varepsilon_{iz}}\sin^2\beta$
- $\mathbf{M}_\nu^3, \mathbf{N}_\nu^3$ - outgoing vector spherical wave functions where $\nu \equiv (m, n)$

10.1.1. Maxwell Equations in Anisotropic Media

For a uniaxial anisotropic medium with permittivity tensor:

$$\boldsymbol{\varepsilon}_i = \begin{pmatrix} \varepsilon_i & 0 & 0 \\ 0 & \varepsilon_i & 0 \\ 0 & 0 & \varepsilon_{iz} \end{pmatrix} \tag{10.1}$$

The Maxwell equations are:

$$\nabla \times \mathbf{E}_i = jk_0\mathbf{B}_i, \quad \nabla \times \mathbf{H}_i = -jk_0\mathbf{D}_i \tag{10.2}$$

$$\nabla \cdot \mathbf{B}_i = 0, \quad \nabla \cdot \mathbf{D}_i = 0 \tag{10.3}$$

with constitutive relations:

$$\mathbf{D}_i = \boldsymbol{\varepsilon}_i\mathbf{E}_i, \quad \mathbf{B}_i = \mu_i\mathbf{H}_i \tag{10.4}$$

10.1.2. Plane Wave Analysis and Dispersion Relations

Using Fourier transform techniques, the electromagnetic fields can be expressed as integrals over plane waves:

$$\mathbf{A}(\mathbf{r}) = \int \tilde{\mathbf{A}}(\mathbf{k})e^{j\mathbf{k}\cdot\mathbf{r}}d^3\mathbf{k} \tag{10.5}$$

For each plane wave with wave vector $\mathbf{k}$, the Maxwell equations in Fourier space become:

$$\mathbf{k} \times \tilde{\mathbf{E}} = k_0\tilde{\mathbf{B}} \tag{10.6}$$

$$\mathbf{k} \times \tilde{\mathbf{H}} = -k_0\tilde{\mathbf{D}} \tag{10.7}$$

$$\mathbf{k} \cdot \tilde{\mathbf{D}} = 0, \quad \mathbf{k} \cdot \tilde{\mathbf{B}} = 0 \tag{10.8}$$

In spherical coordinates (k, β, α) for the wave vector, the analysis yields two characteristic waves:

Ordinary wave:

$$k_1^2 = k_0^2\varepsilon_i\mu_i \tag{10.9}$$

Extraordinary wave:

$$k_2^2 = k_0^2\frac{\varepsilon_i\mu_i}{\cos^2\beta + \frac{\varepsilon_i}{\varepsilon_{iz}}\sin^2\beta} \tag{10.10}$$

10.1.3. Vector Quasi-Spherical Wave Functions

The VQSWFs are defined through integral representations over the unit sphere as given in [126]:

$$\mathbf{X}^e_{mn}(\mathbf{r}) = -\frac{1}{4\pi j^{n+1}}\frac{1}{\sqrt{2n(n+1)}}\int_0^{2\pi}\int_0^{\pi}\Big[j\tau_n^{|m|}(\beta)e^{jk_1(\beta,\alpha)\cdot\mathbf{r}}\mathbf{e}_\alpha + \varepsilon[\lambda_{k\beta}(\beta)\mathbf{e}_k + \lambda_{\beta\beta}(\beta)\mathbf{e}_\beta]m\pi_n^{|m|}(\beta)e^{jk_2(\beta,\alpha)\cdot\mathbf{r}}\Big]e^{jm\alpha}\sin\beta\,d\beta\,d\alpha \tag{10.11}$$

$$\mathbf{Y}^e_{mn}(\mathbf{r}) = -\frac{1}{4\pi j^{n+1}}\frac{1}{\sqrt{2n(n+1)}}\int_0^{2\pi}\int_0^{\pi}\Big[jm\pi_n^{|m|}(\beta)e^{jk_1(\beta,\alpha)\cdot\mathbf{r}}\mathbf{e}_\alpha + \varepsilon[\lambda_{k\beta}(\beta)\mathbf{e}_k + \lambda_{\beta\beta}(\beta)\mathbf{e}_\beta]\tau_n^{|m|}(\beta)e^{jk_2(\beta,\alpha)\cdot\mathbf{r}}\Big]e^{jm\alpha}\sin\beta\,d\beta\,d\alpha \tag{10.12}$$

$$\mathbf{X}^h_{mn}(\mathbf{r}) = -\frac{1}{4\pi j^{n+1}}\frac{1}{\sqrt{2n(n+1)}}\int_0^{2\pi}\int_0^{\pi}\Big[\tau_n^{|m|}(\beta)e^{jk_1(\beta,\alpha)\cdot\mathbf{r}}\mathbf{e}_\beta + j\sqrt{\varepsilon\lambda_{\beta\beta}(\beta)}m\pi_n^{|m|}(\beta)e^{jk_2(\beta,\alpha)\cdot\mathbf{r}}\mathbf{e}_\alpha\Big]e^{jm\alpha}\sin\beta\,d\beta\,d\alpha \tag{10.13}$$

$$\mathbf{Y}^h_{mn}(\mathbf{r}) = -\frac{1}{4\pi j^{n+1}}\frac{1}{\sqrt{2n(n+1)}}\int_0^{2\pi}\int_0^{\pi}\Big[m\pi_n^{|m|}(\beta)e^{jk_1(\beta,\alpha)\cdot\mathbf{r}}\mathbf{e}_\beta + j\sqrt{\varepsilon\lambda_{\beta\beta}(\beta)}\tau_n^{|m|}(\beta)e^{jk_2(\beta,\alpha)\cdot\mathbf{r}}\mathbf{e}_\alpha\Big]e^{jm\alpha}\sin\beta\,d\beta\,d\alpha \tag{10.14}$$

where $\pi_n^{|m|}(\beta)$ and $\tau_n^{|m|}(\beta)$ are angular functions related to associated Legendre polynomials, and $\lambda_{k\beta}(\beta)$, $\lambda_{\beta\beta}(\beta)$ are functions derived from the anisotropic material properties.

10.2. Null-Field Method for Anisotropic Particles

10.2.1. General Null-Field Equation

The null-field method for anisotropic particles [126, 127] starts with the general null-field equation for the exterior domain:

$$\mathbf{E}^e(\mathbf{r}) + \nabla\times\int_S \mathbf{e}_i(\mathbf{r}')g(k_s,\mathbf{r},\mathbf{r}')dS(\mathbf{r}') + \frac{j}{k_0\varepsilon_s}\nabla\times\nabla\times\int_S \mathbf{h}_i(\mathbf{r}')g(k_s,\mathbf{r},\mathbf{r}')dS(\mathbf{r}') = \mathbf{0} \tag{10.15}$$

for $\mathbf{r}\in D_i$, where $\mathbf{e}_i = \mathbf{n}\times\mathbf{E}_i$ and $\mathbf{h}_i = \mathbf{n}\times\mathbf{H}_i$ are the surface fields.

10.2.2. Expansion in Vector Spherical Wave Functions

Following the standard procedure:

1. Restrict $\mathbf{r}$ to lie on a spherical surface enclosed in D_i
2. Expand the incident field and the dyad $g(\mathbf{r},\mathbf{r}')\mathbf{I}$ in terms of regular vector spherical wave functions
3. Use orthogonality of vector spherical wave functions on spherical surfaces

This yields the matrix form:

$$\frac{jk_s^2}{\pi}\int_S\left[\mathbf{e}_i(\mathbf{r}')\cdot\begin{pmatrix}\mathbf{N}_\nu^3(k_s\mathbf{r}')\\ \mathbf{M}_\nu^3(k_s\mathbf{r}')\end{pmatrix}+j\sqrt{\frac{\mu_s}{\varepsilon_s}}\mathbf{h}_i(\mathbf{r}')\cdot\begin{pmatrix}\mathbf{M}_\nu^3(k_s\mathbf{r}')\\ \mathbf{N}_\nu^3(k_s\mathbf{r}')\end{pmatrix}\right]dS(\mathbf{r}')=-\begin{pmatrix}a_\nu\\ b_\nu\end{pmatrix} \tag{10.16}$$

10.2.3. Surface Field Expansion for Anisotropic Media

For anisotropic particles, the surface fields are expanded using VQSWFs:

$$\begin{aligned}\begin{pmatrix}\mathbf{e}_i^N(\mathbf{r}')\\ \mathbf{h}_i^N(\mathbf{r}')\end{pmatrix}=&\sum_{\mu=1}^{N}c_\mu^N\begin{pmatrix}\mathbf{n}(\mathbf{r}')\times\mathbf{X}_\mu^e(\mathbf{r}')\\ -j\sqrt{\frac{\varepsilon_i}{\mu_i}}\mathbf{n}(\mathbf{r}')\times\mathbf{X}_\mu^h(\mathbf{r}')\end{pmatrix}\\&+d_\mu^N\begin{pmatrix}\mathbf{n}(\mathbf{r}')\times\mathbf{Y}_\mu^e(\mathbf{r}')\\ -j\sqrt{\frac{\varepsilon_i}{\mu_i}}\mathbf{n}(\mathbf{r}')\times\mathbf{Y}_\mu^h(\mathbf{r}')\end{pmatrix}\end{aligned} \tag{10.17}$$

10.3. Derivation of Matrix Elements

10.3.1. Substitution and Coefficient Separation

Substituting the anisotropic surface field expansion into the null-field equation, contributions from c_μ^N and d_μ^N coefficients are separated.

For c_μ^N coefficients (X-type functions):

$$\begin{aligned}\frac{jk_s^2}{\pi}\int_S\Bigg[&(\mathbf{n}\times\mathbf{X}_\mu^e)\cdot\begin{pmatrix}\mathbf{N}_\nu^3\\ \mathbf{M}_\nu^3\end{pmatrix}\\&+j\sqrt{\frac{\mu_s}{\varepsilon_s}}\left(-j\sqrt{\frac{\varepsilon_i}{\mu_i}}\mathbf{n}\times\mathbf{X}_\mu^h\right)\cdot\begin{pmatrix}\mathbf{M}_\nu^3\\ \mathbf{N}_\nu^3\end{pmatrix}\Bigg]dS\end{aligned} \tag{10.18}$$

The magnetic field coupling term simplifies as:

$$j\sqrt{\frac{\mu_s}{\varepsilon_s}}\left(-j\sqrt{\frac{\varepsilon_i}{\mu_i}}\right)=j\cdot(-j)\sqrt{\frac{\mu_s\varepsilon_i}{\varepsilon_s\mu_i}}=\sqrt{\frac{\mu_s\varepsilon_i}{\varepsilon_s\mu_i}} \tag{10.19}$$

For nonmagnetic media ($\mu_s=\mu_i=1$):

$$\sqrt{\frac{\mu_s\varepsilon_i}{\varepsilon_s\mu_i}}=\sqrt{\frac{\varepsilon_i}{\varepsilon_s}} \tag{10.20}$$

10.3.2. Final Matrix Elements

The matrix $\mathbf{Q}^{31}_{\text{anis}}$ has the block structure:

$$\mathbf{Q}^{31}_{\text{anis}} = \begin{pmatrix} (\mathbf{Q}^{31}_{\text{anis}})^{11} & (\mathbf{Q}^{31}_{\text{anis}})^{12} \\ (\mathbf{Q}^{31}_{\text{anis}})^{21} & (\mathbf{Q}^{31}_{\text{anis}})^{22} \end{pmatrix} \tag{10.21}$$

From the first component ($\mathbf{N}^3_\nu$ term) with c^N_μ coefficients:

$$\boxed{(\mathbf{Q}^{31}_{\text{anis}})^{11}_{\nu\mu} = \frac{jk_s^2}{\pi} \int_S \left[(\mathbf{n} \times \mathbf{X}^e_\mu) \cdot \mathbf{N}^3_\nu + \sqrt{\frac{\varepsilon_i}{\varepsilon_s}} (\mathbf{n} \times \mathbf{X}^h_\mu) \cdot \mathbf{M}^3_\nu \right] dS} \tag{10.22}$$

From the first component ($\mathbf{N}^3_\nu$ term) with d^N_μ coefficients:

$$\boxed{(\mathbf{Q}^{31}_{\text{anis}})^{12}_{\nu\mu} = \frac{jk_s^2}{\pi} \int_S \left[(\mathbf{n} \times \mathbf{Y}^e_\mu) \cdot \mathbf{N}^3_\nu + \sqrt{\frac{\varepsilon_i}{\varepsilon_s}} (\mathbf{n} \times \mathbf{Y}^h_\mu) \cdot \mathbf{M}^3_\nu \right] dS} \tag{10.23}$$

From the second component ($\mathbf{M}^3_\nu$ term) with c^N_μ coefficients:

$$\boxed{(\mathbf{Q}^{31}_{\text{anis}})^{21}_{\nu\mu} = \frac{jk_s^2}{\pi} \int_S \left[(\mathbf{n} \times \mathbf{X}^e_\mu) \cdot \mathbf{M}^3_\nu + \sqrt{\frac{\varepsilon_i}{\varepsilon_s}} (\mathbf{n} \times \mathbf{X}^h_\mu) \cdot \mathbf{N}^3_\nu \right] dS} \tag{10.24}$$

From the second component ($\mathbf{M}^3_\nu$ term) with d^N_μ coefficients:

$$\boxed{(\mathbf{Q}^{31}_{\text{anis}})^{22}_{\nu\mu} = \frac{jk_s^2}{\pi} \int_S \left[(\mathbf{n} \times \mathbf{Y}^e_\mu) \cdot \mathbf{M}^3_\nu + \sqrt{\frac{\varepsilon_i}{\varepsilon_s}} (\mathbf{n} \times \mathbf{Y}^h_\mu) \cdot \mathbf{N}^3_\nu \right] dS} \tag{10.25}$$

10.4. Physical Interpretation

The derived matrix elements represent the coupling between the vector quasi-spherical wave functions inside the anisotropic particle and the regular vector spherical wave functions in the exterior isotropic medium. The factor $\sqrt{\frac{\varepsilon_i}{\varepsilon_s}}$ reflects the anisotropic nature of the particle and accounts for the modified electromagnetic boundary conditions.

In the isotropic limit ($\varepsilon_{iz} = \varepsilon_i$), the VQSWFs reduce to conventional VSWFs, and the factor $\sqrt{\frac{\varepsilon_i}{\varepsilon_s}}$ becomes the standard relative permittivity ratio, recovering the isotropic T-matrix formulation.

The complete T-matrix for the anisotropic particle is obtained as:

$$\mathbf{T}_{\text{anis}} = -\mathbf{Q}^{11}_{\text{anis}}(k_s, k_i, m_{rz}) \left[\mathbf{Q}^{31}_{\text{anis}}(k_s, k_i, m_{rz}) \right]^{-1} \tag{10.26}$$

where $m_{rz} = \sqrt{\varepsilon_{iz}/\varepsilon_s}$ characterizes the degree of anisotropy.

Chapter 11

Appendix C

11.1. Vector Spherical Wave Functions

Symbol Definitions and Notation

The following symbols are used throughout this appendix:

- $\mathbf{r} = (x, y, z)$ - position vector in Cartesian coordinates
- $\mathbf{r} = (r, \theta, \phi)$ - position vector in spherical coordinates
- $r = |\mathbf{r}|$ - radial distance from the origin
- θ - polar angle (measured from the positive z-axis), $0 \leq \theta \leq \pi$
- ϕ - azimuthal angle (measured from the positive x-axis), $0 \leq \phi < 2\pi$
- k - wavenumber in the surrounding medium
- $\hat{\mathbf{e}}_r$ - radial unit vector pointing outward from the origin
- $\hat{\boldsymbol{\theta}}$ - polar unit vector pointing in the direction of increasing θ
- $\hat{\boldsymbol{\phi}}$ - azimuthal unit vector pointing in the direction of increasing ϕ
- l - multipole order (positive integer), $l = 1, 2, 3, \ldots$
- m - degree (integer), $-l \leq m \leq l$
- $P_l^m(\cos\theta)$ - associated Legendre polynomial of degree l and order m
- $z_l^1(kr) = j_l(kr)$ - spherical Bessel function of the first kind
- $z_l^3(kr) = h_l^{(1)}(kr)$ - spherical Hankel function of the first kind
- $Y_l^m(\theta, \phi)$ - scalar spherical harmonic
- $\mathbf{m}_l^m(\theta, \phi)$, $\mathbf{n}_l^m(\theta, \phi)$ - vector spherical harmonics
- c_l^m - normalization constant for spherical harmonics
- $\nabla\times$ - curl operator in vector calculus
- $[f(kr)]' = \frac{d}{d(kr)}[f(kr)]$ - derivative with respect to the argument kr

- $\delta_{ll'}$ - Kronecker delta function: $\delta_{ll'} = 1$ if $l = l'$, and $\delta_{ll'} = 0$ if $l \neq l'$
- $\mathbf{a} \cdot \mathbf{b}$ - dot product of vectors $\mathbf{a}$ and $\mathbf{b}$
- $\mathbf{a}^*$ - complex conjugate of vector $\mathbf{a}$

Here, the formulation used by Amos [161], Wriedt, and Doicu [126]. The electric and magnetic fields are expanded into VSWFs, which are classified as either regular (denoted with the superscript 1) or radiating (denoted with the superscript 3) and defined as:

$$\mathbf{M}_l^{m1}(k\mathbf{r}) = z_l^1(kr)\mathbf{m}_l^m(\theta,\phi), \tag{11.1}$$

$$\mathbf{N}_l^{m1}(k\mathbf{r}) = \sqrt{\frac{l(l+1)}{2}}\left[\frac{z_l^1(kr)}{kr}Y_l^m(\theta,\phi)\hat{\mathbf{e}}_r + \frac{[krz_l^1(kr)]'}{kr}\mathbf{n}_l^m(\theta,\phi)\right], \tag{11.2}$$

$$\mathbf{M}_l^{m3}(k\mathbf{r}) = z_l^3(kr)\mathbf{m}_l^m(\theta,\phi), \tag{11.3}$$

$$\mathbf{N}_l^{m3}(k\mathbf{r}) = \sqrt{\frac{l(l+1)}{2}}\left[\frac{z_l^3(kr)}{kr}Y_l^m(\theta,\phi)\hat{\mathbf{e}}_r + \frac{[krz_l^3(kr)]'}{kr}\mathbf{n}_l^m(\theta,\phi)\right]. \tag{11.4}$$

Here, $z_l^1(kr)$ represents the spherical Bessel function, and $z_l^3(kr)$ represents the spherical Hankel function. The scalar spherical harmonic $Y_l^m(\theta,\phi)$ is a function of the angular coordinates θ and ϕ, while $\mathbf{m}_l^m$ and $\mathbf{n}_l^m$ are the vector spherical harmonics (VSHs) that define the angular dependence of the fields.

The vector spherical harmonics $\mathbf{m}_l^m(\theta,\phi)$ and $\mathbf{n}_l^m(\theta,\phi)$ are expressed as:

$$\mathbf{m}_l^m(\theta,\phi) = c_l^m\sqrt{\frac{2l(l+1)}{2}}\left[i\frac{m}{\sin\theta}P_l^m(\cos\theta)\hat{\boldsymbol{\theta}} - \frac{dP_l^m(\cos\theta)}{d\theta}\hat{\boldsymbol{\phi}}\right]e^{im\phi}, \tag{11.5}$$

$$\mathbf{n}_l^m(\theta,\phi) = c_l^m\sqrt{\frac{2l(l+1)}{2}}\left[\frac{dP_l^m(\cos\theta)}{d\theta}\hat{\boldsymbol{\theta}} + i\frac{m}{\sin\theta}P_l^m(\cos\theta)\hat{\boldsymbol{\phi}}\right]e^{im\phi}. \tag{11.6}$$

In these expressions, $P_l^m(\cos\theta)$ is the associated Legendre polynomial, which describes the angular dependency. The normalization constant c_l^m ensures orthonormality and is defined as:

$$c_l^m = \sqrt{\frac{(2l+1)}{4\pi}\frac{(l-m)!}{(l+m)!}}. \tag{11.7}$$

The scalar spherical harmonic $Y_l^m(\theta,\phi)$, used in the radial component of $\mathbf{N}_l^m$, is defined as:

$$Y_l^m(\theta,\phi) = c_l^m P_l^m(\cos\theta)e^{im\phi}. \tag{11.8}$$

The vector spherical wave functions $\mathbf{N}_l^m$ and $\mathbf{M}_l^m$ are mathematically related through the curl operation:

$$\mathbf{N}_l^{m1}(k\mathbf{r}) = \frac{1}{k}\nabla\times\mathbf{M}_l^{m1}(k\mathbf{r}), \tag{11.9}$$

$$\mathbf{N}_l^{m3}(k\mathbf{r}) = \frac{1}{k}\nabla\times\mathbf{M}_l^{m3}(k\mathbf{r}). \tag{11.10}$$

These relationships illustrate that the magnetic-type wave functions are derived directly from the electric-type wave functions via a curl operation.

The orthogonality of the vector spherical harmonics is a crucial property that simplifies mathematical operations in the T-matrix method. The orthogonality relations are given by:

$$\int_0^{2\pi}\int_0^{\pi} \mathbf{m}_l^m(\theta,\phi)\cdot\mathbf{m}_{l'}^{m'*}(\theta,\phi)\sin\theta\,d\theta\,d\phi = \pi\delta_{ll'}\delta_{mm'}, \tag{11.11}$$

$$\int_0^{2\pi}\int_0^{\pi} \mathbf{n}_l^m(\theta,\phi)\cdot\mathbf{n}_{l'}^{m'*}(\theta,\phi)\sin\theta\,d\theta\,d\phi = \pi\delta_{ll'}\delta_{mm'}, \tag{11.12}$$

$$\int_0^{2\pi}\int_0^{\pi} \mathbf{m}_l^m(\theta,\phi)\cdot\mathbf{n}_{l'}^{m'*}(\theta,\phi)\sin\theta\,d\theta\,d\phi = 0. \tag{11.13}$$

These orthogonality properties ensure that vector spherical harmonics of different orders (l) or degrees (m) are mutually independent, making them an efficient basis for expanding electromagnetic fields.

Bibliography

[1] N. Rivera and I. Kaminer. Light–matter interactions with photonic quasiparticles. *Nature Reviews Physics*, 2(10):538–561, 2020.

[2] J. T. Hugall, A. Singh, and N. F. van Hulst. Plasmonic cavity coupling. *ACS Photonics*, 5(1):43–53, 2018.

[3] P. Vasa and C. Lienau. Strong light-matter interaction in quantum emitter/metal hybrid nanostructures. *ACS Photonics*, 5(1):2–23, 2018.

[4] D. G. Baranov, M. Wersäll, J. Cuadra, T. J. Antosiewicz, and T. Shegai. Novel nanostructures and materials for strong light-matter interactions. *ACS Photonics*, 5(1):24–42, 2018.

[5] F. Marquier, C. Sauvan, and J. J. Greffet. Revisiting quantum optics with surface plasmons and plasmonic resonators. *ACS Photonics*, 4(9):2091–2101, 2017.

[6] Francesco Pisani, Djamal Gacemi, Angela Vasanelli, Lianhe Li, Alexander Giles Davies, Edmind Linfield, Carlo Sirtori, and Yanko Todorov. Electronic transport driven by collective light-matter coupled states in a quantum device. *Nat. Commun.*, 14:3914, 2023.

[7] Darius Urbonas, Antti J. Moilanen, Kristin B. Arnardottir, Ullrich Scherf, Rainer F. Mahrt, Päivi Törmä, and Thilo Stöferle. Temporal mode switching during polariton condensation. *Commun. Phys.*, 7:203, 2024.

[8] Battulga Munkhbat, Martin Wersäll, Denis G. Baranov, Tomasz J. Antosiewicz, and Timur Shegai. Suppression of photo-oxidation of organic chromophores by strong coupling to plasmonic nanoantennas. *Sci. Adv.*, 4(7):eaas9552, 2018.

[9] Wonmi Ahn, Johan F. Triana, Felipe Recabal, Felipe Herrera, and Blake S. Simpkins. Modification of ground-state chemical reactivity via light–matter coherence in infrared cavities. *Science*, 380(6650):1165–1168, 2023.

[10] Adriana Canales, Denis G. Baranov, Tomasz J. Antosiewicz, and Timur Shegai. Abundance of cavity-free polaritonic states in resonant materials and nanostructures. *Journal of Chemical Physics*, 154(2):024701, 01 2021.

[11] B. Munkhbat, D. G. Baranov, M. Stührenberg, M. Wersäll, A. Bisht, and T. Shegai. Self-hybridized exciton-polaritons in multilayers of transition metal dichalcogenides for efficient light absorption. *ACS Photonics*, 6(1):139–147, 2019.

[12] L. Li, W. Li, X. Zong, and Y. Liu. Self-hybridized exciton-polaritons in perovskite-based subwavelength photonic crystals. *New Journal of Physics*, 24(8), 2022.

[13] Z. Tahir, J. W. Jung, M. Ur Rashid, S. Kim, D. K. Dang, J. W. Kang, C. H. Cho, J. I. Jang, and Y. S. Kim. Strong exciton-photon coupling in self-hybridized organic-inorganic lead halide perovskite microcavities. *Nanophotonics*, 12(23):4297–4306, 2023.

[14] S. B. Anantharaman, C. E. Stevens, J. Lynch, B. Song, J. Hou, H. Zhang, K. Jo, P. Kumar, J. C. Blancon, A. D. Mohite, J. R. Hendrickson, and D. Jariwala. Self-hybridized polaritonic emission from layered perovskites. *Nano Letters*, 21(14):6245–6252, 2021.

[15] A. T. Nguyen, S. Kwon, J. Song, E. Cho, H. Kim, and D. W. Kim. Self-hybridized exciton-polaritons in sub-10-nm-thick ws_2 flakes: Roles of optical phase shifts at ws_2/au interfaces. *Nanomaterials*, 12(14), 2022.

[16] S. B. Anantharaman, J. Lynch, C. E. Stevens, C. Munley, C. Li, J. Hou, H. Zhang, A. Torma, T. Darlington, F. Coen, K. Li, A. Majumdar, P. J. Schuck, A. Mohite, H. Harutyunyan, J. R. Hendrickson, and D. Jariwala. Dynamics of self-hybridized exciton–polaritons in 2d halide perovskites. *Light: Science and Applications*, 13(1), 2024.

[17] M. Black, M. Asadi, P. Darman, S. Seçkin, F. Schillmöller, T. A. F. König, S. Darbari, and N. Talebi. Long-range self-hybridized exciton-polaritons in two-dimensional ruddlesden-popper perovskites. *ACS Photonics*, 2024.

[18] S. Shen, P. Xie, Q. Ding, L. Yue, J. Du, H. Zhang, and W. Wang. Manipulation of intrinsic light-matter interaction in a single self-hybridizing ws_2 nanodisk. *Physical Review B*, 110(15), 2024.

[19] P. Xie, W. Wang, and Y. Cheng. Plasmon-assisted boosting of strong self-hybrid exciton-anapole coupling in bulk transition metal dichalcogenides nanoresonators. *Applied Physics Letters*, 124(20), 2024.

[20] W. Yang, J. Wang, Y. He, S. Jiang, L. Hou, and L. Zhuo. Anapole assisted self-hybridized exciton-polaritons in perovskite metasurfaces. *Nanoscale*, 16(12):6068–6077, 2024.

[21] H. Zhou, M. Qin, H. Xu, G. Wei, H. Li, W. Gao, J. Liu, and F. Wu. Photonic spin-controlled self-hybridized exciton-polaritons in ws_2 metasurfaces driven by chiral quasi-bound states in the continuum. *Physical Review B*, 109(12), 2024.

[22] P. Grahn, A. Shevchenko, and M. Kaivola. Electric dipole-free interaction of visible light with pairs of subwavelength-size silver particles. *Physical Review B*, 86(3), July 2012.

[23] A. I. Kuznetsov, A. E. Miroshnichenko, Y. H. Fu, J. Zhang, and B. Lukyanchukl. Magnetic light. *Scientific Reports*, 2, 2012.

[24] O. Solgaard. Electromagnetic fields and energy. In *Photonic Microsystems*, MEMS Reference Shelf. Springer, Boston, MA, 2009.

[25] O. Solgaard. Plane waves at interfaces. In *Photonic Microsystems*, MEMS Reference Shelf. Springer, Boston, MA, 2009.

[26] P. Di Sia. Overview of drude-lorentz type models and their applications. *Nanoscale Systems: Mathematical Modeling, Theory and Applications*, 3(1), 2014.

[27] H. S. Sehmi, W. Langbein, and E. A. Muljarov. Optimizing the drude-lorentz model for material permittivity: Method, program, and examples for gold, silver, and copper. *Physical Review B*, 95(11), 2017.

[28] P. Shekhar, J. Atkinson, and Z. Jacob. Hyperbolic metamaterials: fundamentals and applications. *Nano Convergence*, 1(1), 2014.

[29] Z. Guo, H. Jiang, and H. Chen. Hyperbolic metamaterials: From dispersion manipulation to applications. *Journal of Applied Physics*, 127(7), 2020.

[30] W. Cai and V. Shalaev. *Optical metamaterials: Fundamentals and applications*. Springer New York, 2010.

[31] C. L. Cortes, W. Newman, S. Molesky, and Z. Jacob. Quantum nanophotonics using hyperbolic metamaterials. *Journal of Optics (United Kingdom)*, 14(6), 2012.

[32] L. Ferrari, C. Wu, D. Lepage, X. Zhang, and Z. Liu. Hyperbolic metamaterials and their applications. *Progress in Quantum Electronics*, 40:1–40, 2015.

[33] A. A. Govyadinov and V. A. Podolskiy. Metamaterial photonic funnels for subdiffraction light compression and propagation. *Physical Review B*, 73(15), 2006.

[34] P. Guo, R. P. H. Chang, and R. D. Schaller. Tunable infrared hyperbolic metamaterials with periodic indium-tin-oxide nanorods. *Applied Physics Letters*, 111(2), 2017.

[35] Y. Guo, W. Newman, C. L. Cortes, and Z. Jacob. Applications of hyperbolic metamaterial substrates. *Advances in OptoElectronics*, 2012, 2012.

[36] H. Herzig Sheinfux, I. Kaminer, Y. Plotnik, G. Bartal, and M. Segev. Subwavelength multilayer dielectrics: Ultrasensitive transmission and breakdown of effective-medium theory. *Physical Review Letters*, 113(24), 2014.

[37] A. J. Hoffman, L. Alekseyev, S. S. Howard, K. J. Franz, D. Wasserman, V. A. Podolskiy, E. E. Narimanov, D. L. Sivco, and C. Gmachl. Negative refraction in semiconductor metamaterials. *Nature Materials*, 6(12):946–950, 2007.

[38] Z. Jacob, J. Y. Kim, G. V. Naik, A. Boltasseva, E. E. Narimanov, and V. M. Shalaev. Engineering photonic density of states using metamaterials. *Applied Physics B*, 100(1):215–218, 2010.

[39] K. Korzeb, M. Gajc, and D. A. Pawlak. Compendium of natural hyperbolic materials. *Optics Express*, 23(20):25406–25424, 2015.

[40] E. E. Narimanov and A. V. Kildishev. Metamaterials: Naturally hyperbolic. *Nature Photonics*, 9(4):214–216, 2015.

[41] S. V. Zhukovsky, A. Andryieuski, O. Takayama, E. Shkondin, R. Malureanu, F. Jensen, and A. V. Lavrinenko. Experimental demonstration of effective medium approximation breakdown in deeply subwavelength all-dielectric multilayers. *Physical Review Letters*, 115(17), 2015.

[42] A. Poddubny, I. Iorsh, P. Belov, and Y. Kivshar. Hyperbolic metamaterials. *Nature Photonics*, 7(12):958–967, 2013.

[43] M. E. Nasir, S. Peruch, N. Vasilantonakis, W. P. Wardley, W. Dickson, G. A. Wurtz, and A. V. Zayats. Tuning the effective plasma frequency of nanorod metamaterials from visible to telecom wavelengths. *Applied Physics Letters*, 107(12), 2015.

[44] M. A. Noginov, Y. A. Barnakov, G. Zhu, T. Tumkur, H. Li, and E. E. Narimanov. Bulk photonic metamaterial with hyperbolic dispersion. *Applied Physics Letters*, 94(15), 2009.

[45] J. B. Pendry, D. Schurig, and D. R. Smith. Controlling electromagnetic fields. *Science*, 312(5781):1780–1782, 2006.

[46] N. Vasilantonakis, M. E. Nasir, W. Dickson, G. A. Wurtz, and A. V. Zayats. Bulk plasmon-polaritons in hyperbolic nanorod metamaterial waveguides. *Laser and Photonics Reviews*, 9(3):345–353, 2015.

[47] J. A. Schuller, E. S. Barnard, W. Cai, Y. C. Jun, J. S. White, and M. L. Brongersma. Plasmonics for extreme light concentration and manipulation. *Nature Materials*, 9(3), 2010.

[48] C. F. Bohren and D. R. Huffman. *Absorption and scattering of light by small particles*. Wiley, 1983.

[49] S. A. Maier. *Plasmonics: Fundamentals and applications*. Plasmonics: Fundamentals and Applications. Springer, 2007.

[50] N. W. Ashcroft and N. D. Mermin. *Solid State Physics*. Cengage Learning, 1976.

[51] M. P. Mcoyi, K. T. Mpofu, M. Sekhwama, and P. Mthunzi-Kufa. Developments in localized surface plasmon resonance. *Plasmonics*, 20(7):5481–5520, 2025.

[52] W. L. Barnes, A. Dereux, and T. W. Ebbesen. Surface plasmon subwavelength optics. *Nature*, 424(6950), 2003.

[53] K. A. Willets and R. P. van Duyne. Localized surface plasmon resonance spectroscopy and sensing. *Annual Review of Physical Chemistry*, 58:267–297, 2007.

[54] A. I. Kuznetsov, A. E. Miroshnichenko, M. L. Brongersma, Y. S. Kivshar, and B. Luk'yanchuk. Optically resonant dielectric nanostructures. *Science*, 354(6314), 2016.

[55] D. G. Baranov, D. A. Zuev, S. I. Lepeshov, O. v. Kotov, A. E. Krasnok, A. B. Evlyukhin, and B. N. Chichkov. All-dielectric nanophotonics: the quest for better materials and fabrication techniques. *Optica*, 4(7):814, 2017.

[56] S. B. Anantharaman, K. Jo, and D. Jariwala. Exciton-photonics: From fundamental science to applications. *ACS Nano*, 15(8):12628–12654, 2021.

[57] R. Bose, J. Gao, J. F. McMillan, A. D. Williams, and C. W. Wong. Cryogenic spectroscopy of ultra-low density colloidal lead chalcogenide quantum dots on chip-scale optical cavities towards single quantum dot near-infrared cavity qed. *Optics Express*, 17(25), 2009.

[58] J. Kasprzak, M. Richard, S. Kundermann, A. Baas, P. Jeambrun, J. M. J. Keeling, F. M. Marchetti, M. H. Szymánska, R. André, J. L. Staehli, V. Savona, P. B. Littlewood, B. Deveaud, and L. S. Dang. Bose-einstein condensation of exciton polaritons. *Nature*, 443(7110), 2006.

[59] S. Ghosh, R. Su, J. Zhao, A. Fieramosca, J. Wu, T. Li, Q. Zhang, F. Li, Z. Chen, T. Liew, D. Sanvitto, and Q. Xiong. Microcavity exciton polaritons at room temperature. *Photonics Insights*, 1(1), 2022.

[60] X. Xiong, N. Kongsuwan, Y. Lai, C. E. Png, L. Wu, and O. Hess. Room-temperature plexcitonic strong coupling: Ultrafast dynamics for quantum applications. *Applied Physics Letters*, 118(13), 2021.

[61] G. Wang, A. Chernikov, M. M. Glazov, T. F. Heinz, X. Marie, T. Amand, and B. Urbaszek. Colloquium: Excitons in atomically thin transition metal dichalcogenides. *Reviews of Modern Physics*, 90(2), 2018.

[62] G. Conibeer, I. Perez-Wurfl, X. Hao, D. Di, and D. Lin. Si solid-state quantum dot-based materials for tandem solar cells. *Nanoscale Research Letters*, 7, 2012.

[63] K. Wojtasik, M. Zięba, M. Wojtasik, C. Tyszkiewicz, M. Pokladko-Kowar, E. Gondek, A. Danel, and P. Karasiński. Chemical doping of a silica matrix with a new organic dye from the group of heterocyclic compounds—chemical, optical and surface characteristics. *Crystals*, 12(4), 2022.

[64] R. Mupparapu, T. Bucher, and I. Staude. Integration of two-dimensional transition metal dichalcogenides with mie-resonant dielectric nanostructures. *Advances in Physics: X*, 5(1), 2020.

[65] F. Shen, Z. Zhang, Y. Zhou, J. Ma, K. Chen, H. Chen, S. Wang, J. Xu, and Z. Chen. Transition metal dichalcogenide metaphotonic and self-coupled polaritonic platform grown by chemical vapor deposition. *Nature Communications*, 13(1), 2022.

[66] T. J. Antosiewicz, S. P. Apell, and T. Shegai. Plasmon-exciton interactions in a core-shell geometry: From enhanced absorption to strong coupling. *ACS Photonics*, 1(5):454–463, 2014.

[67] A. Canales, T. Karmstrand, D. G. Baranov, T. J. Antosiewicz, and T. O. Shegai. Polaritonic linewidth asymmetry in the strong and ultrastrong coupling regime. *Nanophotonics*, 12(21), 2023.

[68] A. Azem. Jaynes-cummings model. *Physics Subject Headings (PhySH)*, 2016.

[69] Z. Liu, J. Li, Z. Liu, W. Li, J. Li, C. Gu, and Z. Y. Li. Fano resonance rabi splitting of surface plasmons. *Scientific Reports*, 7(1), 2017.

[70] M. Blaha, A. Johnson, A. Rauschenbeutel, and J. Volz. Beyond the tavis-cummings model: Revisiting cavity qed with ensembles of quantum emitters. *Physical Review A*, 105(1), 2022.

[71] Q. Zhang, C. Zhang, M. Zhao, Y. Li, and J. Dai. Exciton-plasmon coupling modulation between organic-inorganic hybrid bromide lead perovskites and aluminum nanoparticle lattices. *Journal of Luminescence*, 255, 2023.

[72] C. M. Sparrow. On spectroscopic resolving power. *The Astrophysical Journal*, 44:76, September 1916.

[73] Felix Stete, Wouter Koopman, and Matias Bargheer. Signatures of strong coupling on nanoparticles: Revealing absorption anticrossing by tuning the dielectric environment. *ACS Photonics*, 4(7):1669–1676, July 2017.

[74] Gülis Zengin, Tina Gschneidtner, Ruggero Verre, Lei Shao, Tomasz J. Antosiewicz, Kasper Moth-Poulsen, Mikael Käll, and Timur Shegai. Evaluating conditions for strong coupling between nanoparticle plasmons and organic dyes using scattering and absorption spectroscopy. *The Journal of Physical Chemistry C*, 120(37):20588–20596, March 2016.

[75] V. Savona, L.C. Andreani, P. Schwendimann, and A. Quattropani. Quantum well excitons in semiconductor microcavities: Unified treatment of weak and strong coupling regimes. *Solid State Communications*, 93(9):733–739, March 1995.

[76] G. Khitrova, H. M. Gibbs, M. Kira, S. W. Koch, and A. Scherer. Vacuum rabi splitting in semiconductors. *Nature Physics*, 2(2):81–90, February 2006.

[77] D. S. Dovzhenko, S. V. Ryabchuk, Yu. P. Rakovich, and I. R. Nabiev. Light–matter interaction in the strong coupling regime: configurations, conditions, and applications. *Nanoscale*, 10(8):3589–3605, 2018.

[78] J. Lawless, C. Hrelescu, C. Elliott, L. Peters, N. McEvoy, and A. L. Bradley. Influence of gold nano-bipyramid dimensions on strong coupling with excitons of monolayer mos2. *ACS Applied Materials & Interfaces*, 12(41), 2020.

[79] T. Song, Z. Chen, W. Zhang, L. Lin, Y. Bao, L. Wu, and Z. K. Zhou. Compounding plasmon-exciton strong coupling system with gold nanofilm to boost rabi splitting. *Nanomaterials*, 9(4), 2019.

[80] M. S. Kirschner, W. Ding, Y. Li, C. T. Chapman, A. Lei, X. M. Lin, L. X. Chen, G. C. Schatz, and R. D. Schaller. Phonon-driven oscillatory plasmonic excitonic nanomaterials. *Nano Letters*, 18(1), 2018.

[81] J. Cuadra, D. G. Baranov, M. Wersäll, R. Verre, T. J. Antosiewicz, and T. Shegai. Observation of tunable charged exciton polaritons in hybrid monolayer ws2-plasmonic nanoantenna system. *Nano Letters*, 18(3), 2018.

[82] D. Melnikau, A. A. Govyadinov, A. Sánchez-Iglesias, M. Grzelczak, I. R. Nabiev, L. M. Liz-Marzán, and Y. P. Rakovich. Double rabi splitting in a strongly coupled system of core-shell au@ag nanorods and j-aggregates of multiple fluorophores. *Journal of Physical Chemistry Letters*, 10(20), 2019.

[83] R. Liu, Z. K. Zhou, Y. C. Yu, T. Zhang, H. Wang, G. Liu, Y. Wei, H. Chen, and X. H. Wang. Strong light-matter interactions in single open plasmonic nanocavities at the quantum optics limit. *Physical Review Letters*, 118(23), 2017.

[84] K. Das, J. Dey, M. S. Verma, M. Kumar, and M. Chandra. Probing the role of oscillator strength and charge of exciton forming molecular j-aggregates in controlling nanoscale plasmon-exciton interactions. *Physical Chemistry Chemical Physics*, 22(36), 2020.

[85] V. Krivenkov, Y. P. Rakovich, P. Samokhvalov, and I. Nabiev. ph-sensing platform based on light-matter coupling in colloidal complexes of silver nanoplates and j-aggregates. *Journal of Physical Chemistry C*, 125(3), 2021.

[86] F. M. Balci, S. Sarisozen, N. Polat, and S. Balci. Colloidal nanodisk shaped plexcitonic nanoparticles with large rabi splitting energies. *Journal of Physical Chemistry C*, 123(43), 2019.

[87] F. Muckel, K. N. Guye, S. M. Gallagher, Y. Liu, and D. S. Ginger. Tuning hybrid exciton-photon fano resonances in two-dimensional organic-inorganic perovskite thin films. *Nano Letters*, 21(14), 2021.

[88] K. Santhosh, O. Bitton, L. Chuntonov, and G. Haran. Vacuum rabi splitting in a plasmonic cavity at the single quantum emitter limit. *Nature Communications*, 7, 2016.

[89] J. Heintz, N. Markešević, E. Y. Gayet, N. Bonod, and S. Bidault. Few-molecule strong coupling with dimers of plasmonic nanoparticles assembled on dna. *ACS Nano*, 15(9), 2021.

[90] E. M. Roller, C. Argyropoulos, A. Högele, T. Liedl, and M. Pilo-Pais. Plasmon-exciton coupling using dna templates. *Nano Letters*, 16(9), 2016.

[91] Z. He, F. Li, P. Zuo, C. Xu, W. He, J. He, Y. Zhou, Q. Zhang, K. Chen, H. Huang, and L. Hu. Strong coupling in a hybrid system of silver nanoparticles and j-aggregates at room temperature. *Journal of Physical Chemistry C*, 126(40), 2022.

[92] R. Chikkaraddy, V. A. Turek, N. Kongsuwan, F. Benz, C. Carnegie, T. van de Goor, B. de Nijs, A. Demetriadou, O. Hess, U. F. Keyser, and J. J. Baumberg. Mapping nanoscale hotspots with single-molecule emitters assembled into plasmonic nanocavities using dna origami. *Nano Letters*, 18(1), 2018.

[93] Z. Yuan, P. C. Wu, and Y. C. Chen. Optical resonator enhanced photovoltaics and photocatalysis: Fundamental and recent progress. *Laser and Photonics Reviews*, 16(2), 2022.

[94] M. E. Kleemann, R. Chikkaraddy, E. M. Alexeev, D. Kos, C. Carnegie, W. Deacon, A. C. de Pury, C. Große, B. de Nijs, J. Mertens, A. I. Tartakovskii, and J. J. Baumberg. Strong-coupling of wse2 in ultra-compact plasmonic nanocavities at room temperature. *Nature Communications*, 8(1), 2017.

[95] X. Han, K. Wang, X. Xing, M. Wang, and P. Lu. Rabi splitting in a plasmonic nanocavity coupled to a ws2 monolayer at room temperature. *ACS Photonics*, 5(10), 2018.

[96] J. Qin, Y. H. Chen, Z. Zhang, Y. Zhang, R. J. Blaikie, B. Ding, and M. Qiu. Revealing strong plasmon-exciton coupling between nanogap resonators and two-dimensional semiconductors at ambient conditions. *Physical Review Letters*, 124(6), 2020.

[97] S. Hu, J. Huang, R. Arul, A. Sánchez-Iglesias, Y. Xiong, L. M. Liz-Marzán, and J. J. Baumberg. Robust consistent single quantum dot strong coupling in plasmonic nanocavities. *Nature Communications*, 15(1), 2024.

[98] O. S. Ojambati, R. Chikkaraddy, W. D. Deacon, M. Horton, D. Kos, V. A. Turek, U. F. Keyser, and J. J. Baumberg. Quantum electrodynamics at room temperature coupling a single vibrating molecule with a plasmonic nanocavity. *Nature Communications*, 10(1), 2019.

[99] E. S. H. Kang, S. Chen, S. Sardar, D. Tordera, N. Armakavicius, V. Darakchieva, T. Shegai, and M. P. Jonsson. Strong plasmon-exciton coupling with directional absorption features in optically thin hybrid nanohole metasurfaces. *ACS Photonics*, 5(10), 2018.

[100] A. Tsargorodska, M. L. Cartron, C. Vasilev, G. Kodali, O. A. Mass, J. J. Baumberg, P. L. Dutton, C. N. Hunter, P. Törmä, and G. J. Leggett. Strong coupling of localized surface plasmons to excitons in light-harvesting complexes. *Nano Letters*, 16(11):6850–6856, 2016.

[101] K. D. Park, M. A. May, H. Leng, J. Wang, J. A. Kropp, T. Gougousi, M. Pelton, and M. B. Raschke. Tip-enhanced strong coupling spectroscopy, imaging, and control of a single quantum emitter. *Science Advances*, 5(7), 2019.

[102] F. Wu, J. Guo, Y. Huang, K. Liang, L. Jin, J. Li, X. Deng, R. Jiao, Y. Liu, J. Zhang, W. Zhang, and L. Yu. Plexcitonic optical chirality: Strong exciton-plasmon coupling in chiral j-aggregate-metal nanoparticle complexes. *ACS Nano*, 15(2), 2021.

[103] J. Zhu, F. Wu, Z. Han, Y. Shang, F. Liu, H. Yu, L. Yu, N. Li, and B. Ding. Strong light-matter interactions in chiral plasmonic-excitonic systems assembled on dna origami. *Nano Letters*, 21(8), 2021.

[104] C. M. Guvenc, F. M. Balci, S. Sarisozen, N. Polat, and S. Balci. Colloidal bimetallic nanorings for strong plasmon exciton coupling. *Journal of Physical Chemistry C*, 124(15), 2020.

[105] V. A. Markel. Introduction to the maxwell garnett approximation: tutorial. *Journal of the Optical Society of America A*, 33(7):1244–1256, 2016.

[106] O. Takayama and A. V. Lavrinenko. Optics with hyperbolic materials [invited]. *Journal of the Optical Society of America B*, 36(8):F38–F51, 2019.

[107] Allen Taflove and Susan C. Hagness. *Computational Electrodynamics: The Finite-Difference Time-Domain Method*. Artech House, 3rd edition, 2005.

[108] Kane S. Yee. Numerical solution of initial boundary value problems involving Maxwell's equations in isotropic media. *IEEE Transactions on Antennas and Propagation*, 14(3):302–307, 1966.

[109] Dennis M. Sullivan. *Electromagnetic Simulation Using the FDTD Method*. John Wiley & Sons, 2nd edition, 2013.

[110] K. S. Kunz and R. J. Luebbers. *The Finite Difference Time Domain Method for Electromagnetics*. CRC Press, 1993. Reprint edition 2018.

[111] S. D. Gedney. *Introduction to the Finite-Difference Time-Domain (FDTD) method for electromagnetics*, volume 27 of *Synthesis Lectures on Computational Electromagnetics*. Morgan & Claypool Publishers, 2011.

[112] Lukas Novotny and Bert Hecht. *Principles of Nano-Optics*. Cambridge University Press, 2nd edition, 2012.

[113] Mark I. Stockman. Nanoplasmonics: past, present, and glimpse into future. *Optics Express*, 19(22):22029–22106, 2011.

[114] A. F. Oskooi, D. Roundy, M. Ibanescu, P. Bermel, J. D. Joannopoulos, and S. G. Johnson. Meep: A flexible free-software package for electromagnetic simulations by the FDTD method. *Computer Physics Communications*, 181(3):687–702, 2010.

[115] P. Sypek, A. Dziekonski, and M. Mrozowski. How to render FDTD computations more effective using a graphics accelerator. *IEEE Transactions on Magnetics*, 47(3):1324–1327, 2009.

[116] S. Adams, J. Payne, and R. Boppana. Finite difference time domain (FDTD) simulations using graphics processors. In *Department of Defense - Proceedings of the HPCMP Users Group Conference 2007; High Performance Computing Modernization Program: A Bridge to Future Defense, DoD HPCMP UGC*, pages 334–338, 2007.

[117] Jean-Pierre Berenger. A perfectly matched layer for the absorption of electromagnetic waves. *Journal of Computational Physics*, 114(2):185–200, 1994.

[118] John B. Schneider. *Understanding the Finite-Difference Time-Domain Method*. School of Electrical Engineering and Computer Science, Washington State University, 2010. Available online.

[119] Wenhua Yu and Raj Mittra. *Conformal Finite-Difference Time-Domain Maxwell's Equations Solver*. Artech House, 2003.

[120] Lumerical Solutions, Inc. FDTD solutions knowledge base, 2020. Retrieved from https://support.lumerical.com.

[121] I. R. Capoglu, A. Taflove, and V. Backman. A frequency-domain near-field-to-far-field transform for planar layered media. *IEEE Transactions on Antennas and Propagation*, 60(4):1878–1885, 2012.

[122] T. Hinamoto and M. Fujii. Menp: an open-source matlab implementation of multipole expansion for nanophotonics. *OSA Continuum*, 4(5):1640, 2021.

[123] R. Alaee, C. Rockstuhl, and I. Fernandez-Corbaton. An electromagnetic multipole expansion beyond the long-wavelength approximation. *Optics Communications*, 407:17–21, 2018.

[124] P. C. Waterman. Symmetry, unitarity, and geometry in electromagnetic scattering. *Physical Review D*, 3(4):825–839, February 1971.

[125] P W Barber and S C Hill. *Light Scattering by Particles: Computational Methods*. WORLD SCIENTIFIC, July 1990.

[126] A. Doicu, T. Wriedt, and Y. A. Eremin. *Light Scattering by Systems of Particles Null-Field Method with Discrete Sources: Theory and Programs*. Springer, 2006.

[127] A. Doicu and T. Wriedt. Calculation of the t matrix in the null-field method with discrete sources. *Journal of the Optical Society of America A*, 16(10):2539–2544, 1999.

[128] A. Egel, K. M. Czajkowski, D. Theobald, K. Ladutenko, A. S. Kuznetsov, and L. Pattelli. Smuthi: A python package for the simulation of light scattering by multiple particles near or between planar interfaces. *Journal of Quantitative Spectroscopy and Radiative Transfer*, 273, 2021.

[129] R. Alaee, C. Rockstuhl, and I. Fernandez-Corbaton. Exact multipolar decompositions with applications in nanophotonics. *Advanced Optical Materials*, 7(1), 2019.

[130] Lukas Novotny. Strong coupling, energy splitting, and level crossings: A classical perspective. *American Journal of Physics*, 78(11):1199–1202, October 2010.

[131] X. Wu, Y. Sun, and M. Pelton. Quantum-dot-induced transparency in a nanoscale plasmonic resonator. *Optics Express*, 18(23), 2010.

[132] B. Munkhbat, D. G. Baranov, A. Bisht, M. A. Hoque, B. Karpiak, S. P. Dash, and T. Shegai. Electrical control of hybrid monolayer tungsten disulfide-plasmonic nanoantenna light-matter states at cryogenic and room temperatures. *ACS Nano*, 14(1):1196–1206, 2020.

[133] K. M. Czajkowski, M. Bancerek, A. Korneluk, D. Switlik, and T. J. Antosiewicz. Polarization-dependent mode coupling in hyperbolic nanospheres. *Nanophotonics*, 10(10):2737–2751, 2021.

[134] A. E. Arumona, K. M. Czajkowski, and T. J. Antosiewicz. Material- and shape-dependent optical modes of hyperbolic spheroidal nano-resonators. *Optics Express*, 31(14):23459, 2023.

[135] A. V. Kabashin, P. Evans, S. Pastkovsky, W. Hendren, G. A. Wurtz, R. Atkinson, R. Pollard, V. A. Podolskiy, and A. V. Zayats. Plasmonic nanorod metamaterials for biosensing. *Nature Materials*, 8(11):867–871, 2009.

[136] T. Li and J. B. Khurgin. Hyperbolic metamaterials: beyond the effective medium theory. *Optica*, 3(12):1388, 2016.

[137] M. N. Gjerding, R. Petersen, T. G. Pedersen, N. A. Mortensen, and K. S. Thygesen. Layered van der waals crystals with hyperbolic light dispersion. *Nature Communications*, 8(1), 2017.

[138] J. D. Caldwell, A. V. Kretinin, Y. Chen, V. Giannini, M. M. Fogler, Y. Francescato, C. T. Ellis, J. G. Tischler, C. R. Woods, A. J. Giles, M. Hong, K. Watanabe, T. Taniguchi, S. A. Maier, and K. S. Novoselov. Sub-diffractional volume-confined polaritons in the natural hyperbolic material hexagonal boron nitride. *Nature Communications*, 5, 2014.

[139] R. Carmina Monreal, T. J. Antosiewicz, and S. P. Apell. Competition between surface screening and size quantization for surface plasmons in nanoparticles. *New Journal of Physics*, 15, 2013.

[140] N. A. Mortensen. Mesoscopic electrodynamics at metal surfaces - from quantum-corrected hydrodynamics to microscopic surface-response formalism. *Nanophotonics*, 10(10):2563–2616, 2021.

[141] T. Stefaniuk, P. WrÃ³bel, P. Trautman, and T. Szoplik. Ultrasmooth metal nanolayers for plasmonic applications: surface roughness and specific resistivity. *Applied Optics*, 53(10):B237, 2014.

[142] L. Sun, Z. Li, T. S. Luk, X. Yang, and J. Gao. Nonlocal effective medium analysis in symmetric metal-dielectric multilayer metamaterials. *Physical Review B - Condensed Matter and Materials Physics*, 91(19), 2015.

[143] S. G. Castillo-LÃ³pez, A. A. Krokhin, N. M. Makarov, and F. PÃ©rez-RodrÃguez. Electrodynamics of superlattices with ultra-thin metal layers: quantum landau damping and band gaps with nonzero density of states. *Optical Materials Express*, 9(2):673, 2019.

[144] S. Kozik, M. A. Binhussain, A. Smirnov, N. Khilo, and V. Agabekov. Investigation of surface roughness influence on hyperbolic metamaterial performance. *Advanced Electromagnetics*, 3(2), 2014.

[145] Adrian Doicu and Michael I. Mishchenko. An overview of the null-field method. i: Formulation and basic results. *Physics Open*, 5:100020, 2020.

[146] N. Maccaferri, Y. Zhao, T. Isoniemi, M. Iarossi, A. Parracino, G. Strangi, and F. de Angelis. Hyperbolic meta-antennas enable full control of scattering and absorption of light. *Nano Letters*, 19(3):1851–1859, 2019.

[147] A. B. Evlyukhin, T. Fischer, C. Reinhardt, and B. N. Chichkov. Optical theorem and multipole scattering of light by arbitrarily shaped nanoparticles. *Physical Review B*, 94(20), 2016.

[148] S. Gladyshev, K. Frizyuk, and A. Bogdanov. Symmetry analysis and multipole classification of eigenmodes in electromagnetic resonators for engineering their optical properties. *Physical Review B*, 102(7), 2020.

[149] F. M. Schulz, K. Stamnes, and J. J. Stamnes. Point-group symmetries in electromagnetic scattering. *Journal of the Optical Society of America A*, 16(4):853–865, 1999.

[150] T. J. Antosiewicz, S. P. Apell, C. Wadell, and C. Langhammer. Absorption enhancement in lossy transition metal elements of plasmonic nanosandwiches. *Journal of Physical Chemistry C*, 116(38):20522–20529, 2012.

[151] S. Huang, C. Song, G. Zhang, and H. Yan. Graphene plasmonics: Physics and potential applications. *Nanophotonics*, 6(6):1191–1204, 2017.

[152] L. Lin, M. Lou, S. Li, X. Cai, Z. Zhang, and H. Tao. Tuning electronic and optical properties of two-dimensional vertical van der waals arsenene/sns2 heterostructure by strain and electric field. *Applied Surface Science*, 572, 2022.

[153] C. Tserkezis, P. E. Stamatopoulou, C. Wolff, and N. A. Mortensen. Self-hybridisation between interband transitions and mie modes in dielectric nanoparticles. *Nanophotonics*, 13(14):2513–2522, 2024.

[154] A. Canales, D. G. Baranov, T. J. Antosiewicz, and T. Shegai. Abundance of cavity-free polaritonic states in resonant materials and nanostructures. *Journal of Chemical Physics*, 154(2), 2021.

[155] W. Ahn, J. F. Triana, F. Recabal, F. Herrera, and B. S. Simpkins. Modification of ground-state chemical reactivity via lightâ€"matter coherence in infrared cavities. *Science*, 380(6650), 2023.

[156] A. Canales, T. Karmstrand, D. G. Baranov, T. J. Antosiewicz, and T. O. Shegai. Polaritonic linewidth asymmetry in the strong and ultrastrong coupling regime. *Nanophotonics*, 12(21):4073–4086, 2023.

[157] S. Naureen, N. Shahid, A. Dev, and S. Anand. Generation of substrate-free iii-v nanodisks from user-defined multilayer nanopillar arrays for integration on si. *Nanotechnology*, 24:225301, 2013.

[158] B. Munkhbat, P. WrÃ³bel, T. J. Antosiewicz, and T. O. Shegai. Optical constants of several multilayer transition metal dichalcogenides measured by spectroscopic ellipsometry in the 300-1700 nm range: High index, anisotropy, and hyperbolicity. *ACS Photonics*, 9(7):2398–2407, 2022.

[159] G. E. Jellison and F. A. Modine. Parameterization of the optical functions of amorphous materials in the interband region. *Applied Physics Letters*, 69(3):371–374, 1996.

[160] G. E. Jellison and F. A. Modine. Erratum: parameterization of the optical functions of amorphous materials in the interband region. *Applied Physics Letters*, 69(14):2137–2137, 1996.

[161] Amos Egel and Uli Lemmer. Dipole emission in stratified media with multiple spherical scatterers: Enhanced outcoupling from oleds. *Journal of Quantitative Spectroscopy and Radiative Transfer*, 148:165–176, November 2014.